12-2010

A COMPUTATIONAL INVESTIGATION OF CONTACT PRESSURE FOR A NON-PNEMAUTIC WHEEL WITH A META-MATERIAL SHEAR BAND

Renuka Jagadish
Clemson University, rjagadi@g.clemson.edu

A COMPUTATIONAL INVESTIGATION OF CONTACT PRESSURE FOR A NON-PNEMAUTIC WHEEL WITH A META-MATERIAL SHEAR BAND

A Thesis
Presented to
the Graduate School of
Clemson University

In Partial Fulfillment
of the Requirements for the Degree
Master of Science
Mechanical Engineering

By
Renuka Jagadish
December 2010

Accepted by:
Dr. Paul Joseph, Committee Chair
Dr. Joshua D. Summers
Dr. Vincent Blouin

ABSTRACT

One of the missions of National Aeronautics Space Administration (NASA) is to develop a vehicle that can travel for a longer distance on the moon and have a greater degree of mobility compared to the currently used Lunar Roving Vehicles (LRV). This led to the development of the All-Terrain Hex-Limed Extra-Terrestrial Explorer (ATHLETE), which requires a significant advance in the type of wheels that must be used on this highly mobile lander. The Michelin Lunar Wheel, which is a non-pneumatic tire invented by Michelin Researche et Technologie has been identified as one of the key designs capable of performing on the lunar environment and satisfying the mobility requirements of the ATHLETE.

One of the critical characteristics of a tire for mobility in sand is to have a low and constant contact pressure throughout the contact patch. Experimental results obtained by the Swiss MICHELIN team for the Michelin Lunar Wheel indicate that the pressure is not uniform and that the pressure is higher than NASA would prefer. Such pressure non-uniformity is inherent to the design of the tire. Since these wheels are very expensive to build, it is desirable to have the modeling capability to predict pressure accurately and to optimize the pressure distribution.

In this thesis, to understand the contact pressure behavior more clearly, the Michelin Lunar Wheel is initially simplified to only a ring that is pressed between two frictionless rigid planes. The analysis is performed using ABAQUS Standard finite element software. It is seen that all the structural elements in the ABAQUS element

library face difficulty in predicting accurate contact pressure at the edge of contact for a thin and stiff structural member, such as what is used to design the lunar wheel. Convergence with respect to mesh refinement cannot be achieved. To overcome this problem, a soft tread of reasonable stiffness is added on the outer perimeter of the ring which resolves the convergence problem and unique contact pressure profiles are obtained. The modeling approach developed for the simple ring model was extended to both two-dimensional and three-dimensional wheel models.

Sensitivity analysis was performed on the two dimensional model to determine what design parameters affect the contact pressure. These results show that it is very difficult to define the correct computational model to predict accurately the contact pressure since very small displacements can drastically change the pressure distribution. For example, for the baseline loading the wheel deforms about 14 mm leading to a non-uniform pressure. A non-uniform change in displacement with amplitude less than 0.2 mm can convert this non-uniform pressure into a uniform pressure. In order to predict displacement accurately, it is necessary to precisely model the actual geometry and structural connections between small parts, which are very complex to define. Based on this sensitivity analysis and the approach of introducing a non-uniform displacement by modifying the tread thickness, areas for future work are identified and presented at the end of the thesis.

DEDICATION

To my wonderful parents Rekha Jagadish and Jagadish S. Hiregoudar, my sisters Krithika and Archana and my fiancé Srinivasan Krishnamachari for their love and support.

ACKNOWLEDGMENTS

I would like express my deepest gratitude to Dr. Paul Joseph, my committee chair, who supported me throughout my thesis with his patience and knowledge. I attribute my Masters degree to his encouragement and effort without which this thesis would not be possible. I would like to thank my advisory committee Dr. Joshua Summers and Dr. Vincent Blouin for their valuable suggestions during the NASA meetings which kept me heading in the right direction in my thesis.

I would like to genuinely thank my very good friend and mentor Balajee Ananthasayanam for his constant support and guidance and teaching me many useful concepts in ABAQUS when I started working in this project. I would like thank the Marisa Orr for her significant contribution for the numerical modeling and literature of the Michelin Lunar wheel.

Furthermore, I would offer my sincere gratitude to David Palmer, Manoj Chinnakonda and Prashanth Vijalapura for providing valuable insights in my thesis during my tenure as an intern in Dassault Systemes Simulia Corp.

Lastly, I would like to thank my friends Prashanth Palanisamy, Akshay Narasimhan and Dhananjay Joshi who helped during the course of my Masters program at Clemson.

TABLE OF CONTENTS

Page

Page

LIST OF TABLES

Table Page

LIST OF FIGURES

List of Figures (Continued)

List of Figures (Continued)

List of Figures (Continued)

List of Figures (Continued)

List of Figures (Continued)

CHAPTER ONE

INTRODUCTION

1.1 Background

A modern non-pneumatic tire design, named the TWEEL™ [2] which is shown in Figure 1-1, was first proposed and developed by Michelin North Americas Research and Development Corporation.

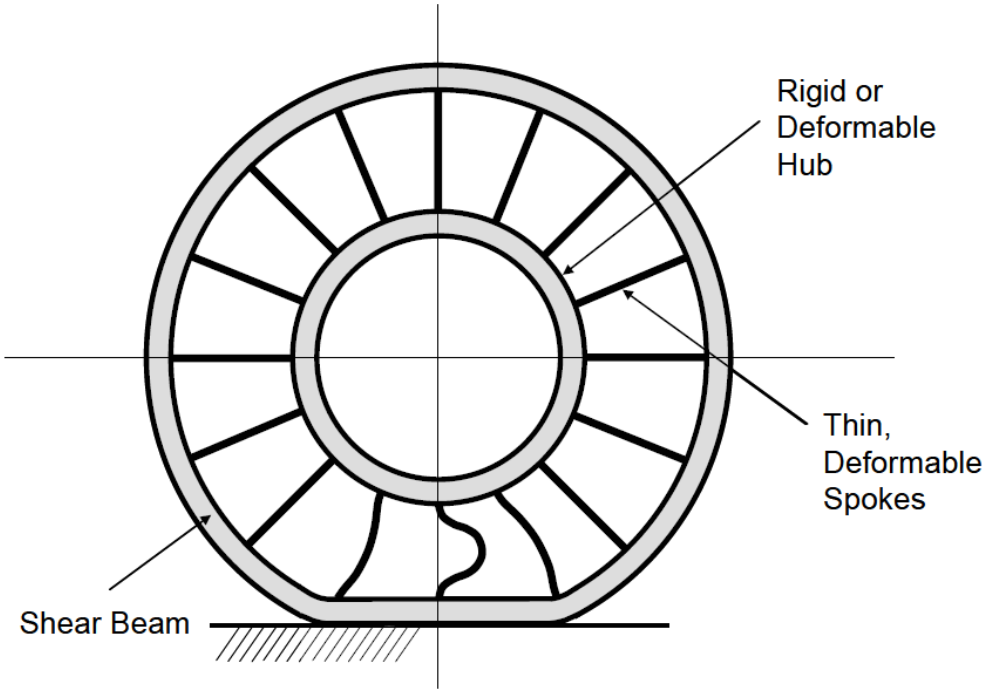

Figure 1-1: Generic Tweel™ and it components described by Rhyne and Cron [2]

This non-pneumatic tire, also referred to as a "structurally supported tire," consists of a hub that is supported by a number of curved spokes extending radially to a reinforced annular band. The annular band, referred to as the "shear band," consists of a material of low elastic modulus (rubber, polyurethane, foamed-rubber or polyurethane) that is sandwiched between inner and outer "inextensible" membranes [1, 2]. The main

objective of the shear layer is to allow "bending-type deformations" of the shear band due primarily to shear deformation. Following Rhyne and Cron [2] the kinematics of deformation within the region of contact, where a circle is deformed into a straight line, requires that the associated shear strain is linear. Such a linear variation in shear strain gives rise to a linear variation of shear force. From mechanics of materials, the associated contact pressure will be uniform. Therefore, for a Tweel™ Tire, the transfer of load from the axle to the ground will have a contact patch with a constant contact pressure, thus performing the function of the inflation pressure in a pneumatic tire.

For exploration on the moon, National Aeronautics and Space Administration (NASA) proposed a new enhanced robotic vehicle called the ATHLETE, which comes from All-Terrain-Hex-Limbed-Terrestrial-Explorer [4, 5]. This latest lunar landing vehicle was developed by NASA's Jet Propulsion Laboratory (JPL) to meet NASA's current mission goal of a "Need for Mobility" and concentrate on eliminating all the disadvantages being faced by the present Lunar Rover vehicle (LRV) [3-6].

The ATHLETE, shown in Figure 1-2, will carry astronaut habitants and move on the lunar soil efficiently [4]. The unique spider like hexagonal ring structure of the ATHLETE has flexibility in all six degrees of freedom in its six legs, allowing it to move, roll, walk or step over obstacles one at a time depending on the terrain conditions (rough or smooth) as shown in Figure 1-3. The other notable feature of the ATHELETE is that it can dock with other units/devices to perform various tasks like manipulation, fueling and cargo handling [4].

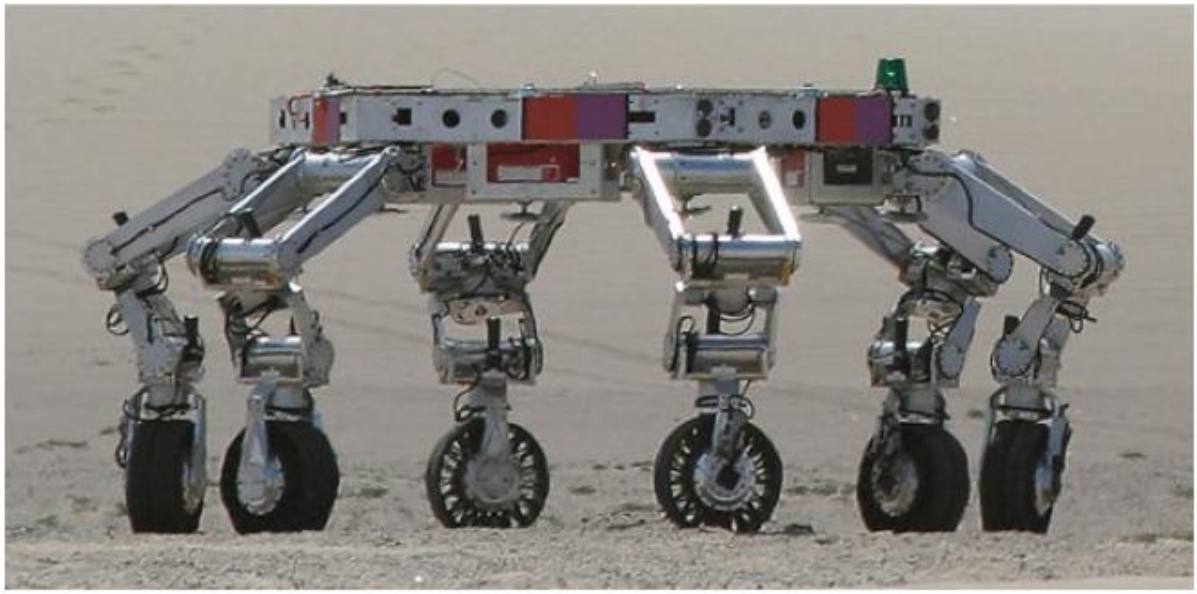

Figure 1-2: The All-Terrain-Hex-Limbed-Terrestrial-Explorer (ATHLETE), photo courtesy NASA/JPL-Caltech [4]

Figure 1-3: ATHLETE during testing, photo courtesy NASA/JPL-Caltech [4]

One of the key requirements for exceptional performance of the ATHLETE lies in the type of wheels to be used on each of the six legs of this mobile lander. The wheels should not only be capable of serving the multiple mobility functions of the ATHLETE,

but also should perform on the treacherous lunar environmental conditions [4, 6]. As the wheels of the ATHLETE roll over the lunar "regolith", which is sand like material on the moon's surface, it has the ability to generate low contact pressure and use energy efficiently. In addition the tire should be made of materials that enable it to maintain traction at very low lunar temperatures, provide shock absorption, be long-lasting and have low rolling resistance. Since pneumatic tires and solid wheels are not good design choices for the several reasons stated in [6], the desire for a new wheel technology was explored.

During the fall 2006 semester, new wheel designs were proposed and studied by senior students at Clemson University for the ATHLETE and three shear band design concepts were developed [6]. One promising shear band design is the segmented cylinder configuration developed by Clemson University and jointly supported by NASA's JPL Robotics development team and Michelin American Research Center (MARC). A generic prototype of the Michelin Lunar Wheel Tire developed by undergraduate students in Clemson University is shown in Figure 1-4.

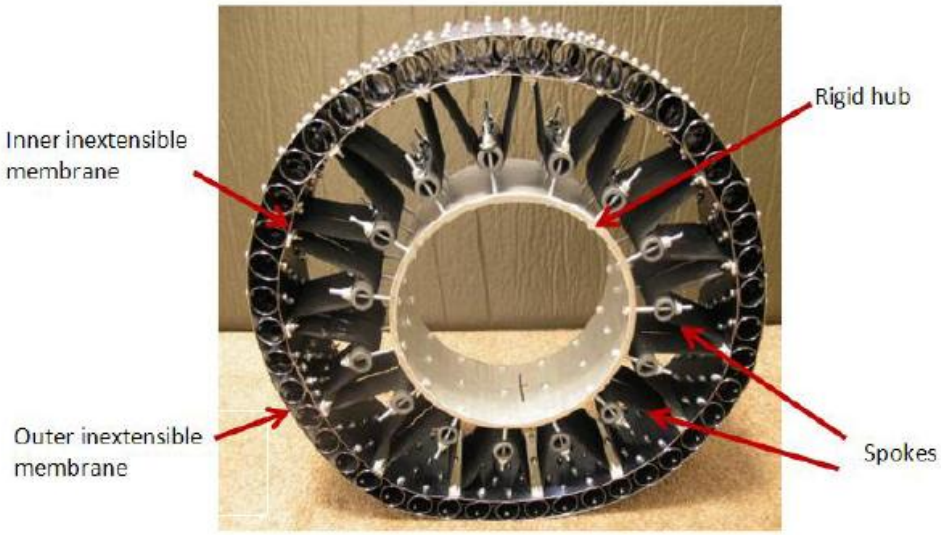

Figure 1-4: Prototype of Michelin Lunar Wheel developed at Clemson University in fall 2006 [6]

Based on the prototype shown in Figure 1-3, the Michelin Lunar Wheel was developed at Michelin Research and Technology. This tire consists of four main components: a tread, a glass fiber composite shear band, thin deformable spokes made of sailcloth, and an aluminum hub. As shown in Figure 2-1, the shear band for lunar application, which is the critical component in a Michelin Lunar Wheel, consists of cylinders enclosed between inner and outer "inextensible" membranes. These components are made of a glass fiber composite that is capable of operating for a wide range of temperature.

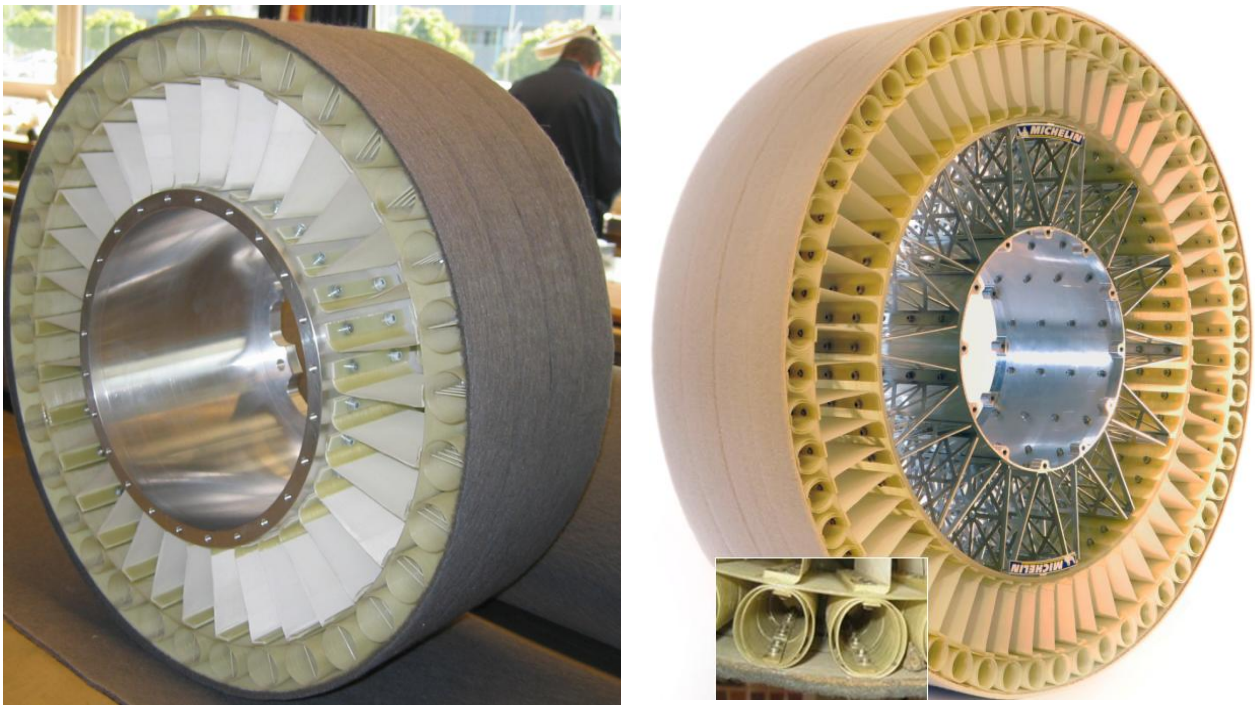

Figure 1-5: First Generation and Third Generation Michelin Lunar Wheel

As shown in Figure 1-1, the first generation Michelin Lunar Wheel shear band has thirty-three circular cylinders with glass fiber rods glued between the inner and outer inextensible membrane with epoxy. The shear band is connected to the hub by a number of thin spokes running radially along the circumference of the inner inextensible membrane and the hub. The diameter of the first generation Michelin Lunar Wheel is 18.5'' (470 mm). The third generation Michelin Lunar Wheel has almost the same configuration as the first generation except that it has a bigger diameter of 27.56'' (702.45mm) and has two sets of fifty-six oval shaped cylinders arranged concentrically which are fixed between the two inextensible membranes by nuts and bolts. .

Specifically, the circular cylinders can be designed to achieve a target low contact pressure of 10 psi [6], which is required for mobility and traction in the lunar regolith.

Compared to the Apollo Lunar Rover Vehicle (LRV) wheel, which supported a load of 254 N per wheel for 120 kilometers [7], the Michelin Lunar Wheel Tire is of low weight and capable of high load carrying capacity satisfying the ATHLETE design to support a load of 2500 N per wheel and travel up to 10,000 kilometers [6].

1.2 Motivation for Current Research

1.2.1 Experimental Results

The pressure distribution for the third generation Swiss Tweel Tire was measured using the TEKSCAN mapping sensors by Michelin Swiss Research Cooperation. The Michelin Lunar Wheel without a tread was pressed on a flat surface by applying a force of 2795.85 N (285 kg) and the TEKSCAN mapping senor was placed between the wheel and the surface. All the four lobes of the Michelin Lunar Wheel were placed on the sensor, which is large enough to include the entire contact patch. This loading engages five of the circular cylinders as shown in the TEKSCAN image in Figure 1-6 and in the experimental picture in Figure 1-7. As shown in the figure, the pressure varies from about 0.3 to 1.7 bar, with an average of 0.81 bar (1 bar = 14.5 psi). It is observed that the end cylinders carry more load than those at the center.

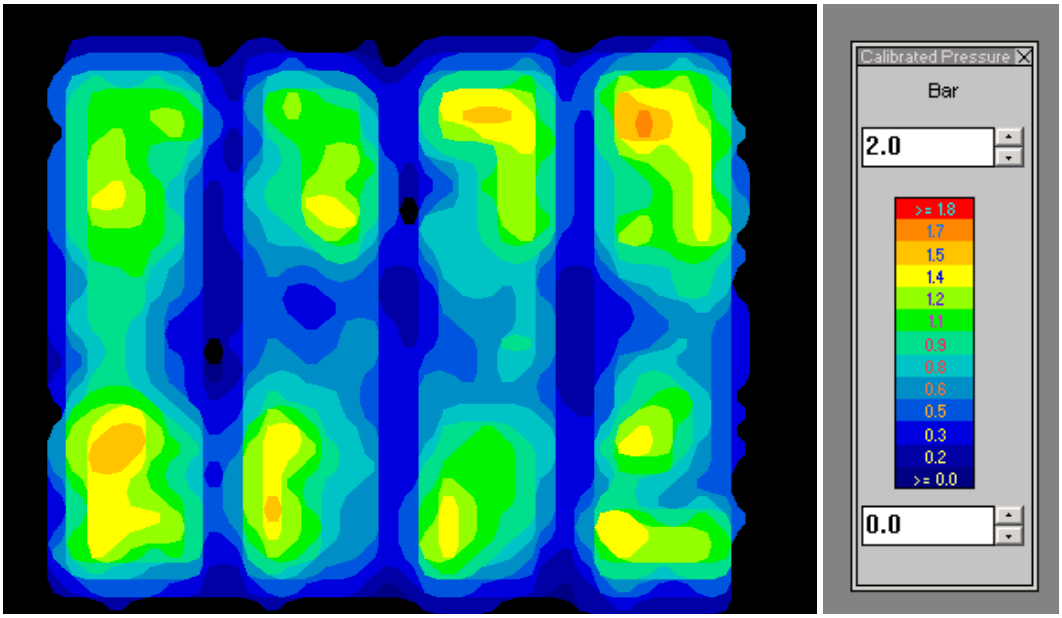

Figure 1-6: Contact Pressure image obtained from TEKSCAN by the Swiss MICHELIN

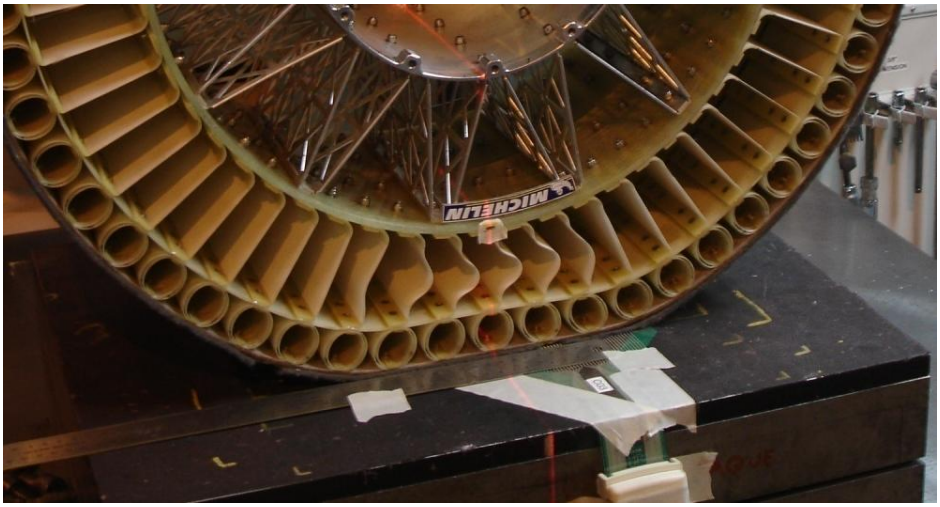

Figure 1-7: Experimental setup showing five of the circular cylinders in contact after loading for the Third Generation Michelin Lunar Wheel

1.2.2 Preliminary simulation results from ABAQUS STANDARD

A 2D finite element model of the First Generation Michelin Lunar Wheel was made. A static analysis was done by applying a load of 625 N (1/4th the load carried by

each wheel) at the center of the analytical rigid ground and pushed up to load the wheel. The deformed model of the wheel in ABAQUS is presented in Figure 1-8 and the contact pressure plot is presented in Figure 1-9.

These early results showed high pressure gradient "*spikes*" formed on the outer inextensible membrane of the Michelin Lunar Wheel, with the highest pressure levels occurring on the outermost cylinders [8]. These results, which were later determined to be incorrect from a computational point of view, also do not agree in form with the experimental results in Figure 1-6 above. On closer examination of the simulation results, it is seen in Figure 1-10 that gaps of very small magnitude exist between the spikes in the contact patch where the contact pressure is zero.

The goal is to develop a computational model of the Michelin Lunar Wheel using ABAQUS Standard which can predict the pressure accurately so that improvements and modifications can be made using simulation.

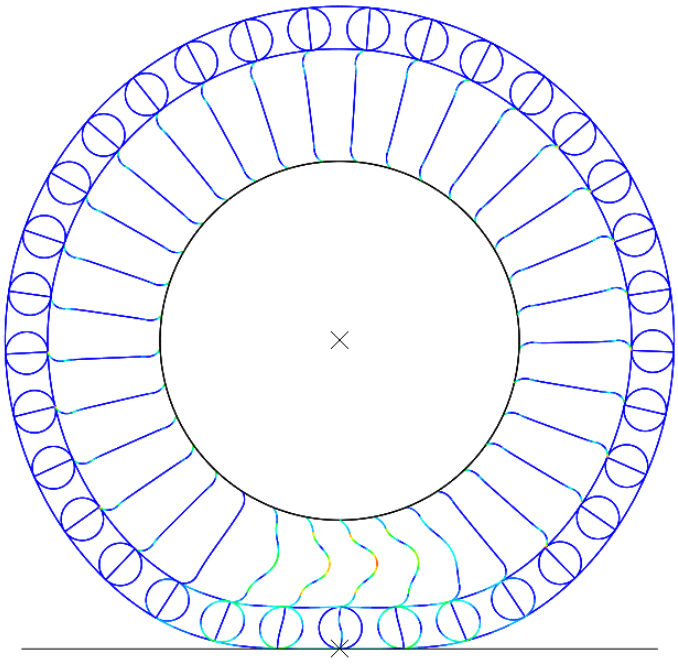

Figure 1-8: Deformed configuration of the First Generation Michelin Lunar Wheel

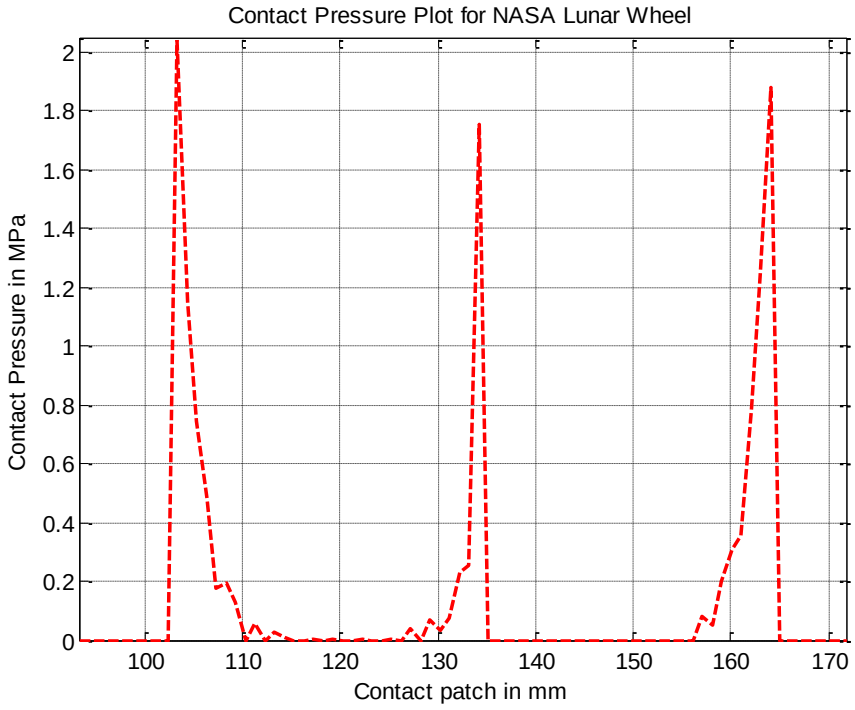

Figure 1-9: Incorrect Contact Pressure for the First Generation Michelin Lunar Wheel from computational point of view

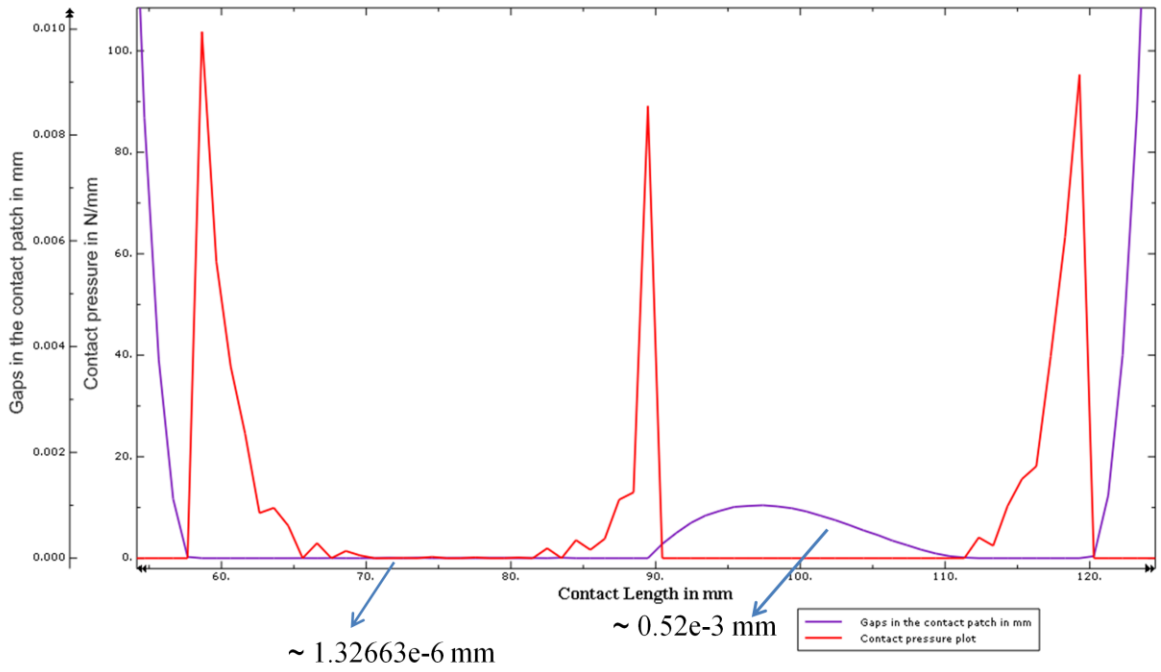

Figure 1-10: Plot showing gaps between the spikes in the contact patch for the First Generation Michelin Lunar Wheel

1.3 Literature Review

The critical characteristics and potential advantages of a TWEEL™ tire over a pneumatic tire are identified by Rhyne and Cron in [2]:

1. Low contact pressure
2. Low stiffness
3. Low mass (load carrying efficiency)
4. Low energy loss from obstacle impacts

In this thesis, the contact pressure associated with the Michelin Lunar Wheel is investigated with the goal of obtaining an optimized pressure and to explain why the

model does not predict the experimental results. The contact pressure, being one of the important characteristic of the TWEEL™, is supposed to have a low and uniform contact profile [2]. As explained by Rhyne and Cron in [2], this is accomplished by shear deformation, which for the case of the Michelin Lunar Wheel, is provided by the shear capability of the cylinders. The size of the contact patch, and therefore the level of pressure, can be changed by changing the shear stiffness of the cylinders. In addition the contact pressure, p_c, for an ideal TWEEL™ Tire is predicted to be dependent on only material properties of the shear band and the geometry of the tire according to

$$p_c \cong \frac{Gh}{R} \tag{1-1}$$

where, G is the shear modulus of the beam, h is height of the beam and R is the radius of the beam. Since this pressure is constant, it is also equal to the total load divided by the contact area.

The TWEEL™ Tire being a so-called 'top loader', transfers the load from the hub to the spokes above the hub, while the spokes below the hub buckle in compression and do not provide any support [2]. As shown in Figure 1-11 when the shear beam deforms, the spoke stiffness governs the stiffness of the TWEEL™ by controlling the ring diameter growth to accommodate or restrain the excess length in the contact patch [2].

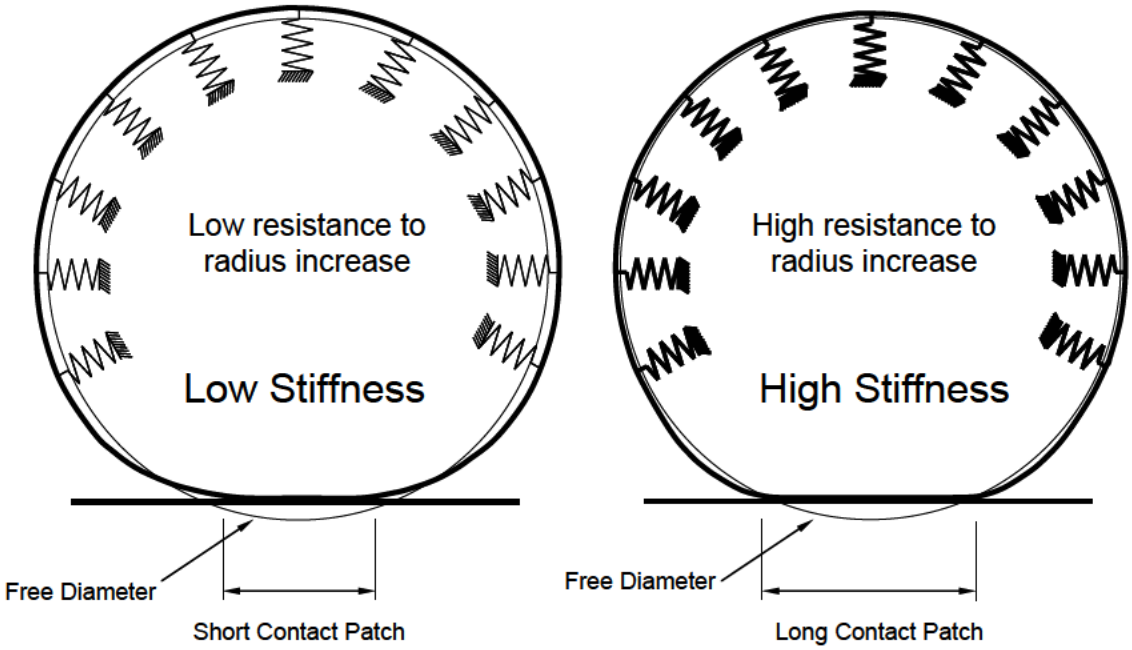

Figure 1-11: Stiffness of the wheel governed by the spokes for constant displacement explained by Rhyne and Cron [2]

For reasons stated in [6], to withstand the cryogenic temperatures on the moon, the discrete shear band design was selected, since the performance of the composite material is not affected at low temperatures and therefore it is capable of imitating the performance characteristics of a conventional TWEEL™. The inextensible membranes of the Michelin Lunar Wheel are thin cylindrical shell structures unlike the conventional TWEEL™ which makes use of steel cord embedded in tire rubber.

Extensive theories have been developed to study the class of contact problems in the theory of beams, plates and shells. Clark [9] in his book 'Mechanics of Pneumatics of Tires' has a chapter which reviews and discuses the importance of various beam theories with respect to contact between the tire and road.

Keer and Silva [10] studied the bending of a beam gradually brought into contact with a cylindrical supporting surface and compared the beam theory results with theory of elasticity solution. In this paper, the contact pressure was studied by varying the following parameters:

- The ratio of the length of the contact region to the thickness of the beam
- The ratio of the length to the thickness of the beam

The numerical results show that the more slender the beam becomes, the more difficult it was to predict the contact pressure accurately. As will be shown in Chapter 2, at the edge of contact the beam theory result become unbounded, while the elasticity result has a finite value that drops to zero at the edge of contact for any given ratio of contact length to the thickness of the beam. In this paper an elasticity solution is provided and the contact stresses are compared with those of beam theory. As the ratio of length to the thickness of the beam is reduced, for beam theory the contact pressure develops into two point loads at the edge of contact. The elasticity solution gives the same result as beam theory in the limit as the beam thickness become very thin. As the beam is made thicker, the contact pressure shows more of a Hertz distribution.

In a later paper, Keer and Miller [11] solved the elasticity problem of contact problem of a finite elastic layer being indented by a cylindrical punch. In this paper they also developed a solution for beam theory to obtain the overall load displacement relationship. In their solutions the ratio of contact length (c) to thickness (h) was varied and the contact pressure distribution was determined. At lower ratios of c/h, a Hertz-like

pressure distribution was seen and at higher ratios of c/h the elasticity solution results in zero shear and normal stress in the contact region which gives rise to spikes at the edge of contact.

In a recent paper by Keer and Block [12] partial contact of a frictionless, elastic curved beam pressed against a flat rigid plane was solved using the method of Michell-Fourier series expansion. The problem is assumed to be geometrically linear. When the curved beam was thick, the stress distribution developed by the plane strain solution resembled Hertz theory for up to 90% - 95% of the beam thickness. When the thickness to length ratio of the beam was made smaller (5% thickness) the contact stress distribution approached elementary beam solution and the results characteristics are the same as those mentioned in the earlier studies, [10] and [11].

Essenburg [13] emphasized the importance of including the effect of the transverse normal strain along with transverse shear deformation in beam theory for contact problems to obtain a more accurate approximation compared to shear deformation theory. Essenburg included the transverse normal component of deformation as a quadratic function in the thickness variable along with transverse shear deformation. He used the example of a beam with pinned ends in contact with a smooth rigid cylindrical surface to demonstrate the importance of transverse normal strain. The higher order beam solution indicates that the pressure is continuous at the boundary of the contact region without any singularities and the contact region develops gaps.

Naghdi and Rubin [14] have considered an example of an isotropic, homogenous elastic beam of rectangular cross section in contact with a smooth rigid surface and

compared three theories, Euler-Bernoulli (E), Timoshenko (T) and a constrained theory which accounts for the normal extensional deformation (N) to a general theory (G) which includes all the type of deformation of the other three theories mentioned above. When the beam is subjected to a bending moment (M) the beam initially establishes contact with the rigid surface. But as the bending moment is increased the general theory predicts the conditions when the beam looses contact. The Euler Bernoulli and the Timoshenko fail to predict these features unlike the normal extensional theory which shows this effect.

Panek [15] in the first part of his thesis solved a contact problem of an infinite wavy layer pressed between two flat surfaces by using the three beam theories: Bernoulli-Euler, Timoshenko and Essenburg beam theory. For comparison, he developed an elasticity solution for the same problem. The results indicated that the Essenburg beam and the elasticity solution had no singularities or discontinuities in the contact pressure.

In another thesis by Robbins [16] the solution of a contact problem for simple symmetric shells pressed against rigid flat surfaces also emphasized that transverse normal stress and strains should be included for better approximation of the contact pressure.

1.4 Organization of this Thesis

In Chapter II, a simplified model is introduced to isolate the difficulty with ABAQUS in predicting accurate converged contact pressure for the Michelin Lunar Wheel. The simple model consists only of a ring that is pressed between two frictionless plates. The complete finite element modeling of the ring along with details of material

properties, contact interactions and contact conditions and other constraints used are described in detail.

In Chapter III, motivated by the work of Essenburg [13], a new modeling approach to overcome the difficulty of convergence with respect to contact pressure is explained by using a tread on the outer inextensible membrane and intense convergence studies are performed and the results are presented.

In Chapter IV the complete two dimensional finite element model of the first generation Michelin Lunar Wheel is explained and the new modeling approach from Chapter III is used to obtain converged contact pressure profiles. Static analysis of the new Wheel model pressed against a rigid plane is performed and results for the converged contact pressure profiles and force-displacement curves are presented. This model was used as a baseline case for sensitivity analysis in Chapter V.

In Chapter V, design sensitivity studies were performed by varying the design variables, which include the details of the connections between the circular cylinders and the membranes, thickness of cylinders, volume fraction of the Glass Composite, and cylinder orientation. This sensitivity analysis reveals the parameters that affect contact pressure. The model which gives the best contact pressure is identified. In addition the slight deviation from a flat surface that would provide a uniform pressure is obtained.

In Chapter VI the finite element model of the three dimensional third generation Michelin Lunar Wheel Tire is presented. Boundary conditions, meshing and the simulation procedure carried out in ABAQUS/Standard are described. The results are

presented and compared with the experimental results and the first generation Michelin Lunar Wheel.

In Chapter VII, which is the last chapter, the research is summarized and several conclusions are made based on the results of the simulations, the experimental results and the theory for contact problems involving thin structures. Recommendations for future work are also made.

CHAPTER TWO

SIMPLIFIED TWO DIMENSIONAL RING PROBLEM

The focus of study in this chapter is the computational predication of contact pressure for this integrated tire and wheel assembly and how the design of the shear band affects this pressure. The contact pressure prediction is complicated by two factors: 1) the structural details of the shear band, and 2) the difficulty of solving a contact problem when shell-like structures are involved. Because of the latter difficulty, and before considering how the design of the shear band affects contact pressure, in this chapter the focus is on the accurate prediction of contact pressure between just the outer inextensible membrane and a rigid flat surface. ABAQUS Standard version 6.8-3 is used for the computational analysis and the problem geometry shown in Figure 2-1 reduces to that of a deformable ring pressed between two parallel frictionless surfaces.

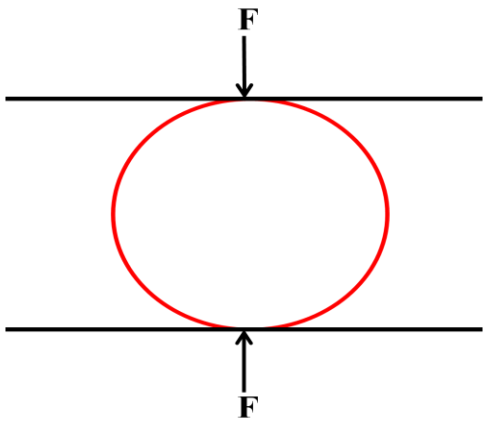

Figure 2-1: Ring pressed between two parallel frictionless plates

As will be shown pressure “spikes” appear at the edges of contact and the associated high pressure gradients make convergence difficult.

In the next section four solutions are presented: an analytical solution that shows the source of the pressure spikes, a beam solution within ABAQUS, a shell theory ABAQUS solution and an FE orthotropic elasticity solution. The shell theory was used in an attempt to include the effect of the transverse normal strain (thickness change) along with transverse shear deformation. See Essenburg [13] and Naghdi and Rubin [14] for the importance of transverse normal strain in predicting pressure.

2.1 Limiting Case of a Straight Euler-Bernoulli Beam: Analytical Solution

The problem of a circular ring pressed flat by a rigid surface (Figure 2-2) can be approximated by making a straight beam conform to the shape of a rigid circle as shown in Figure 2-2.

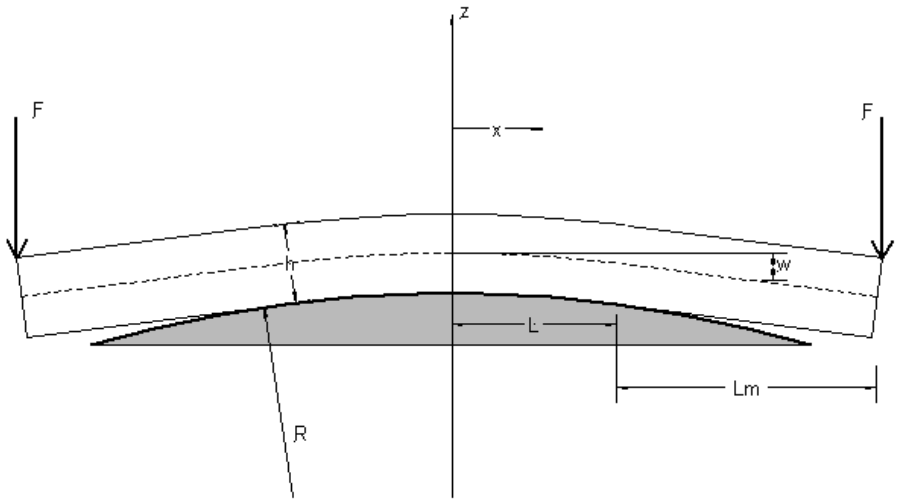

Figure 2-2: Beam on curve image by Steve Cron [2]

For Euler Bernoulli beam theory, which approximates the shear modulus of the beam as infinite, all deformations are due to bending. The moment curvature relationship from mechanics of materials,

$$\frac{1}{R} = \frac{M}{EI}, \tag{2-1}$$

where *1/R* is the radius of curvature, *M* is the bending moment , *E* is the Young's Modulus and *I* is the moment of inertia.

which is valid for relatively large deformations, shows that the internal bending moment in the portion of the beam in contact with the circle is constant. If this is true, then from the relationship between bending moment and shear force *(V)*,

$$\frac{dM}{dx} = V, \tag{2-2}$$

the internal shear force in the beam must be zero. Finally, if this is true, from

$$\frac{dV}{dx} = -p(x), \tag{2-3}$$

it is concluded that pressure, *p(x)*, in the region of contact must be zero. In order to satisfy force equilibrium, the only possibility is for concentrated forces, i.e., *infinite* pressure spikes, to exist at the edge of contact. These concentrated forces can only be relaxed into a finite pressure distribution by allowing the beam to deform in shear and/or radial compression (Essenburg [13], Naghdi and Rubin [14]) or for the deformed shape to be different from a circle. In reality, the outer inextensible membrane has a finite value of shear modulus which removes the concentrated forces. However, the shear modulus is large as shown in Table 2-1 and the feature of pressure spikes is not eliminated.

The above simple analysis shows how convergence of the pressure profile will be very difficult in cases where bending deformation of the beam dominates shear

deformation. For the limiting case where shear deformation dominates bending, i.e., such as the ideal shear band introduced by Rhyne and Cron [2], the pressure for the deformation in Figure 2-2 becomes essentially constant. Referring to Figure 2-1, the outer inextensible member alone is not a shear band and behaves more like an Euler-Bernoulli beam with a non-negligible bending stiffness, so the difficulty with pressure spikes is expected for the full TWEEL^{TM} tire.

2.2 ABAQUS Solution for Beam and Orthotropic Elasticity

2.2.1 Model Geometry

In the finite element study of the ring problem in Figure 2-2, two dimensional beam elements (B21), two dimensional plane stress/plane strain (CPS4R/CPE4R) elements and three dimensional structural shell elements (S4R) are used to model the ring. The three-dimensional shell formulation is made two dimensional by specifying Poisson's ratio as zero in the axial direction. The purpose of exploring all the structural elements available in the ABAQUS Standard library was to test the convergence of the pressure profile by trying to implement the various constraint theories (Euler Bernoulli, Timoshenko and an element type similar to the plate theory used by Essenburg [12]). The dimensions of the ring are: Diameter, D_r = 240 mm, ring thickness, t_r = 1.5mm, ring length, L_r = 95mm. The thickness parameter which is the ratio the radius of the ring to the radius of the ring with the thickness R_r/R_t (120/121.5) = 0.98765. See Keer and Block [11] for the importance of the beam thickness for predicting the contact pressure. The smooth flat ground is modeled as an analytically rigid surface with a straight line

segment. Since contact is involved, using an analytical rigid surface instead of an element based surface has the following advantages [17]:

- Analytically rigid surfaces are not meshed unlike the conventional element based surface, resulting in decreased computational cost in the contact algorithm.
- Analytical rigid surfaces have the ability to parameterize exactly with a curved geometric surface using curved line segments, which results is a smoother surface description, the possibility of reduced contact noise and provides a better approximation to the physical contact constraint.

The disadvantages are [17]:

- An analytical rigid surface must be used as a master surface in contact interactions. Hence it cannot be modeled for a problem which requires two analytical rigid surfaces in contact with each other.
- Contact forces and pressures cannot be contoured on an analytical rigid surface but can be plotted on the slave surface.

2.2.2 Material Properties of the Ring

The entire shear band of the Michelin Lunar Wheel, which includes the ring which is the outer inextensible membrane, is made of glass composite fiber and is orthotropic. The elastic stress strain relations or the stiffness matrix for the orthotropic material is represented by engineering constants and is of the form:

$$\begin{bmatrix}\sigma_{11}\\ \sigma_{22}\\ \sigma_{33}\\ \sigma_{12}\\ \sigma_{13}\\ \sigma_{23}\end{bmatrix}=\begin{bmatrix} D_{1111} & D_{1122} & D_{1133} & 0 & 0 & 0\\ & D_{2222} & D_{2233} & 0 & 0 & 0\\ & & D_{3333} & 0 & 0 & 0\\ & & & D_{1212} & 0 & 0\\ & \text{sym} & & & D_{1313} & 0\\ & & & & & D_{2323}\end{bmatrix}\begin{bmatrix}\varepsilon_{11}\\ \varepsilon_{22}\\ \varepsilon_{33}\\ 2\varepsilon_{12}\\ 2\varepsilon_{13}\\ 2\varepsilon_{23}\end{bmatrix}$$

The engineering constants of the D matrix are given by:

$$D_{1111}=E_1(1-\nu_{23}\nu_{32})\gamma$$

$$D_{2222}=E_2(1-\nu_{13}\nu_{31})\gamma$$

$$D_{3333}=E_3(1-\nu_{12}\nu_{21})\gamma$$

$$D_{1122}=E_1(\nu_{21}+\nu_{31}\nu_{23})\gamma=E_2(\nu_{12}+\nu_{32}\nu_{13})\gamma$$

$$D_{1133}=E_1(\nu_{31}+\nu_{21}\nu_{32})\gamma=E_3(\nu_{13}+\nu_{12}\nu_{23})\gamma$$

$$D_{2233}=E_2(\nu_{32}+\nu_{12}\nu_{31})\gamma=E_3(\nu_{23}+\nu_{21}\nu_{13})\gamma$$

$$D_{1212}=G_{12}$$

$$D_{1313}=G_{13}$$

$$D_{2323}=G_{23}$$

$$\gamma=\frac{1}{1-\nu_{12}\nu_{21}-\nu_{23}\nu_{32}-\nu_{31}\nu_{13}-2\nu_{21}\nu_{32}\nu_{13}}$$

Where, “1” corresponds to the radial direction, “2” corresponds to the circumferential direction and “3” corresponds to the out of plane direction. The values of the constants were provided by MICHELIN and are listed in Table 2-1

Table 2-1: Orthotropic Material Properties of the glass Fiber composite used to make the shear band, which includes the inner and outer inextensible members and the circular cylinders

Young Moduli (MPa)	Shear Moduli (MPa)	Poisson`s ratio
E_1= 39969	G_{12}= 2537	ν_{12} = 0.29
E_2= 6813	G_{23}= 2537	ν_{23} = 0.05
E_3= 6813	G_{13}= 3500	ν_{13} =0.48

2.2.3 Contact Properties between the Ring and the Flat Rigid Ground

Contact modeling is used to simulate the interaction between contact surfaces in ABAQUS [17]. Three steps should be followed to define a contact based simulation using ABAQUS/Standard [17]:

- Selection of the two geometric surfaces which may interact with each other, referred to as the "contact pair"
- A contact formulation should be created taking into account the following three key factors:
  - The contact discretization
  - The tracking approach
  - Assignment of the master and the slave roles to contact surfaces
- Contact properties such as mechanical, thermal, damping properties, etc, defined that determine the normal and tangential behavior between the two surfaces when they come in contact should be defined. In the normal direction the constraint

enforcement method and the pressure-overclosure relationship should be specified.

ABAQUS Standard follows a strict master slave weighting formulation i.e., the nodes of the master surface can penetrate into the slave surface, whereas the nodes of the slave surface are constrained not to penetrate into the master surface [17]. The analytical rigid flat surface is defined as the master surface for the reasons stated before and the deformable ring is defined as the slave surface. For the static analysis considered here, surface to surface contact interaction is used with the finite sliding tracking approach. Node to surface discretization is defined between the deformable outer membrane and the analytical rigid ground which comes in contact when loaded. The contact properties defined between the two contacting surfaces are:

- Tangential behavior: Frictionless contact is assumed
- Normal behavior: The direct enforcement method with hard pressure over-closure relationship is used since the goal is to predict an accurate contact pressure without any penetration or approximation. Hence this method strictly enforces the hard pressure-over closure behavior per constraint, minimizing the penetration of the master surface into the slave surface at the constraint locations and does not allow the transfer of tensile stress across the interface [17].

In this analysis the contacting surfaces are allowed to separate as they interact i.e., the surfaces separate if the contact pressure reduces to zero and they come into contact and develop a pressure when the clearance between them reduces to zero. Figure 2-3

shows the contact modeling and the two surfaces which are in point contact with each other before deformation.

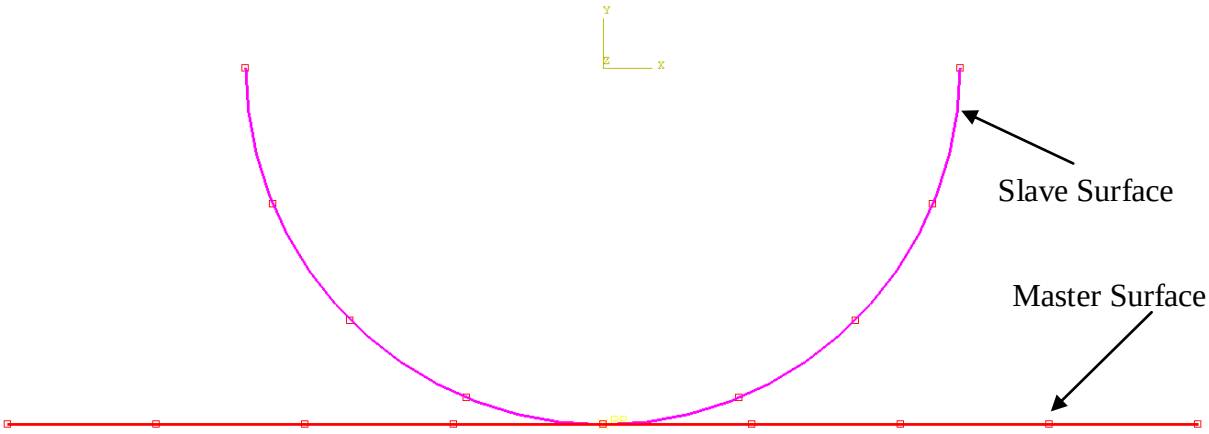

Figure 2-3: Contact interaction between the rigid plane and the ring before deformation

2.2.4 Meshing of the Ring

The goal here is to examine the convergence of the contact pressure, particularly with respect to the mesh. For beam theory, beam elements are used to mesh the ring in ABAQUS. Since contact is involved only the shear deformable, B21 first order beam element can be used from the ABAQUS element library. Although ABAQUS documentation suggests using only linear order Timoshenko beam element (B21) with contact, a second order Timoshenko beam element (B22) was used to check if convergence would be achieved. For the case of linear orthotropic elasticity, in plane stress case, the ring is meshed with the CPS4R elements, which is a reduced integration bilinear quadrilateral element, while in plane strain the CPE4R element is used, which is a reduced integration bilinear quadrilateral element. The second order bi-quadratic plane

stress quadrilateral plane stress element, CPS8R is used to check if convergence can be achieved better with second order. For the shell element the linear four node element S4R is used, which employs thick shell theory as the shell thickness increases and reduces to Kirchhoff thin shell elements as the thickness decreases, since the transverse shear deformation can be neglected as the structure becomes thin. The shell elements allow for a possible thickness change based on the material definition or by specifying effective section Poisson's ratio. The rigid ground is infinitely stiff and hence does not require meshing.

2.2.5 Mechanical Loads and Boundary Conditions

A general static step with large displacement formulation is defined for this contact problem which takes care of the boundary and geometry non linearity that may encountered while executing the analysis.

A force of 300N is applied at the center of the analytically rigid ground, which establishes contact between the ground and the ring. Since the ring is symmetric the horizontal centerline is allowed to move only in the transverse direction (x direction) and is restricted in other degrees of motion. The beam ring along with the rigid ground and boundary conditions are presented in Figure 2-4. The corresponding case where the ring has orthotropic elasticity properties is shown in Figure 2-5. The ring which employs the shell model is shown in Figure 2-6.

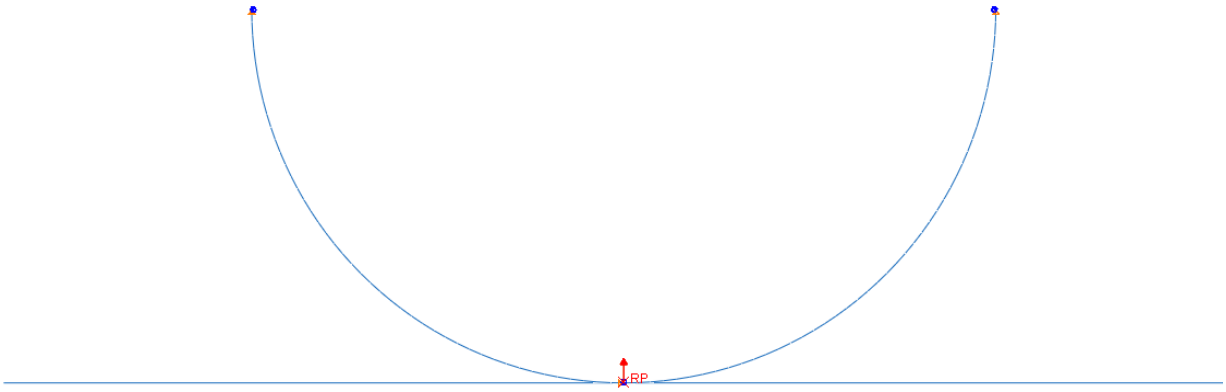

Figure 2-4: The beam model (B21 elements) with the defined boundary and the loading conditions

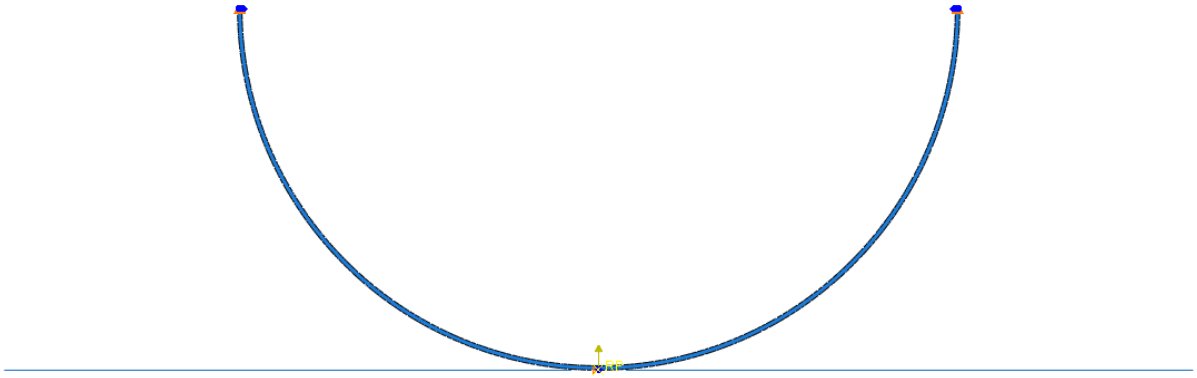

Figure 2-5: The orthotropic elasticity (CPS4R/CPE4R/CPS8R) model with the defined boundary and loading conditions

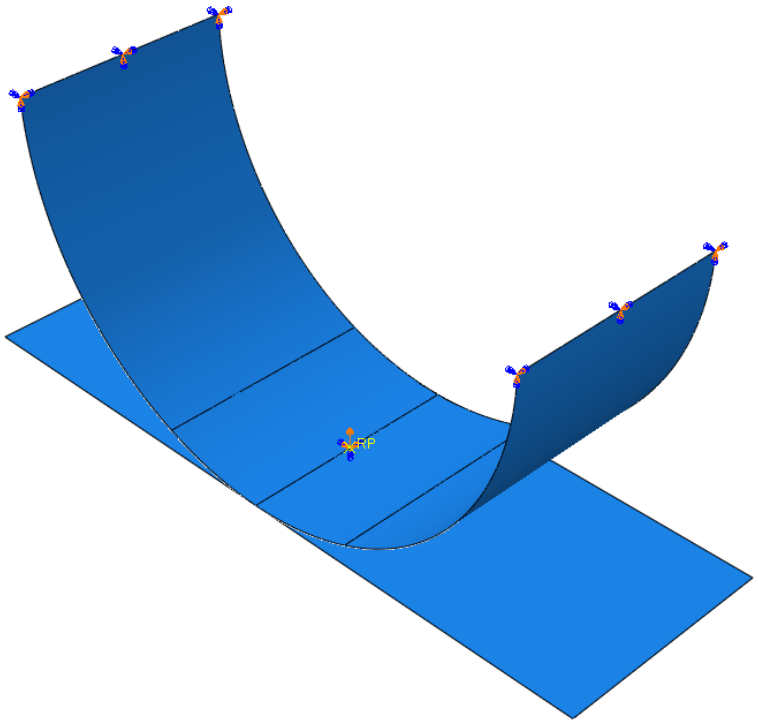

Figure 2-6: The half curved shell model (S4R) with the defined boundary and loading conditions

2.2.6 Results and Discussion

Static analysis of the half ring contacting the rigid ground was done and convergence was studied with respect to mesh refinement for both the beam theory and elasticity. Convergence was studied for three scalar parameters that represent the contact pressure, although the contact pressure distribution itself is the most important quantity:

- Integral of the pressure which should be equivalent to the load applied
- The contact patch length
- The contact pressure peaks

CASE 1: BEAM THEORY

The Table 2-2 shows the number of elements on the half beam for each mesh and the values of three of the convergence parameters. The numbers of elements are doubled for each case compared to the previous one.

Table 2-2: Convergence Study for the Beam ring (B21) for different mesh size

Number of elements on the Half ring	Integral of the Pressure [Reaction Force] (N)	Contact Length (mm)	Contact Pressure Peak (N)
1000	300.0050	67.858	61.2422
2000	300.0075	67.857	118.1320
4000	300.2913	67.8589	236.7940
8000	299.9536	67.855	390.9450
16000	300.3868	68.0502	738.9950
32000	299.3310	67.922	1039.50

Figure 2-7 shows the initial and the deformed configuration of the half beam ring in contact with the ground.

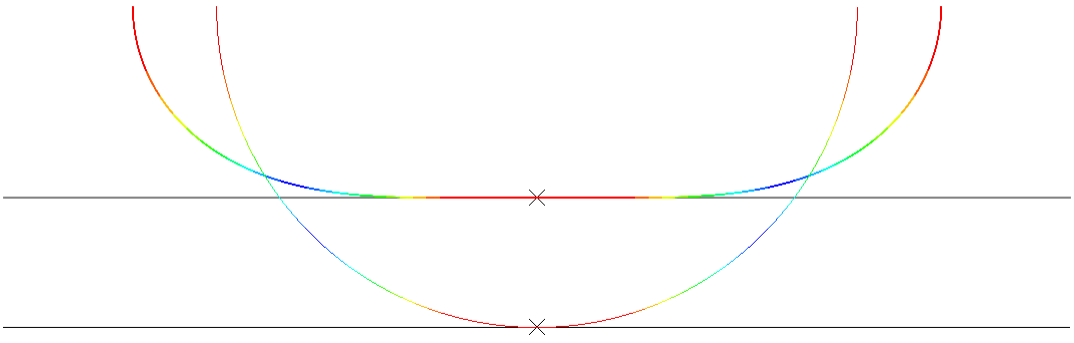

Figure 2-7: Initial and the deformed configuration of the half beam ring (B21)

To extract the contact pressure results, a path is defined around the ring which stores the value of the contact stress at every constraint point where contact was established. The contact pressure variable in ABAQUS is CPRESS and is plotted for each case of mesh refinement.

Figure 2-8 and 2-9 shows the contact pressure (MPa) plots for each case of mesh refinement. The force verses displacement plots are also plotted for each case of mesh refinement in Figure 2-10. The convergence parameter for contact pressure peak is plotted in Figure 2-11.

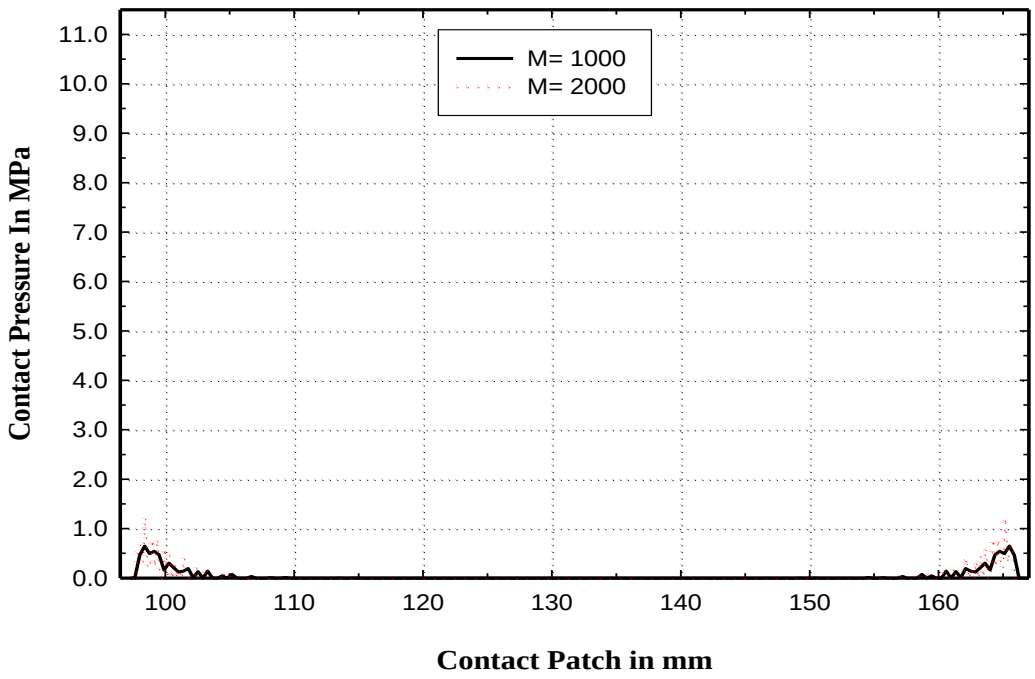

Figure 2-8: Mesh refinement plot of the contact pressure (MPa) for Beam elements (B21) for mesh M=1000 and M=2000

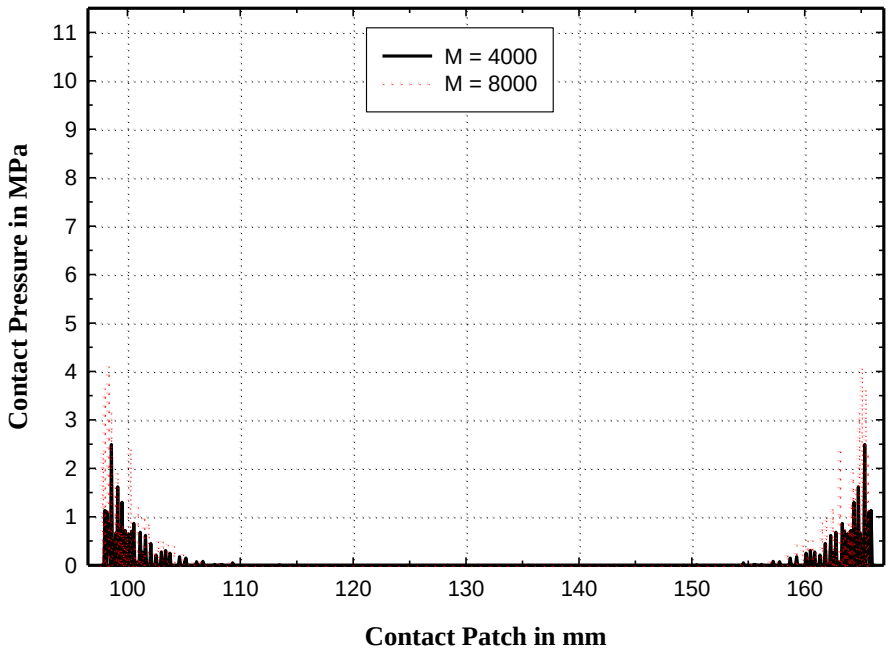

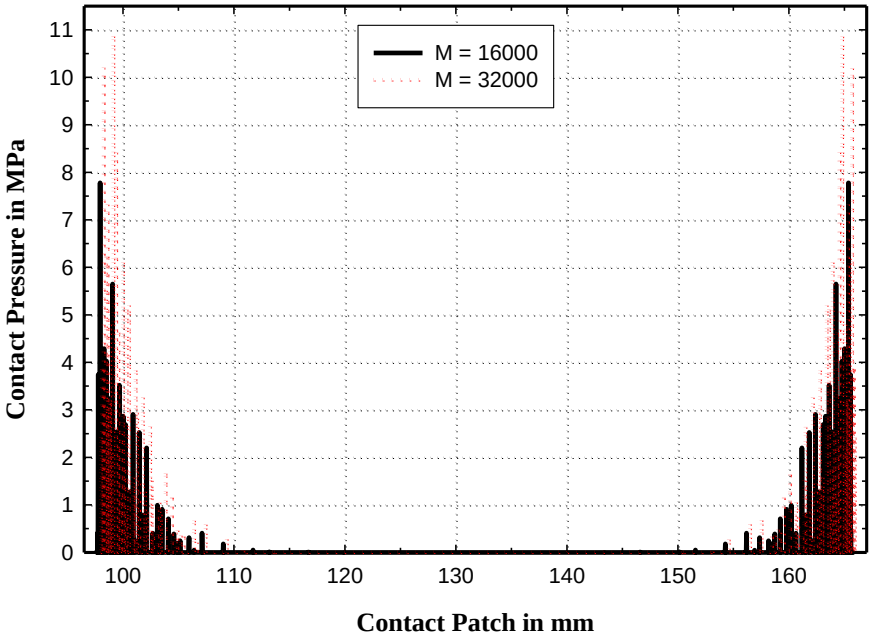

Figure 2-9: Mesh refinement plot of the contact pressure (MPa) for Beam elements (B21) for mesh M=4000 and M=8000 and M=16000 and M=32000 in the below plot

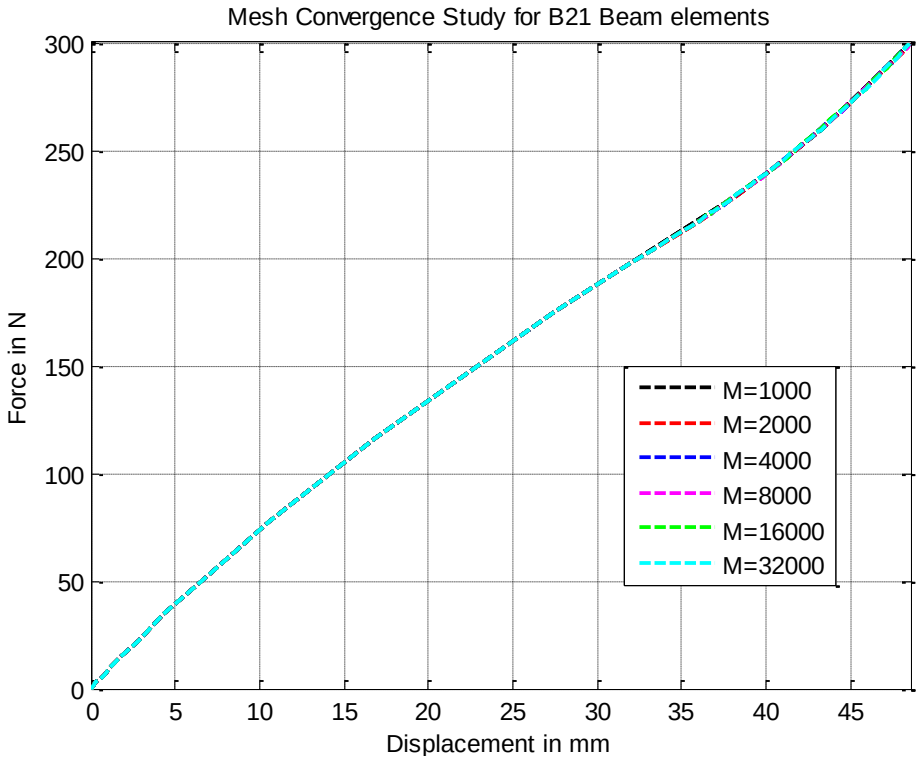

Figure 2-10: Force vs. Displacement plot for Beam elements (B21)

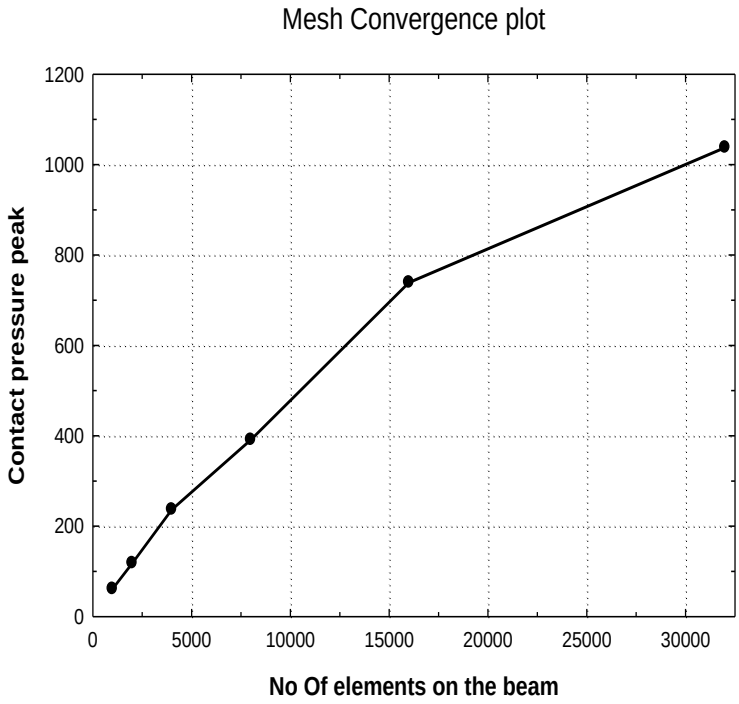

Figure 2-11: Contact Pressure peak for Beam elements (B21)

It is observed from Table 2-2 that the contact pressure peak values shoot up as the mesh is made finer. Although, the force displacement plots have converged the contact pressure does not converge to a unique profile as the number of elements is increased. The reason the contact pressure profile has not converged with respect to the mesh is that the ring is very stiff in shear and consequently the pressure has a very high gradient near the edge of contact. This difficulty was expected based on the previous analytical solution, although the inability of ABAQUS to converge with respect to mesh refinement was unanticipated. ABAQUS has difficulty in predicting the high pressure gradient. The contact pressure plots obtained using the higher order Timoshenko beam elements (B22) was found to be more unfavorable than the first order elements.

But another theory by Essenburg [12] and Naghdi and Rubin [13], mentioned that the addition of transverse shear deformation and bending deformation is not sufficient for prediction of accurate contact pressure since discontinuities may still appear in the contact pressure. The beam theory should also include the effect of transverse normal strains in addition to transverse shear deformation. The effect of transverse normal strain either in a beam / plate theory or elasticity is to include the surface deformations which ensure of the shear discontinuity approximation is eliminated and the pressure peak value at the edge of contact region immediately drops to zero outside the region. The beam elements (B21 or B22) here do not include the effect of transverse normal strain.

CASE 2: ORTHOTROPIC ELASTICITY

The Figure 2-12 shows the deformed configuration of the half elasticity ring in contact with the ground for one case of mesh refinement.

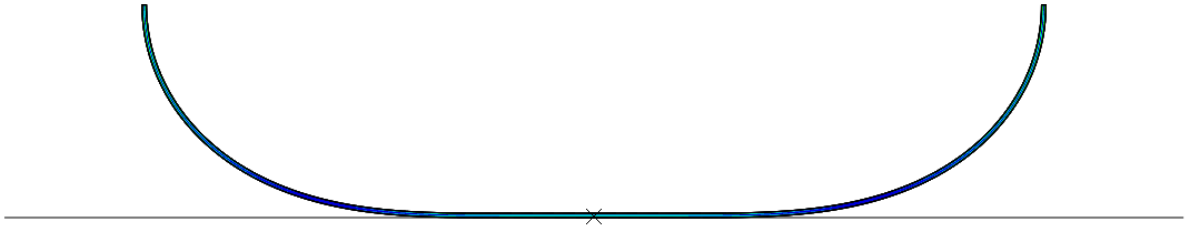

Figure 2-12: Deformed configuration of the half elasticity orthotropic ring

An aspect ratio of one is maintained for each element for each case of mesh refinement for all linear order plane stress/plane strain (CPS4R/CPE4R) and second order plane stress element (CPS8R) used.

LINEAR ORDER PLANE STRESS ELEMENTS - CPS4R

The Table 2-3 shows the number of elements on the half elasticity beam as the mesh is refined and the values for three scalar parameters. From the Table 2-3 and the contact pressure plots shown in Figure 2-13, the contact pressure peaks does not settle to a consistent value and contact pressure does not converge to a uniform profile. The force displacement plot is shown in Figure 2-14 for each case of mesh refinement.

Table 2-3: Convergence Study for the plane stress (CPS4R) for different mesh size

Number of elements on the Half ring (CPS4R)	Integral of the Pressure [Reaction Force] (N)	Contact Length (mm)	Contact Pressure Peak (N)	Number of elements in actual contact	Number of elements in the thickness direction
6250	300.2889	75.8705	83.7859	253	5
25000	300.5567	71.0139	120.2300	471	10
100000	304.6667	71.316	60.2888	943	20
400000	299.9989	71.01	73.7190	1875	40

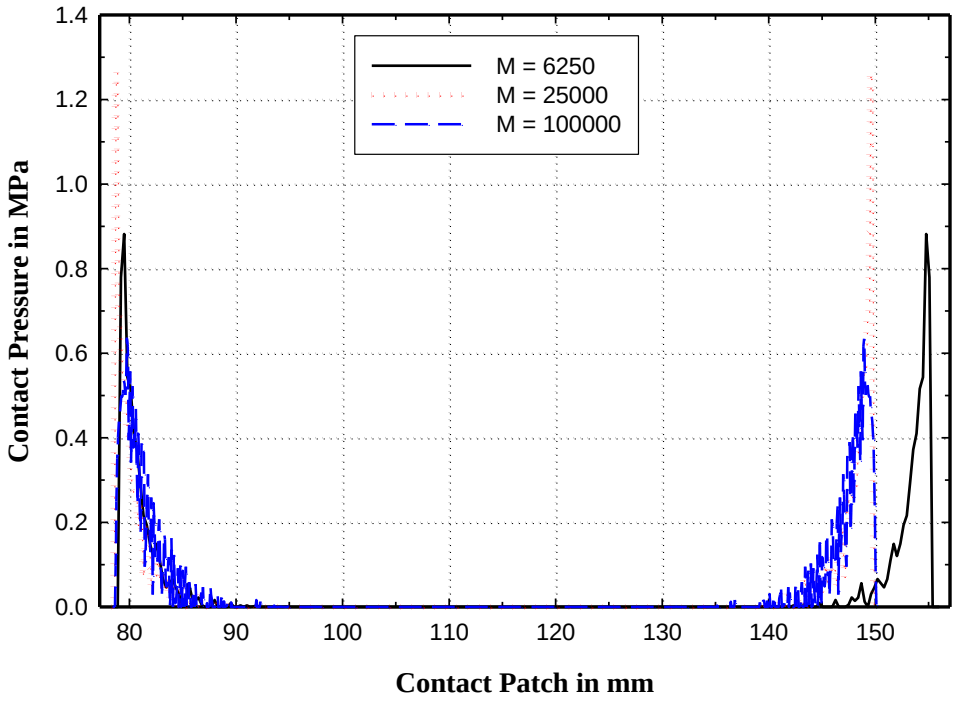

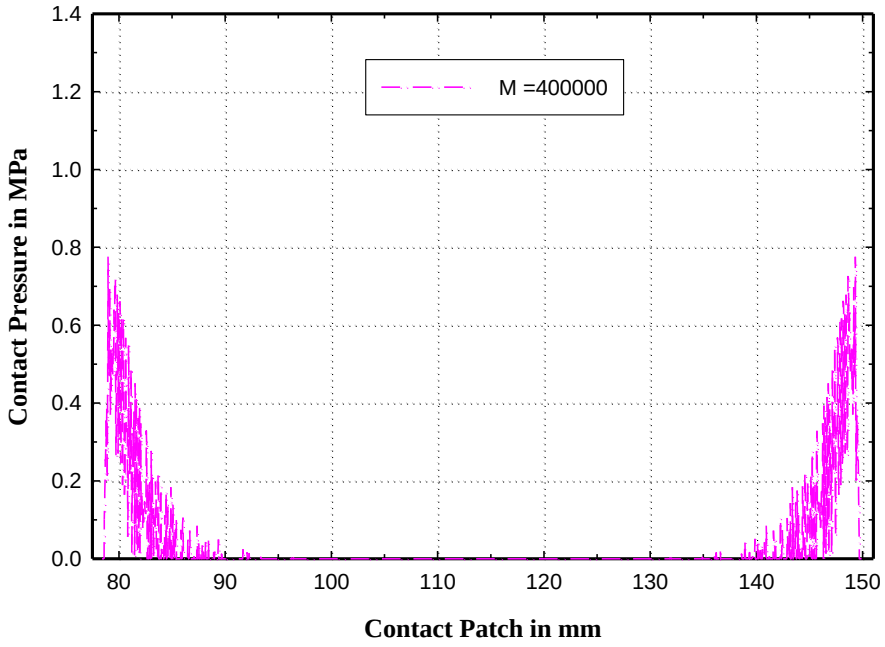

Figure 2-13: Mesh refinement plot of the contact pressure (MPa) for plane stress elements (CPS4R)

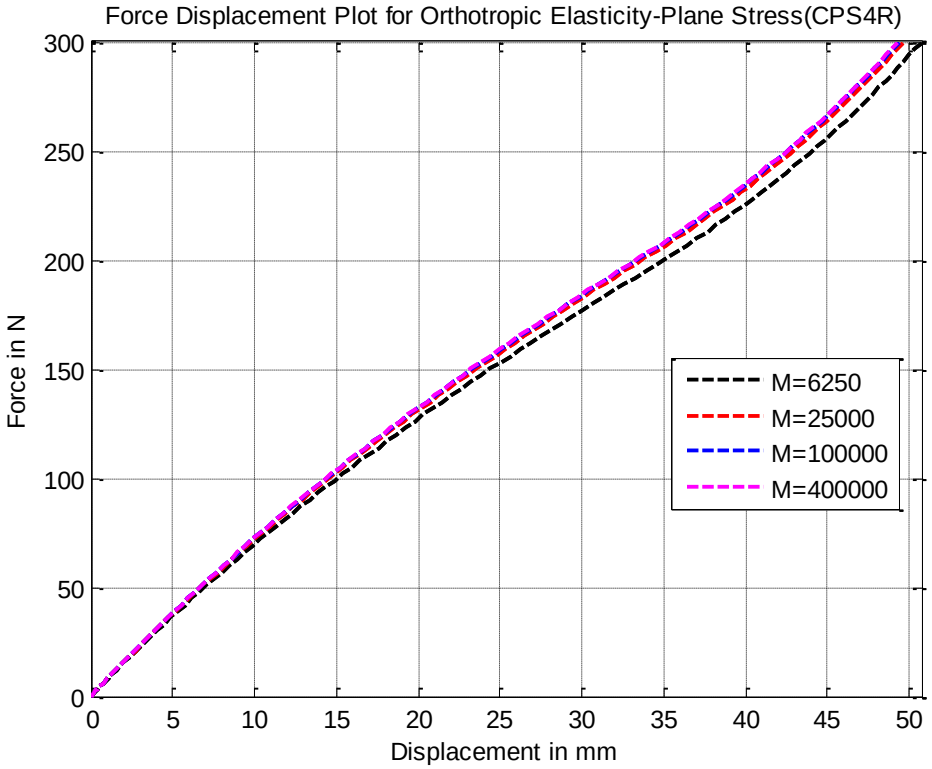

Figure 2-14: Force vs. Displacement plot for Plane Stress elements (CPS4R)

LINEAR ORDER PLANE STRAIN ELEMENTS - CPE4R

The Table 2-4 shows the number of elements on the half elasticity beam as the mesh is refined and the values for three scalar parameters for plane strain case. The results obtained are same as the plane stress case and the contact pressure plot shown in Figure 2-16 does not converge to a uniform profile. The force displacement plot is shown in Figure 2-15.

Table 2-4: Convergence Study for plane strain (CPE4R) for different mesh size

Number of elements on the Half ring (CPE4R)	Integral of the Pressure [Reaction Force] (N)	Contact Length (mm)	Contact Pressure Peak (N)	Number of elements in actual contact	Number of elements in the thickness direction
6250	300.0064	77.0836	54.8557	257	5
25000	299.9994	72.2286	56.1950	479	10
100000	300.0064	71.0116	64.6227	939	20

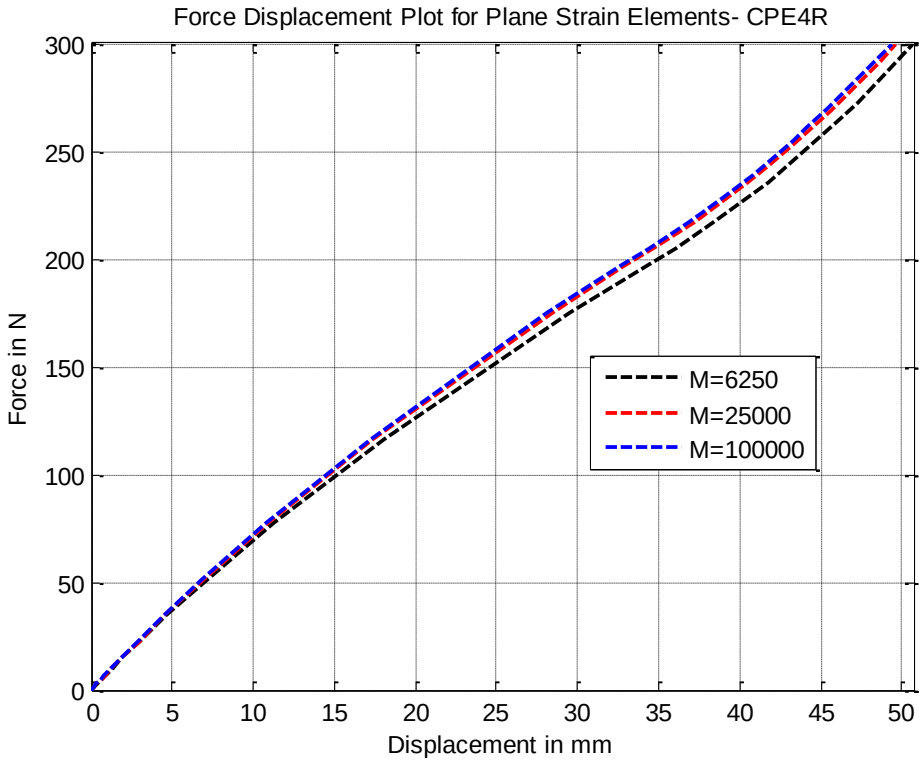

Figure 2-15: Force vs. Displacement plot for Plane strain elements (CPE4R)

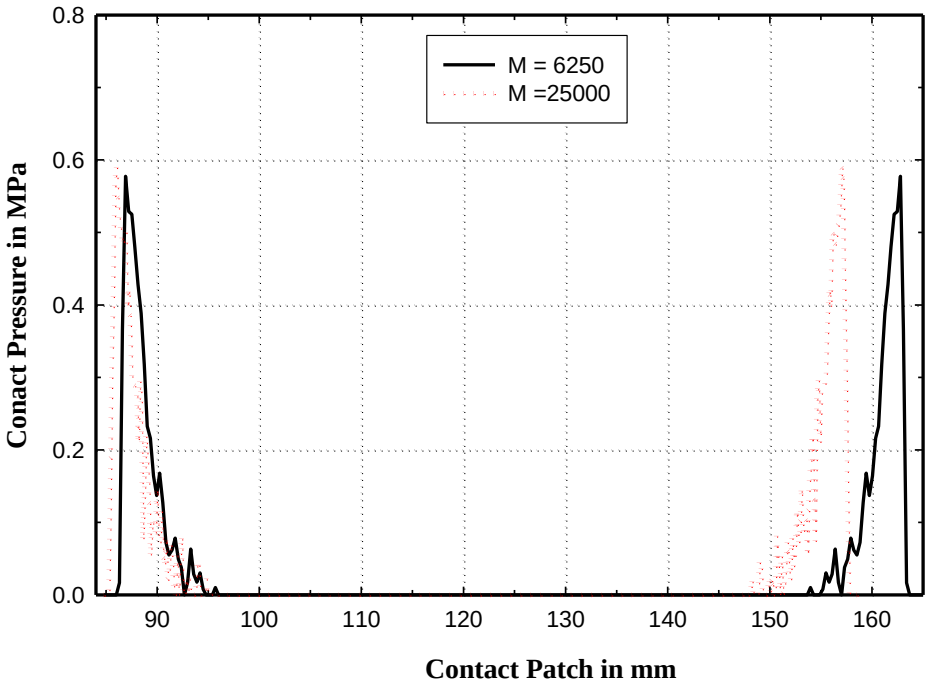

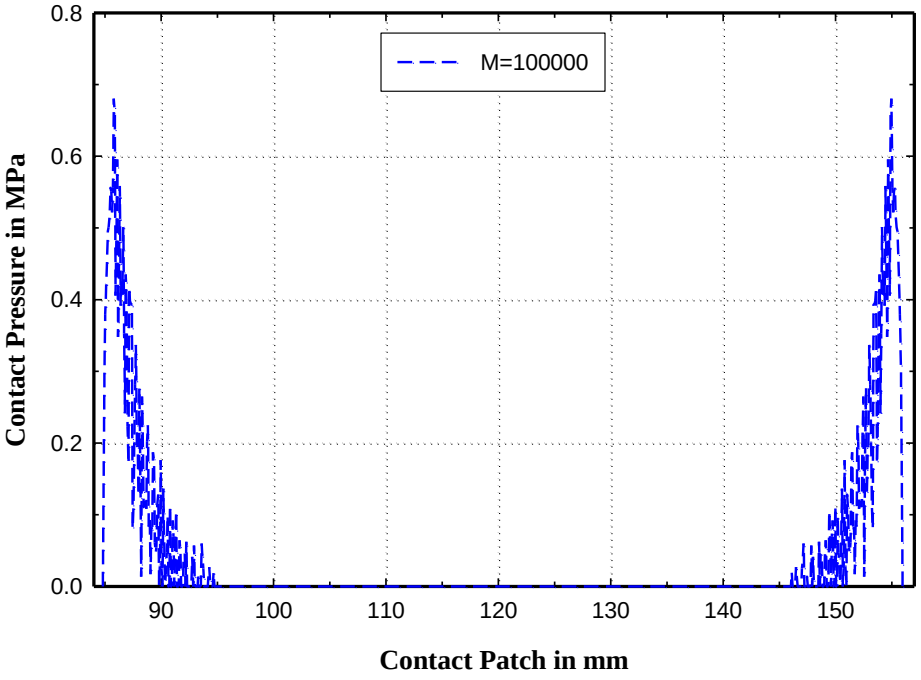

Figure 2-16: Mesh refinement plot of the contact pressure (MPa) for plane strain elements (CPE4R)

SECOND ORDER PLANE STRESS ELEMENTS - CPS8R

For orthotropic elasticity another mesh convergence study is done with higher order elasticity elements (CPS8R). The Table 2-5 shows the number of elements on the half elasticity beam as the mesh is refined and the values for three scalar parameters for CPS8R. Even here convergence is not achieved as shown in Figure 2-17. The force displacement plot is shown in Figure 2-18.

Table 2-5: Convergence Study for second order plane stress (CPS8R) for different mesh size

Number of elements on the Half ring (CPS4R)	Integral of the Pressure[Reaction Force] (N)	Contact Length (mm)	Contact Pressure Peak (N)	Number of elements in actual contact	Number of elements in the thickness direction
6250	304.6667	70.7104	62.9514	253	5
25000	306.8107	70.8602	84.0684	471	10
100000	313.8468	70.86	112.5900	943	20

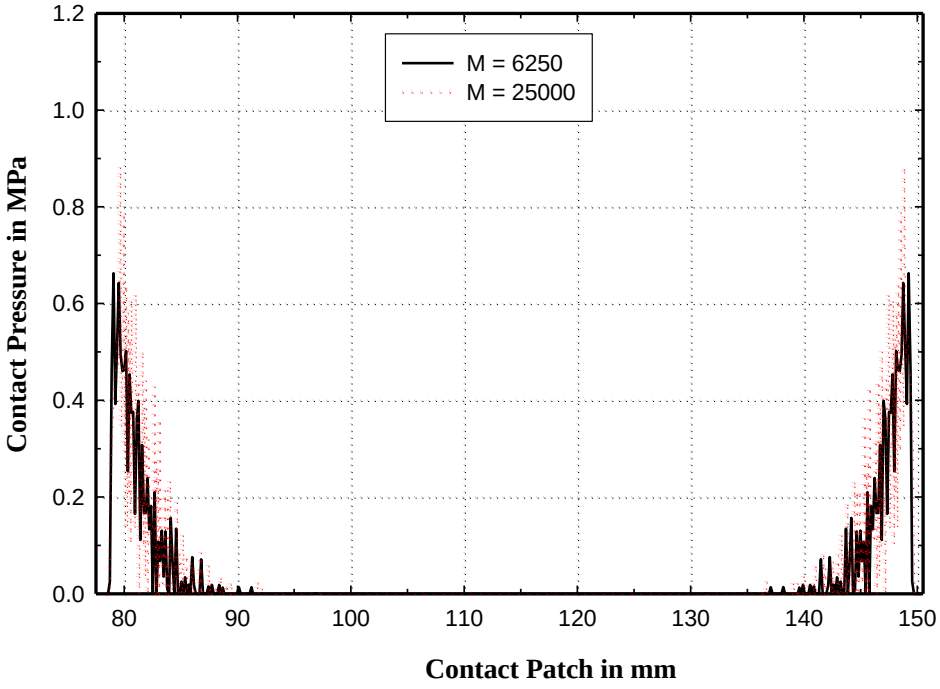

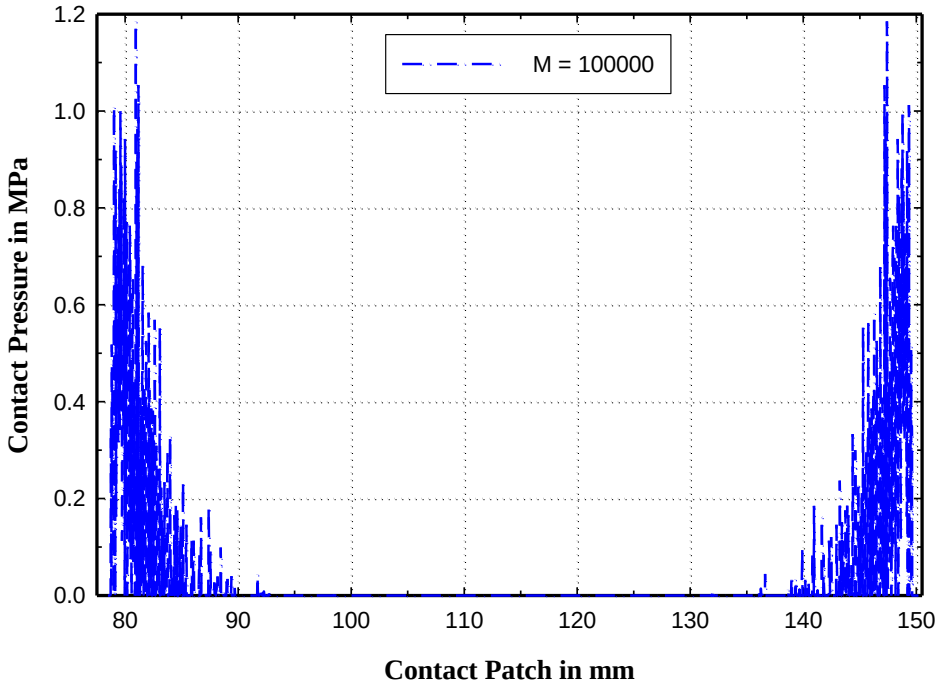

Figure 2-17: Mesh refinement plot of the contact pressure (MPa) for plane stress elements (CPS8R)

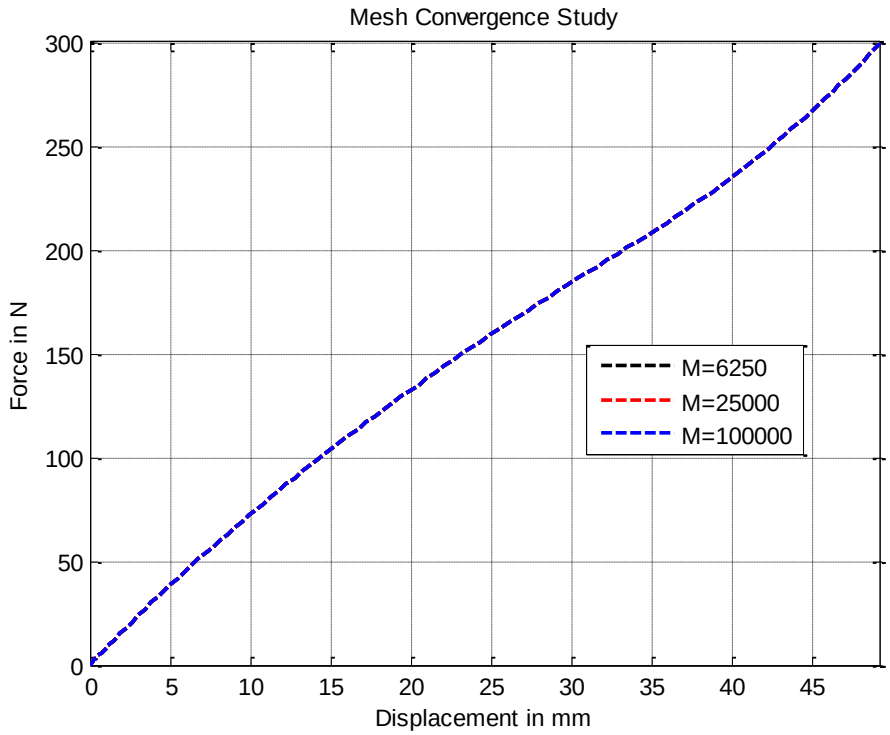

Figure 2-18: Force vs. Displacement plot for second order plane stress elements (CPS8R)

It is unexpected that ABAQUS cannot predict the high pressure gradient and converge to a unique profile either with linear order plane stress/plane strain or second order plane stress elasticity elements. The force displacement plot for the second order plane stress elements converge faster compared to the first order elements. It is also seen that the similar pattern of results is repeated for contact pressure is all the cases in ABAQUS.

CASE3: SHELL THEORY

The three dimensional shell is made two dimensional by making the Poisson's ratio in ν_{23} to zero .Since Poisson's ratio is defined as zero, the there are no lateral stresses and thus the CPRESS values would be constant in 2-3(y-z) direction. The Figure

2-19 shows deformed configuration of the half curved shell in contact with the ground for one case of mesh refinement. The table 2-6 shows the number of elements on the half curved shell as the mesh is refined and the values for three convergence parameters for S4R.

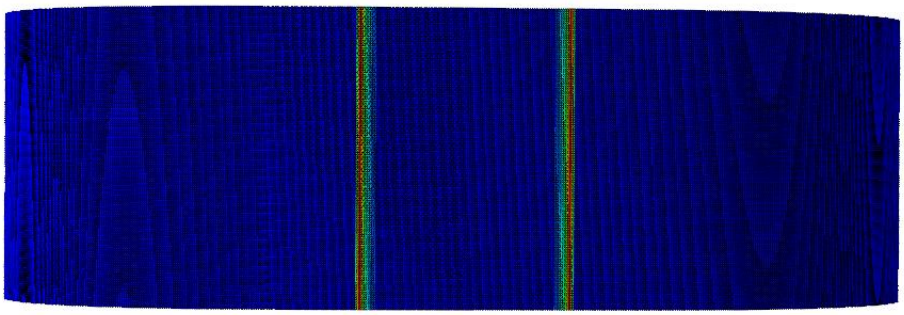

Figure 2-19: Deformed configuration of the half curved shell in contact (S4R)

Table 2-6: Convergence Study for the half curved shell (S4R) for different mesh size

Number of elements on the half curved shell (S4R)	Integral of the Pressure[Reaction Force] (N)	Contact Length (mm)	Contact Pressure Peak (N)
15500	300.0027	67.3654	56.6960
62500	300.0023	67.8583	52.3830
250000	300.0005	67.8584	61.0565

The contact pressure profile does not convergence to a unique profile as shown in Figure 2-20 as the mesh is refined. Since the thickness of the shell is thin, this shell element may not be even including the effect of the transverse shear deformation .The force displacement plot is shown in Figure 2-21.

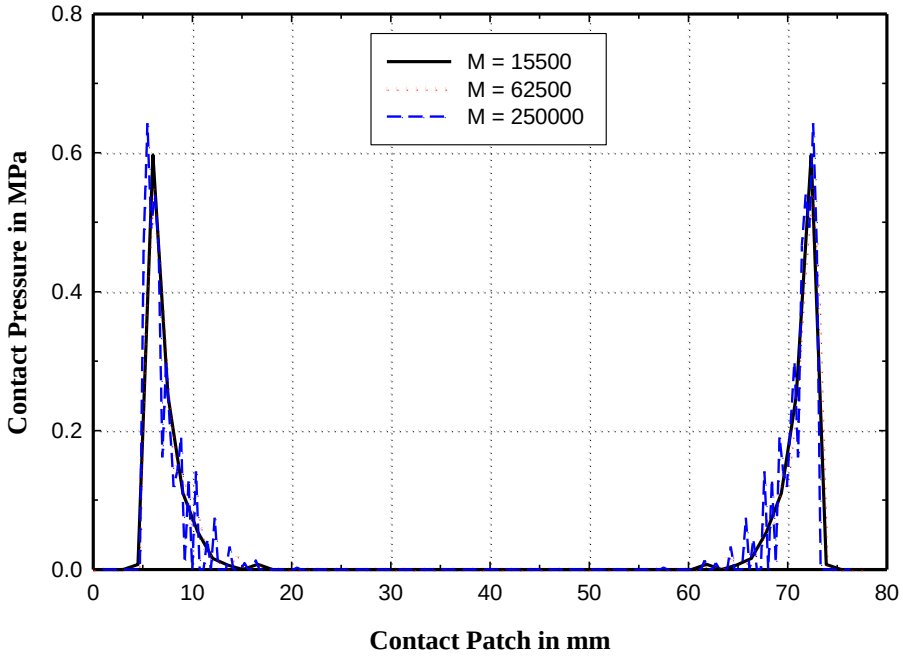

Figure 2-20: Mesh refinement plot of the contact pressure (MPa) for shell elements (S4R)

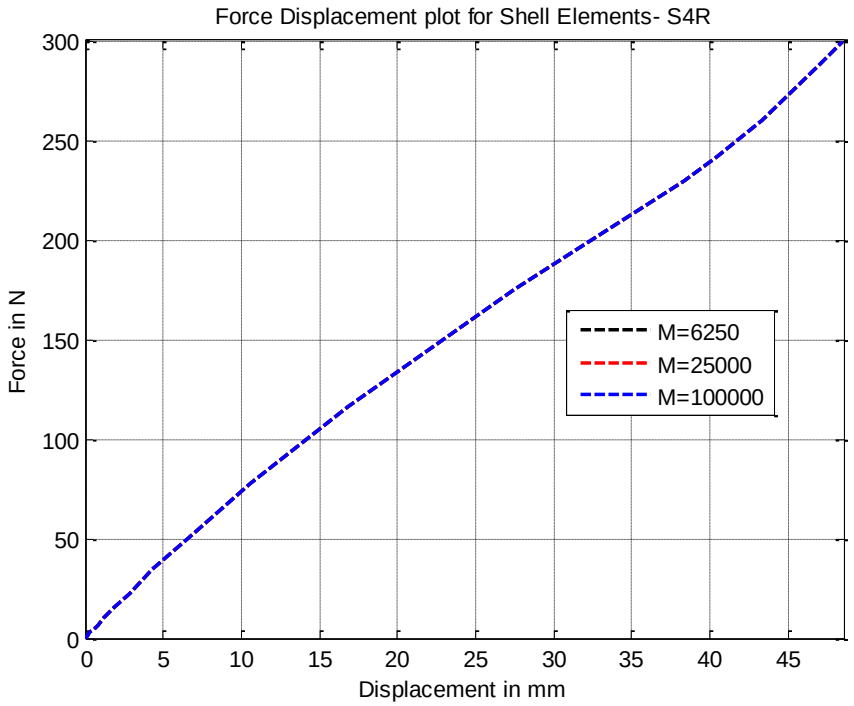

Figure 2-21: Force vs. Displacement plot for shell elements (S4R)

ABAQUS SUPPORT EXPLANATION

The below is a detailed summary explaining the problem of mesh convergence for the above problem.

In the analysis, a beam initially curved into a semi-circle is being pressed against a rigid surface, so that the beam gets flattened. The analytical solution in Block and Keer [12] suggests that the CPRESS distribution on the beam (specifically where the beam radius of curvature changes at the leading edge of the contact zone) should become a point force as the thickness of the beam reduces. The ABAQUS results show this feature of the solution, and as the mesh gets finer the CPRESS distribution gets a better and better representation of the spike. Here, the mesh refinement with respect to CPRESS distribution is trying to capture a spike as in the analytical solution. Apart from CPRESS, the mesh converges in the other results – reaction force, length of contact zone, etc.

The rules that apply to mesh convergence are centered on the ability of the finite element approximation to represent the actual solution. That is, how well the given discretization can replicate a polynomial expansion that fits the exact solution. In this problem, as the mesh is refined, the pressure peaks grow and the solution is also more oscillatory because a polynomial interpolation for the pressure distribution is trying to capture a spike. As the mesh is refined, there are more terms added in the approximation and oscillations are expected similar to Gibbs phenomenon where Fourier terms approximate spikes. The solution to the contact problem has both displacements and pressures as primary unknowns and the mesh convergence rules which applies in this case is a mixed finite element method using Lagrange Multipliers unlike conventional

displacement only finite element formulation. The pressures are interpolated typically with polynomials of one order lower than the displacements and the displacements are interpolated with polynomials of one order higher than the pressure. When these pressure interpolating polynomials approximate (in some least squares sense) the solution for thin beams that approach a singularity, oscillations are to be expected since the function does not include the singularity polynomial and hence there is drastic reduction in the rate of convergence explained by G. Strang and G. Fix [18] or by G. Strang [19]. Ideally, an FE approximation with polynomials will require an infinitely fine mesh to capture what is effectively a point force in the output.

An alternate way around this problem would be to model the ground itself as deformable but with a higher stiffness than the shell structure - it may lead to better convergence behavior than the current rigid ground-shell structure scenario.

ABAQUS also mentioned that there is no element in their element library which includes the effect of the transverse linear strain. The thickness change feature present in the shell element is only a Poisson's effect.

CHAPTER THREE

ADDING A COMPLIANT LAYER ON THE RING

To overcome the issue of convergence of contact pressure in ABAQUS, a soft compliant layer, or tread, is added to the outer perimeter of the ring. Adding this soft layer as an elastic continuum will address the problem of the ring being very stiff in shear that causes very high pressure gradients at the edges of contact. The focus of the work in this chapter is to identify a value of thickness of the compliant layer which would enable ABAQUS to converge and give unique converged contact pressure profiles as the mesh is refined. The geometry, material properties, analysis type, boundary and loading conditions of the ring are the same as those of Chapter II. The compliant layer is added on the outer surface of the ring by using 'surface based tie constraints' in ABAQUS.

3.1 ABAQUS Solution for the Ring with the Compliant Layer

3.1.1 Model Geometry

The compliant layer is added to the outer surface of the ring, which is pressed between two frictionless plates as shown in Figure 3-1. For this study, a thickness of $1/10^{th}$ the thickness of the ring (t_r =1.5mm, t_c = 0.15mm) was used for the compliant layer to observe if convergence can be achieved. Hence the inner diameter of the compliant layer was taken to be D_c= 240 mm and the outer diameter was D_o=240.15 mm. The layer thickness was then increased to study the sensitivity of the contact pressure.

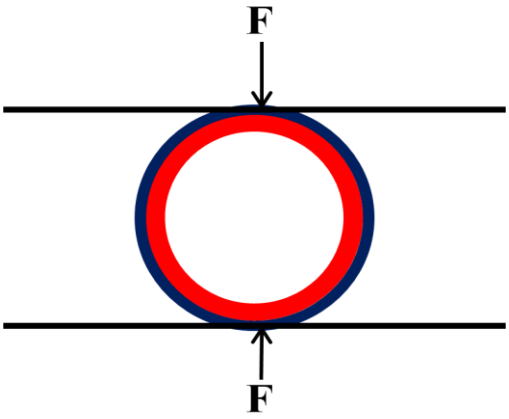

Figure 3-1: Ring with compliant layer pressed between two parallel frictionless plates

3.2.2 Material Properties of the Compliant Layer

For the compliant layer, an isotropic material having a stiffness of 1/1000th of the circumferential stiffness (E_{layer} = 500 MPa, ν = 0.3) of the ring is used. This is a reasonable value for the stiffness of a tread, such as the leather that was considered as a tread material for lunar applications.

3.1.3 Multipoint Constraints

The ring and the compliant layer were modeled as separated parts and are connected using ABAQUS multi-point constraints. The outer surface of the ring is tied to the inner surface of the compliant layer using 'surface based tie constraints' as shown in Figure 3-2. Therefore, physically, the entire outer surface of the ring is bonded to the compliant layer.

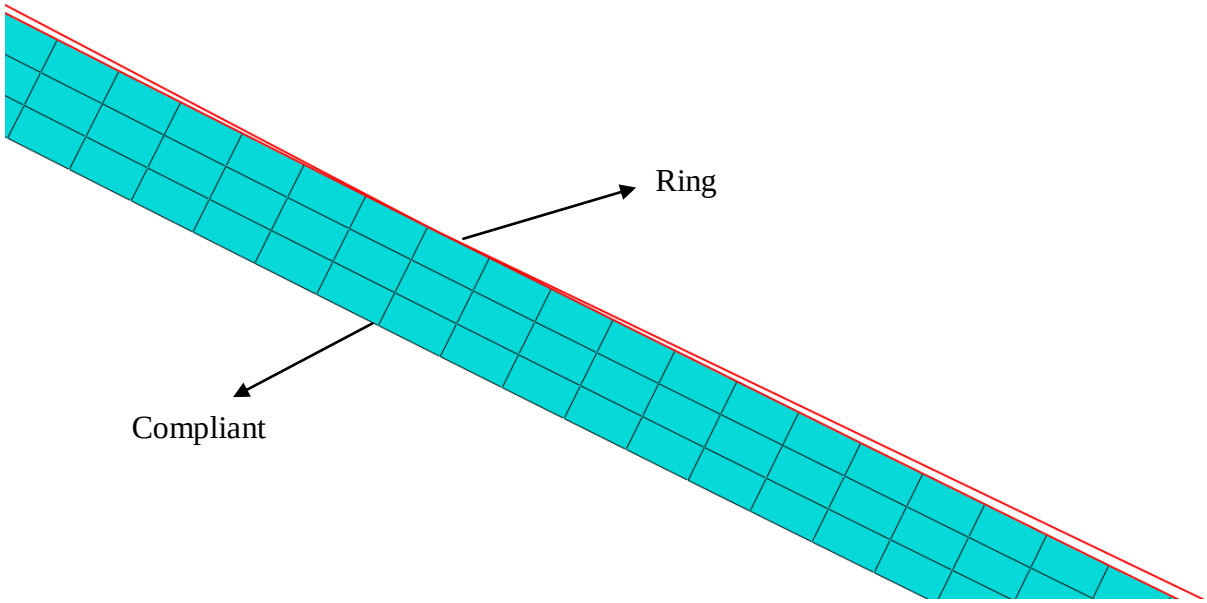

Figure 3-2: Section of the ring and the compliant layer

3.1.4 Contact Properties between the Compliant Layer and the Flat Rigid Ground

The analytical rigid flat surface is defined as the master surface and the compliant layer is defined as the slave surface. The contact formulation and contact properties continue to be the same as those described in Chapter II.

3.1.5 Meshing the Ring and the Compliant Layer

The ring is meshed with linear beam elements (B21) and the compliant layer is meshed with plane strain elements (CPE4R). The numbers of elements used in the compliant layer and the ring are varied to study convergence of the contact pressure. As in Chapter 2, the elements are taken to be square in shape.

3.1.6 Mechanical Loading and Boundary Conditions

A force of 300N is applied at the center of the analytically rigid ground, which establishes contact between the ground and the deformable compliant layer. Since the compliant layer is bonded to the ring and is symmetric, the horizontal centerline is allowed to move only in the transverse direction (x direction) and is restricted in other degrees of motion. The ring with the compliant layer and rigid ground with the boundary conditions are presented in Figure 3-3.

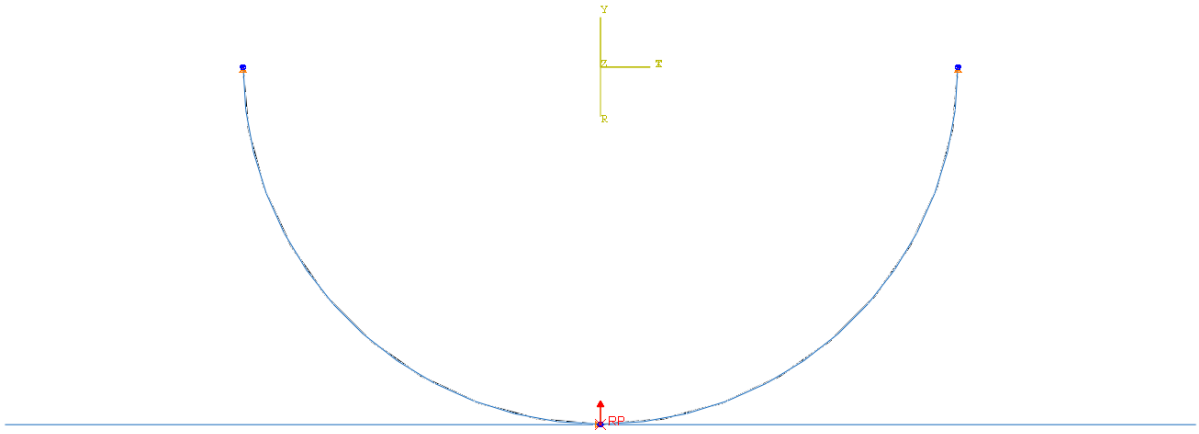

Figure 3-3: The model with the defined boundary and the loading conditions

3.1.7 Results and Discussion

A static analysis of the ring attached to the compliant layer contacting the rigid ground was performed and convergence with respect to mesh refinement of the ring and compliant layer was studied. The thickness of the compliant layer was then varied to study the sensitivity of the contact pressure. Two cases of thickness were studied:

- CASE 1 = Thickness of compliant layer $t_c = 0.15$ mm

- CASE 2 = Thickness of compliant layer t_c = 0.25 mm

For each of the above cases, the following two sub cases were studied:

- SUBCASE 1: The number of elements was varied on the ring keeping the number of elements on the compliant layer constant.
- SUBCASE 2: The number of elements was varied on the compliant layer keeping the number of elements on the ring constant.

The Figure 3-4 shows the deformed configuration of the half ring with the compliant layer in contact with ground.

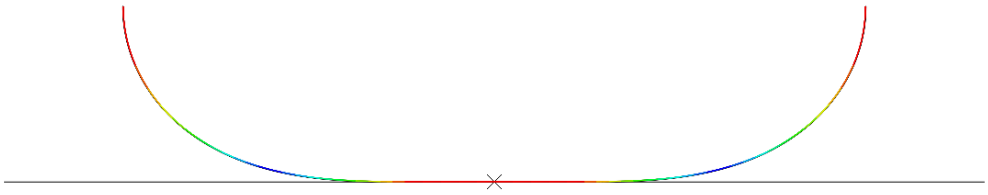

Figure 3-4: Deformed configuration of the half ring with the compliant layer (thickness =0.15 mm)

To extract the contact pressure results, a path is defined around the compliant layer which stores the value of the contact stress at every node where contact was established.

CASE 1: Thickness of the compliant layer 0.15mm

While the contact pressure is the most important quantity to evaluate convergence, the following three scalar parameters that represent the contact pressure where also studied for convergence:

- Integral of the pressure which should be equivalent to the load applied
- The contact patch length
- The contact pressure peaks

➢ Subcase 1

The Table 3-1 shows the values for three scalar parameters for sub case 1 where the thickness of the compliant layer is 0.15mm. Figure 3-5 and 3-6 shows the contact pressure (MPa) plots for subcase1 for the same cases of mesh count used for Table 3-1. The force verses displacement plots are also plotted for subcase 1 in Figure 3-7 and 3-8.

Table 3-1: Convergence Study for Subcase 1 where the thickness of the compliant layer = 0.15mm (a) No of Elements on the Compliant Layer = 2500 (b) No of Elements on the Compliant Layer = 10000 (c) No of Elements on the Compliant Layer = 40000

No of Elements on the Compliant Layer = 2500 (Aspect ratio 1)			
No of Elements on the Ring	Integral of the Pressure [Reaction Force] (N)	Contact Length (mm)	Contact Pressure Peak (N)
1000	300.0002	69.3666	41.6124
2000	300.0032	69.3674	41.5950
4000	300.0043	69.367	41.5841
8000	300.0017	69.3665	41.5735

(a)

No of Elements on the Compliant Layer = 10000 (Aspect ratio 1)			
No of Elements on the Ring	Integral of the Pressure [Reaction Force] (N)	Contact Length (mm)	Contact Pressure Peak (N)
1000	299.9952	69.3649	42.3784
2000	299.9924	69.3665	42.3832
4000	299.9947	69.3663	42.3812
8000	299.9857	69.3651	42.3793

(b)

No of Elements on the Compliant Layer = 40000 (Aspect ratio 1)			
No of Elements on the Ring	Integral of the Pressure [Reaction Force] (N)	Contact Length (mm)	Contact Pressure Peak (N)
1000	300.0083	69.2966	43.2668
2000	300.0109	69.2914	43.2739
4000	300.0123	69.2917	43.2739
8000	300.0098	69.2928	43.2738

(c)

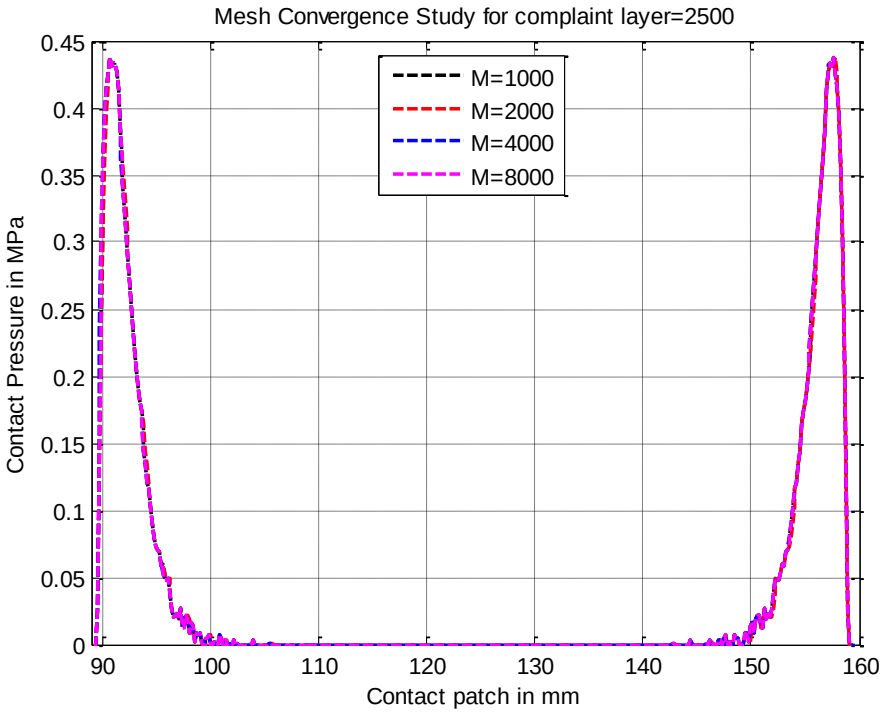

(a)

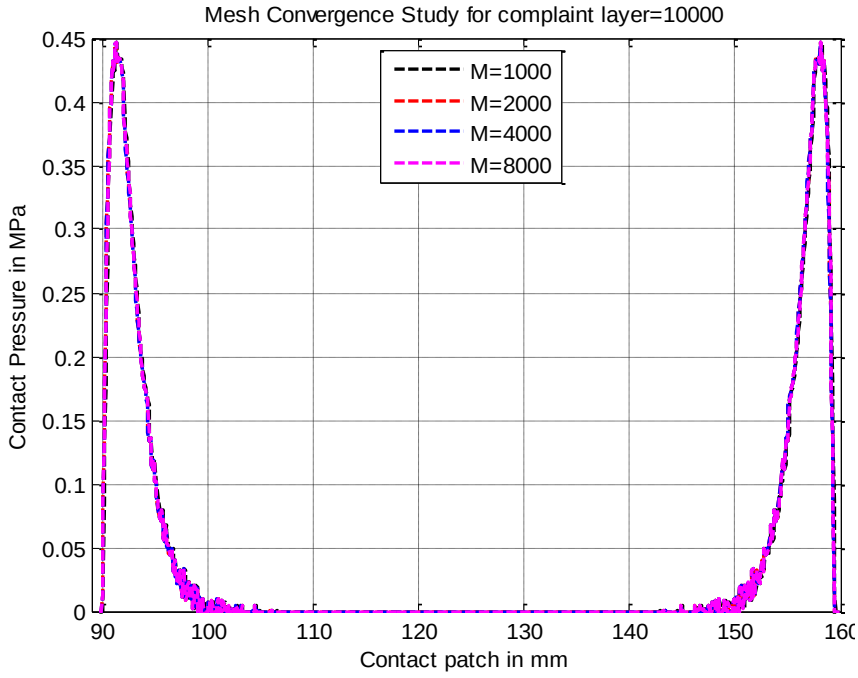

(b)

Figure 3-5: Contact pressure (MPa) for Subcase 1- t=0.15mm (a) No of Elements on the Compliant Layer = 2500 (b) No of Elements on the Compliant Layer = 10000

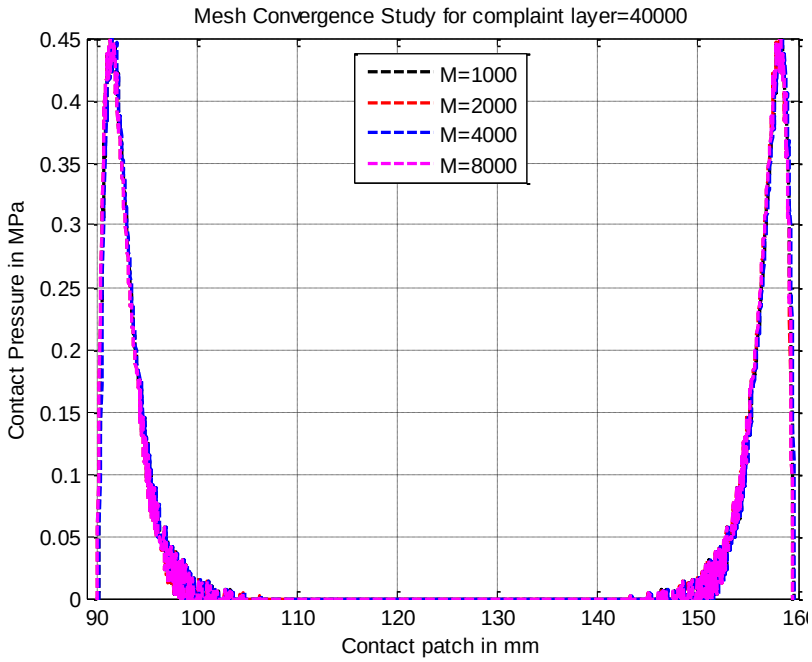

(c)

Figure 3-6: Contact pressure (MPa) for Subcase 1- t=0.15mm (c) No of Elements on the Compliant Layer = 40000

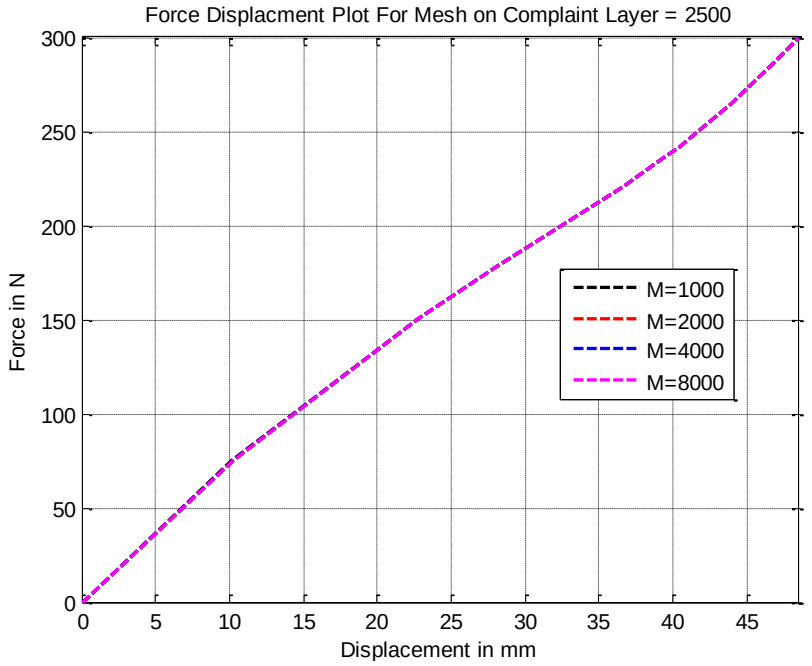

(a)

Figure 3-7: Force vs. Displacement Plots for Subcase 1 - t=0.15mm (a) No of Elements on the Compliant Layer = 2500

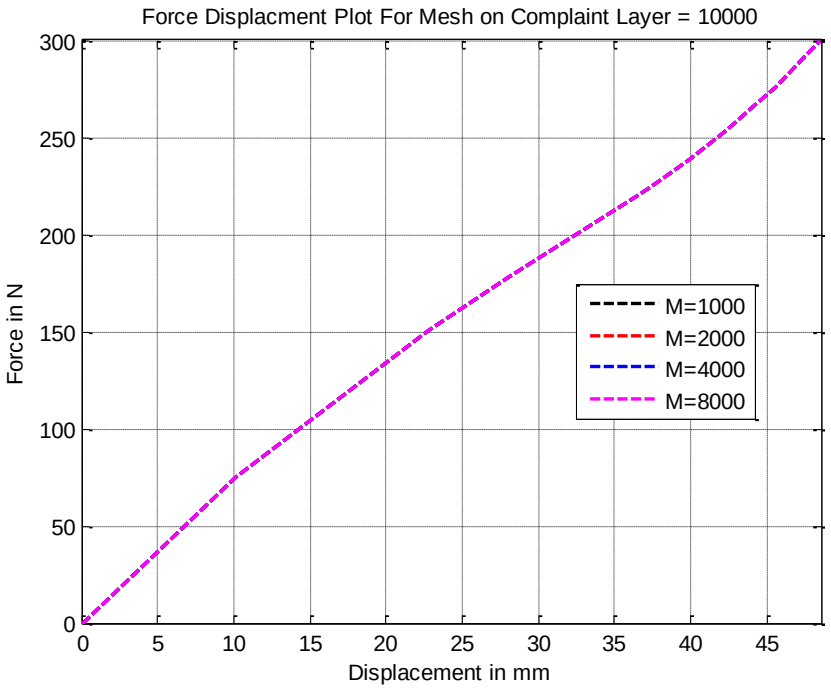

(b)

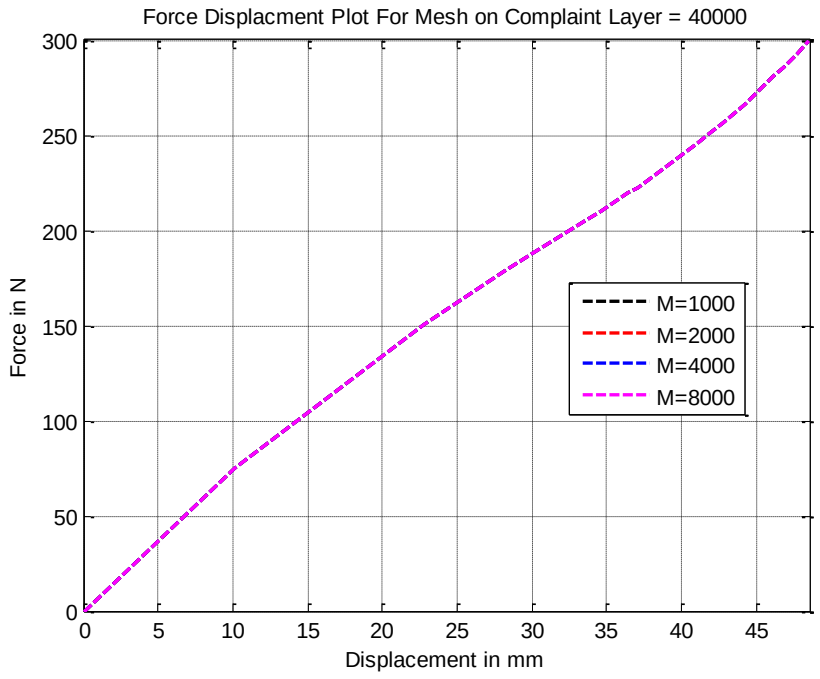

(c)

Figure 3-8: Force vs. Displacement Plots for Subcase 1 - t=0.15mm (b) No of Elements on the Compliant Layer = 10000 (c) No of Elements on the Compliant Layer = 40000

From the contact pressure plots and from the Table 3-1 it is observed that the scalar parameters are almost constant when the number of elements on the ring is varied. The contact pressure profile is smooth and converges to a constant profile unlike the contact pressure plots in the previous chapter in the absence of the compliant layer. Hence ABAQUS is able to predict a finite value of pressure at the edge of contact. The subcase 2 was tested and convergence was achieved similar to that of sub case 1, and therefore the results are not presented.

CASE 2: Thickness of the compliant layer 0.25 mm

- Subcase 1

The Table 3-2 shows the values for three scalar parameters for subcase 1 where the thickness of the compliant layer is 0.25mm. Figure 3-9 shows the contact pressure (MPa) plots for subcase 1. The force verses displacement plots are also plotted for subcase 1 in Figure 3-10.

Table 3-2: Convergence Study for Subcase 1 where the thickness of the compliant layer = 0.25mm (a) No of Elements on the Compliant Layer = 6000 (b) No of Elements on the Compliant Layer = 24000

No of Elements on the Compliant Layer = 6000 (Aspect ratio 1)			
No of Elements on the Ring	Integral of the Pressure [Reaction Force] (N)	Contact Length (mm)	Contact Pressure Peak (N)
1000	300.0192	69.6189	38.5284
2000	299.4148	69.619	38.4510
4000	299.4149	69.619	38.4458
8000	299.4140	69.6191	38.4435

(a)

No of Elements on the Compliant Layer = 24000 (Aspect ratio 1)			
No of Elements on the Ring	Integral of the Pressure [Reaction Force] (N)	Contact Length (mm)	Contact Pressure Peak (N)
1000	299.3869	69.6204	39.1164
2000	299.3918	69.6204	39.1169
4000	299.3916	69.6202	39.1168
8000	300.0107	69.6203	39.1973

(b)

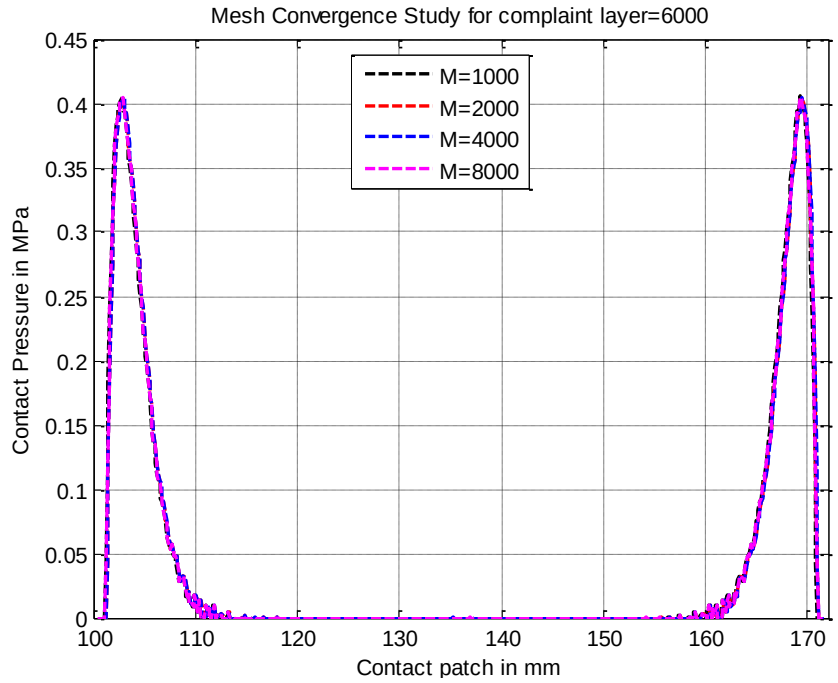

(a)

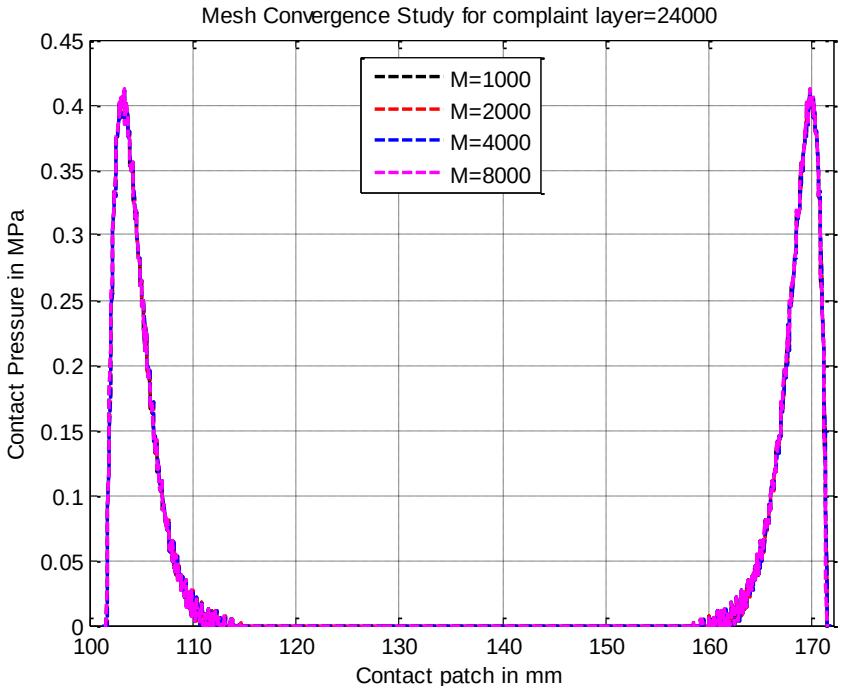

(b)

Figure 3-9: Contact Pressure (MPa) plot for Subcase 1- t=0.25mm (a) No of Elements on the Compliant Layer = 6000 (b) No of Elements on the Compliant Layer = 24000

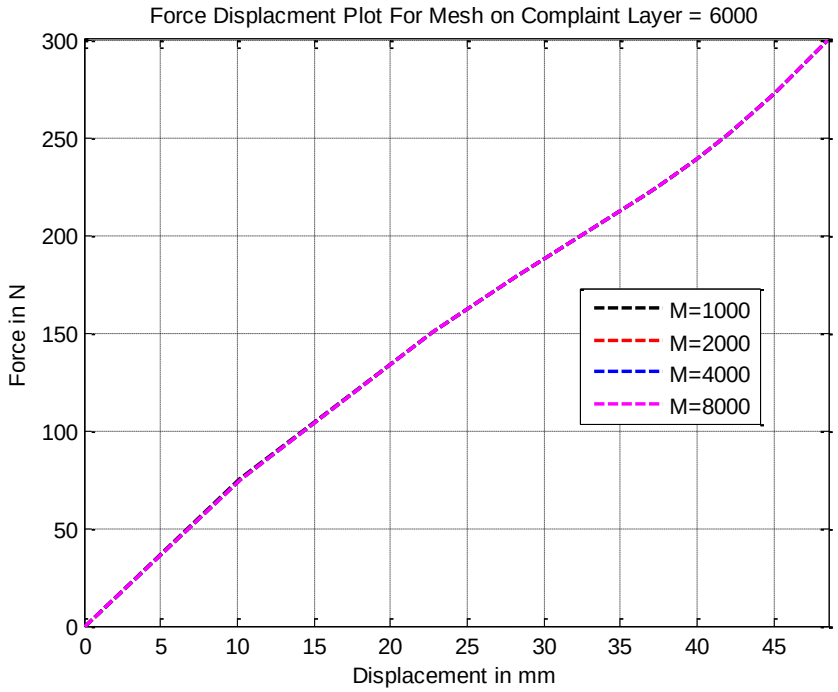

(a)

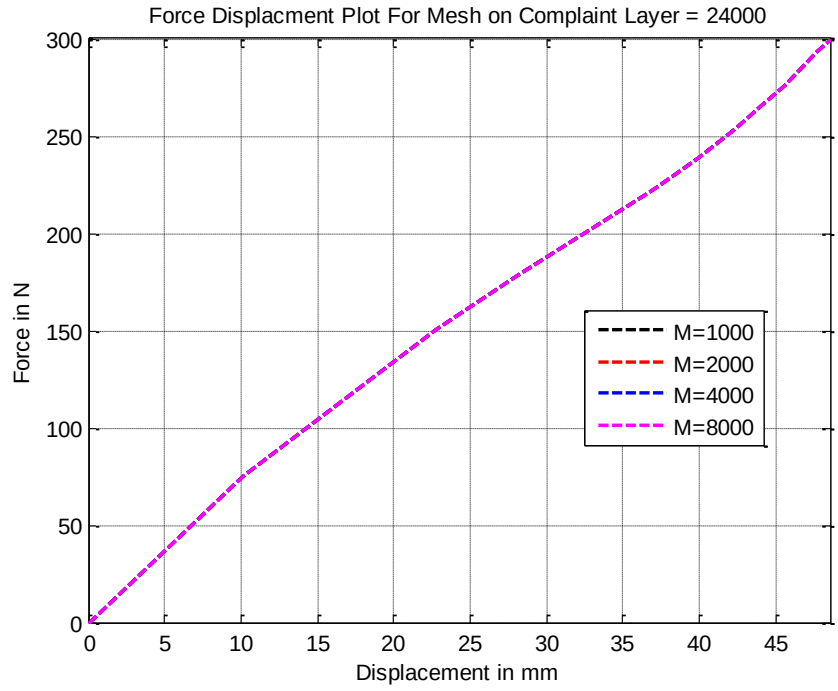

(b)

Figure 3-10: Force vs. Displacement Plots for Subcase 1 - t=0.25mm (a) No of Elements on the Compliant Layer = 6000 (b) No of Elements on the Compliant Layer = 24000

It is observed here that as the thickness is increased the contact pressure profile become smoother and the value of the contact pressure peak drops compared to the previous thickness t_c = 0.15 mm. Since ABAQUS does have an element which accounts for the transverse linear strain it is concluded that using a tread of a very small thickness and reasonable stiffness helps is achieving a converged contact pressure profile in ABAQUS.

3.1.8 Reasons for Achieving Convergence with a Compliant Layer:

When a compliant layer of thickness 0.15 mm is added to the outer perimeter of the ring and the composite ring is pressed between two rigid surfaces, the compliant layer must follow the contact boundary condition given in Equation 5-1, and deform into a straight line in the region of contact. But the compliant layer allows the beam to deform into a shape that is slightly different from a perfect circle, which allows the ring to avoid the sharp spike in pressure. This behavior is demonstrated in Figures 3-11 and 3-12. The plots in Figure 3-11 are for the ABAQUS displacements of the ring and compliant layer within the contact area, compared to the displacement boundary condition for the compliant layer given by Equation 5.1, where the δ_0 value is obtained from ABAQUS. More importantly, the difference between these displacements for both the outer surface and the compliant layer and the outer surface of the ring are presented in Figure 3-12. This difference is approximately zero for the compliant layer, which validates the solution of the contact problem. However, the difference for the ring shows a non-zero deviation from being flat, which corresponds to the slight deviation from changing a

circle to a straight line. This slight deviation enables ABAQUS to converge and shows just how sensitive the pressure is to flattening a circular shape.

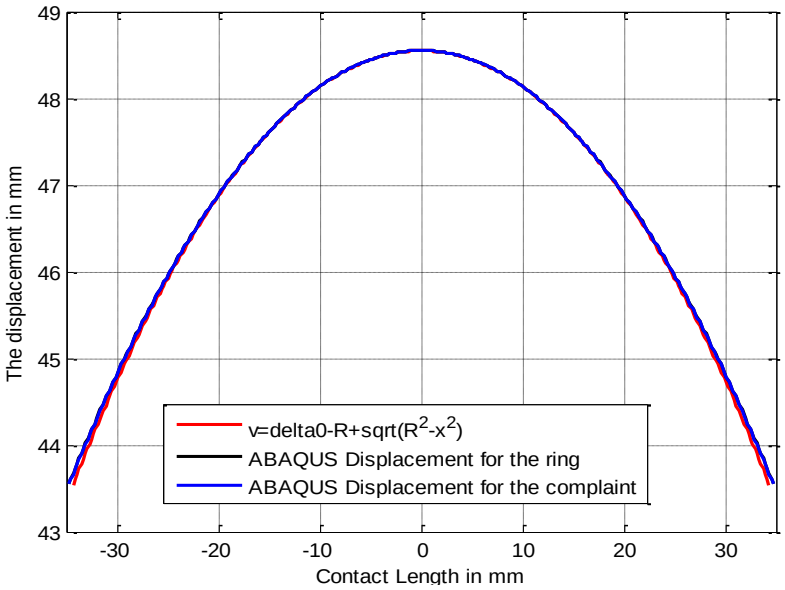

Figure 3-11: Displacement of the ring within the contact area compared to the displacement boundary condition for the 0.15 mm thick compliant layer.

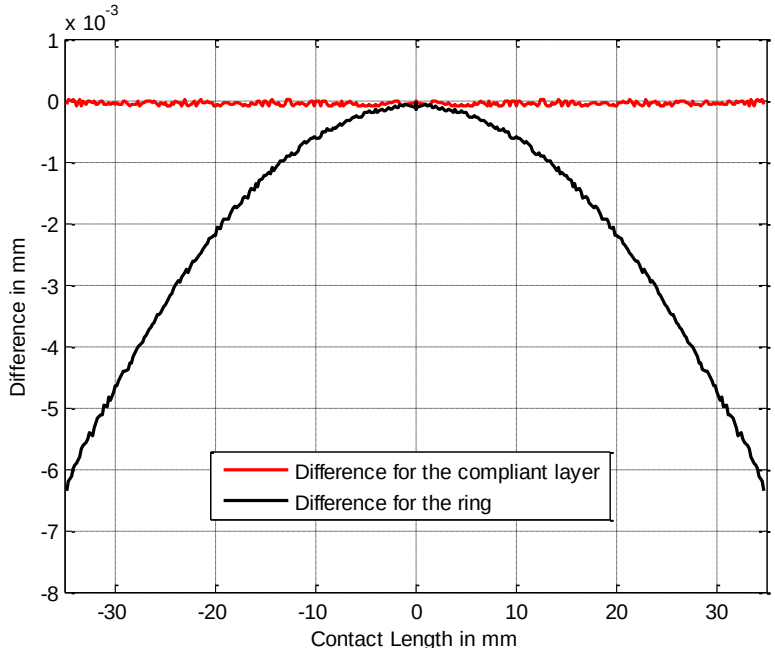

Figure 3-12: Differences (obtained from Figure 3-11) between the contact boundary condition (Eqn. 5.1) and the deformed shapes of the ring and compliant layer obtained by ABAQUS. These differences correspond to the deviation from being flat.

CHAPTER FOUR

TWO DIMENSIONAL FINITE ELEMENT MODEL OF THE FIRST GENERATION MICHELIN LUNAR WHEEL

From the point of view of design, it is important to have confidence in the accurate predictions of contact pressure for the Michelin Lunar Wheel. Work over the last two chapters has shown that it is not possible for ABAQUS to resolve contact pressure accurately without including a soft tread, even for a simple ring in contact with an analytical rigid ground. Furthermore, for the Michelin Lunar Wheel with or without a compliant layer, computational contact pressure results are very sensitive to the geometrical arrangement and dimensions of the circular cylinders, the manner in which the circular cylinders are attached to the inextensible members and to the properties of the inextensible members. Hence adding a soft compliant layer is required in this study, and will help to distribute load near the cylinder attachment points and at the edges of contact.

In this chapter a description of the two dimensional Michelin Lunar Wheel finite element model created in ABAQUS/ CAE is presented. Because of the argument given above, throughout this thesis a compliant layer thickness of 4mm made of an isotropic material having a stiffness of $1/1000^{th}$ of the circumferential stiffness of Lunar wheel is used.

4.1 Description of the 2D Model Geometry of the First Generation Michelin Lunar Wheel

A model of a two dimensional Michelin Lunar Wheel was developed using beam elements (B21). The total width of the lunar wheel is 203.2 mm which is divided into four lobes. Each lobe has a shear band, consisting of cylinders, glass fiber, and inner and outer inextensible membranes. These shear bands are connected to the hub by a number of thin spokes arranged radially along the circumference of the inner inextensible membrane and the hub. The width of each lobe is 50.8 mm. The dimensions of each part of the Lunar Wheel are provided in Table 4-1. A rectangular shape is assigned for each part in the profile module.

Table 4-1: Dimensions of the First Generation Michelin Lunar Wheel

PART	DIMENSION (mm)	THICKNESS (mm)
Outer Inextensible Membrane	$D_{OE} = 235$	1.5
Inner Inextensible Membrane	$D_{IE} = 205$	1
Glass Cylinder	$D_G = 30$	1
Glass Fiber	$L_{GF} = 30$	0.07
Spokes - Straight	$L_S = 58$	0.4
Spokes - Curved	$R_{SC} = 10$	0.2
Hub	$D_H = 127$	1

Plane strain elements (CPE4R) were used for the compliant layer. The dimensions of the compliant layer are provided in Table 4-2.

Table 4-2: Dimensions of the Compliant Layer

Diameter of the Compliant Layer (mm)	Thickness of the Compliant Layer (mm)
$D_{OC} = 239$ $D_{IC} = 235$	4

In the material property section, the glass composite material properties, which are the same as those presented in Chapter II, are assigned to the shear band and the deformable spokes. For the compliant layer an isotropic material having a stiffness of $1/1000^{th}$ of the circumferential stiffness of Lunar wheel is used as shown in Table 4-3.

Table 4-3: Compliant Layer Material Properties

Young Moduli (E) in MPa	Poisson's Ratio (ν)
40	0.3

The compliant layer is tied to the surface of the outer inextensible membrane by 'surface-based tie constraints'. In the prototype the hub is a very rigid structure and is mounted on the wheel motor. In ABAQUS the hub is modeled as a rigid body where the motion of a hub is governed by the motion of a single node, called the rigid body reference node as shown in Figure 4-1. Therefore, the boundary conditions cannot be applied to the nodes of the hub and should be applied only to the reference node of the wheel.

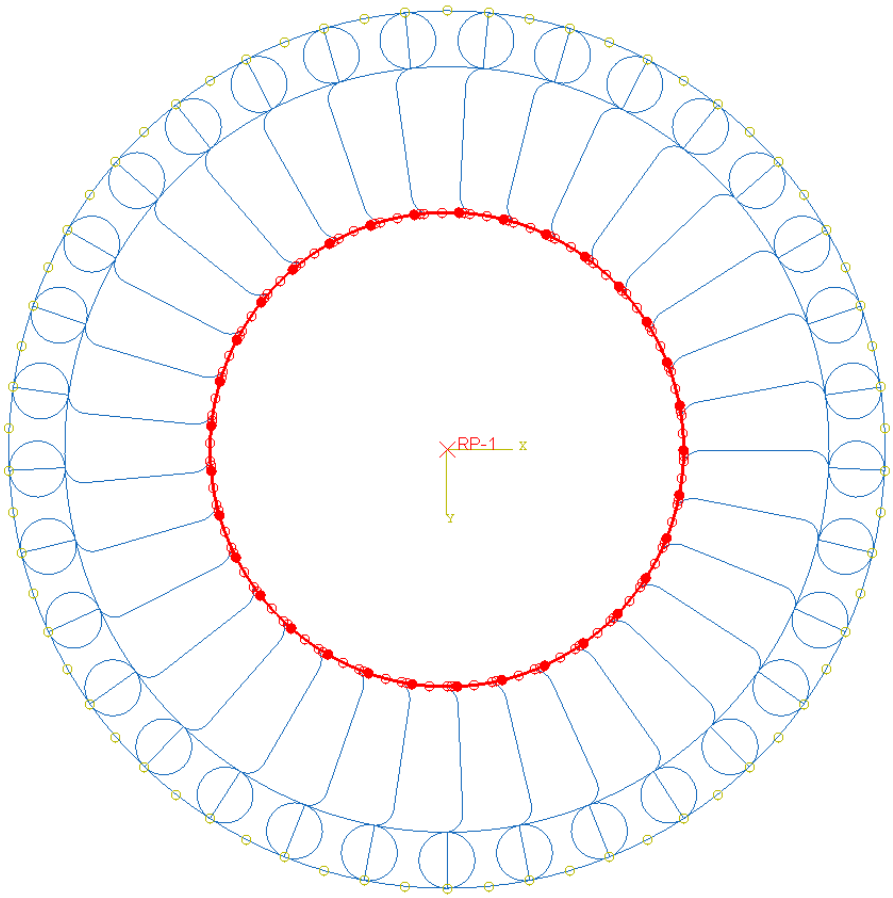

Figure 4-1: The Michelin Lunar model with the rigid body kinematic coupling constraint

For conditions of contact the analytical rigid flat surface is defined as the master surface and the compliant layer is defined as the slave surface. The contact formulation and contact properties remain the same as those presented in Chapter II. Before loading the analytical rigid surface is defined tangent to a single contact point on the compliant layer. After loading, deformation of the shear layer with the compliant layer creates a relatively large contact patch.

The wheel was meshed with 20,856 beam elements and the number of elements on the compliant layer was varied to check convergence of the contact pressure. Since only 1/4th of the width of the NASA Lunar Wheel is considered, only 1/4th of the total load of 625 N was applied perpendicularly at the center of the analytical rigid ground. This loading establishes contact between the wheel and ground. The hub is constrained in all directions and the analytical rigid ground is allowed to move only in the direction of the applied load and. A complete model with the compliant layer, boundary conditions and loading is shown in Figure 4-2.

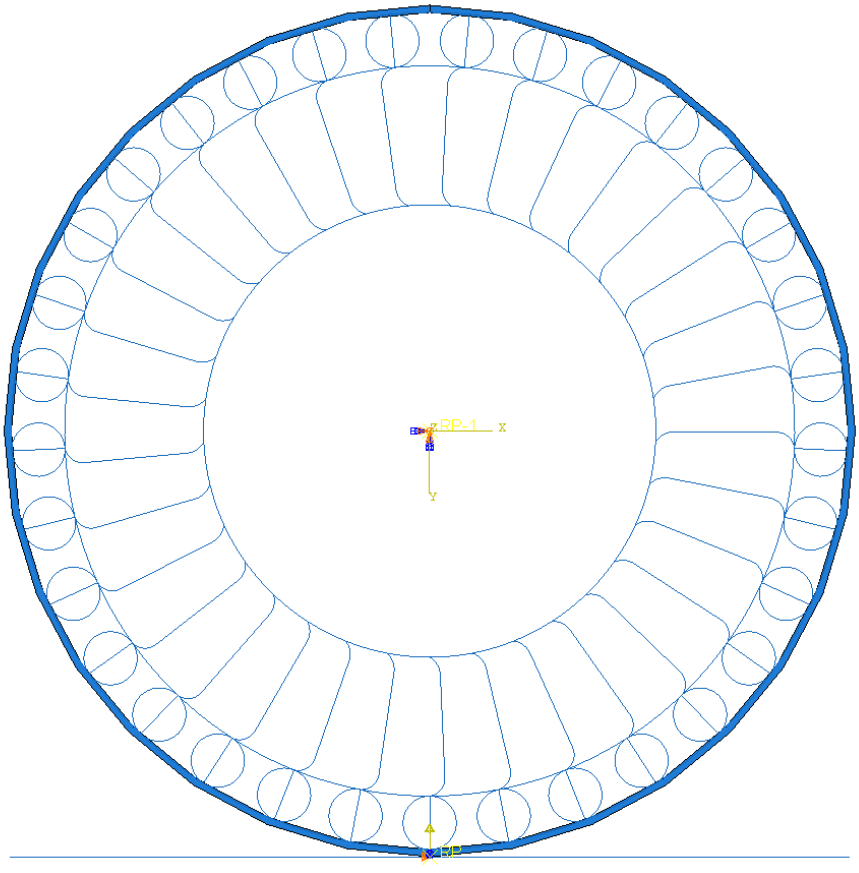

Figure 4-2: The Michelin Lunar Wheel model with the compliant layer and the loading and boundary conditions

A three dimensional view of the NASA Lunar wheel is presented in Figure 4-3.

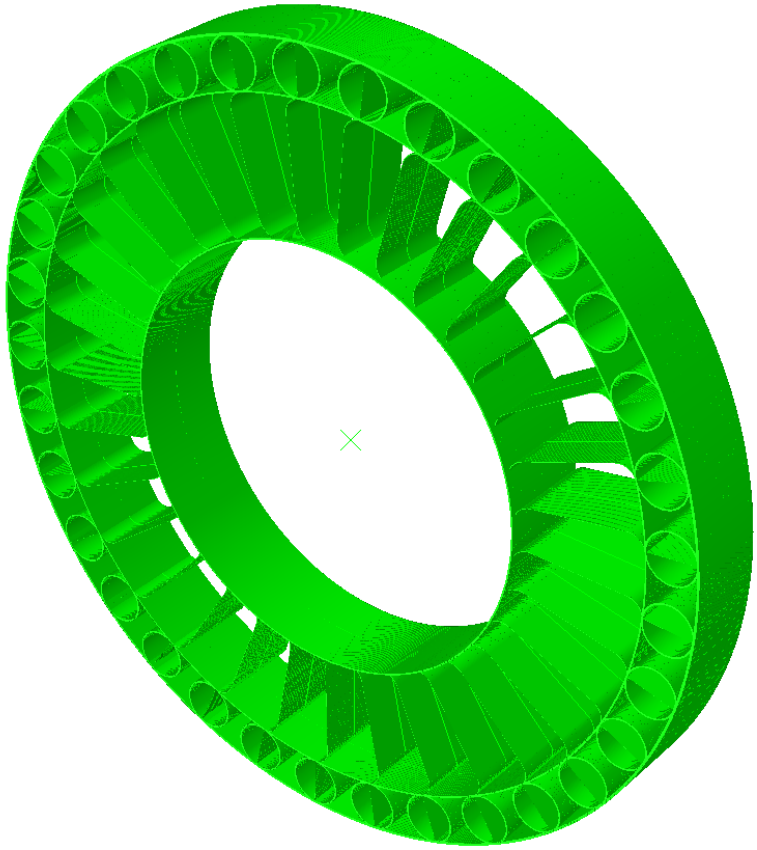

Figure 4-3: The Michelin Lunar model (3D visulization)

4.2 Results

When the wheel is loaded the deformed configuration of the shear band with compliant layer has effectively three cylinders in contact region as shown in Figure 4-4.

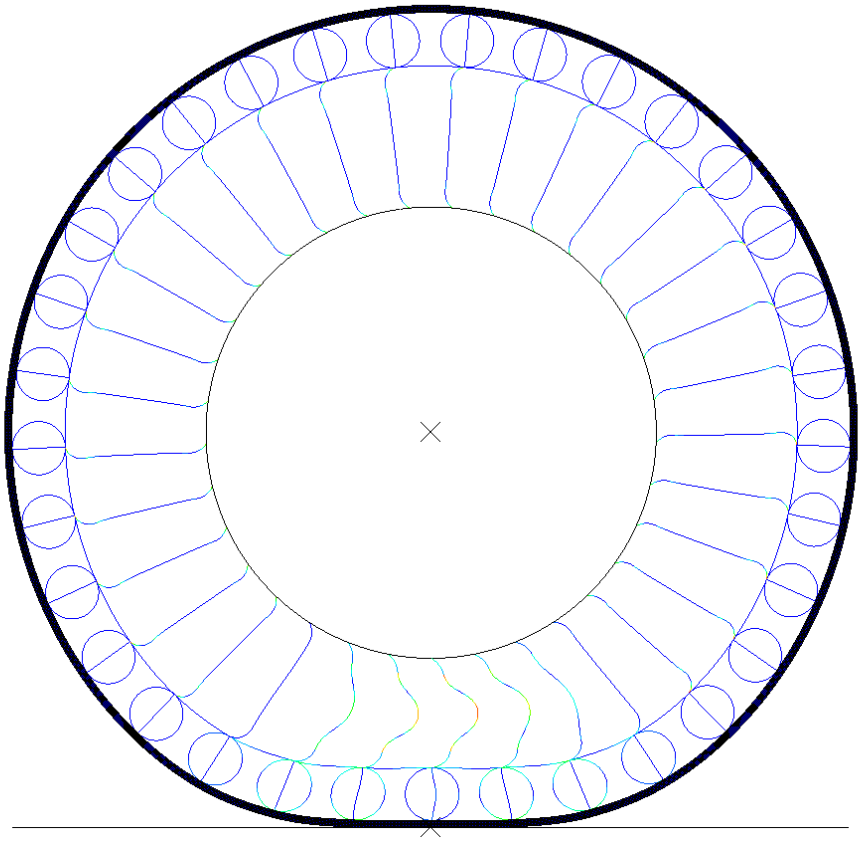

Figure 4-4: Deformed configuation of the Michelin Lunar model for the baseline case of 625 N

The number of elements within the compliant layer was varied and convergence of the contact pressure profile was achieved as shown in Figure 4-5. From this contact pressure plot it is clearly seen that the end cylinders carry more load then the center cylinder. The converged force displacement plot is shown in Figure 4-6. The pressure varies from 0.14 to 0.40 MPa which is equal to 1.4 to 4 in the bar scale.

Table 4-3: Convergence study for the First Generation Michelin Lunar model with a compliant layer

No of Elements on the Michelin Lunar Wheel Tire model = 20,856			
No of Elements on the Compliant Layer (Aspect Ratio=1)	Integral of the Pressure [Reaction Force] (N)	Contact Length (mm)	Contact Pressure Peak (N)
9250	624.9972	70.3231	20.6793
37000	625.0010	70.727	20.7428
148000	625.0014	70.5257	20.7552

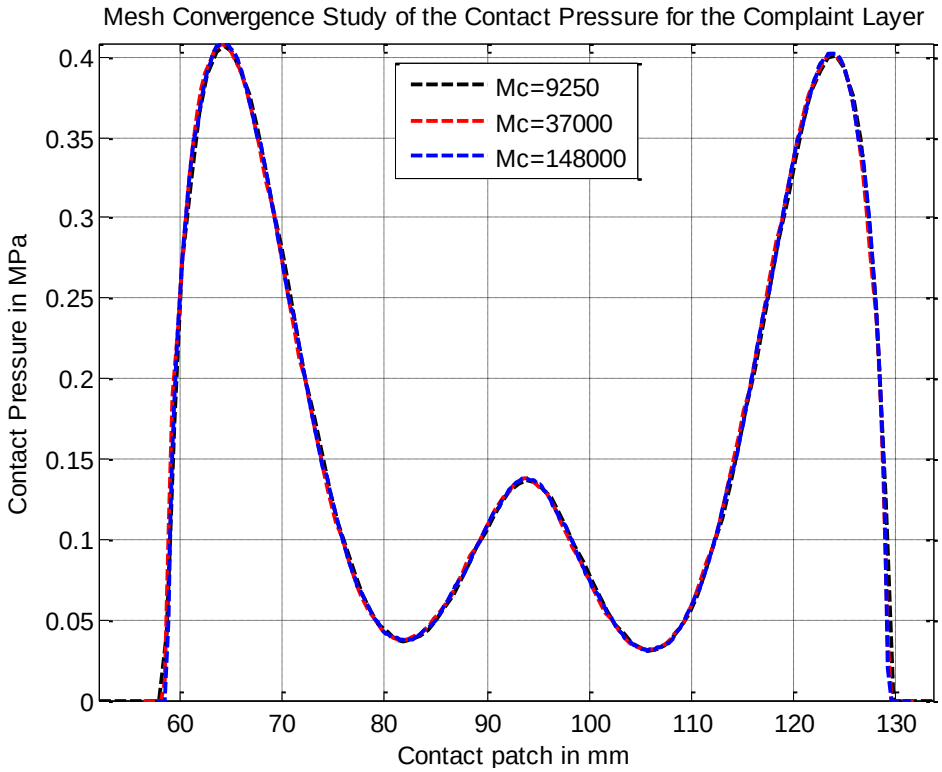

Figure 4-5: Contact Pressure profile of the Third Generation Michelin Lunar model for 625 N with a compliant layer having three cylidners in contact (MPa)

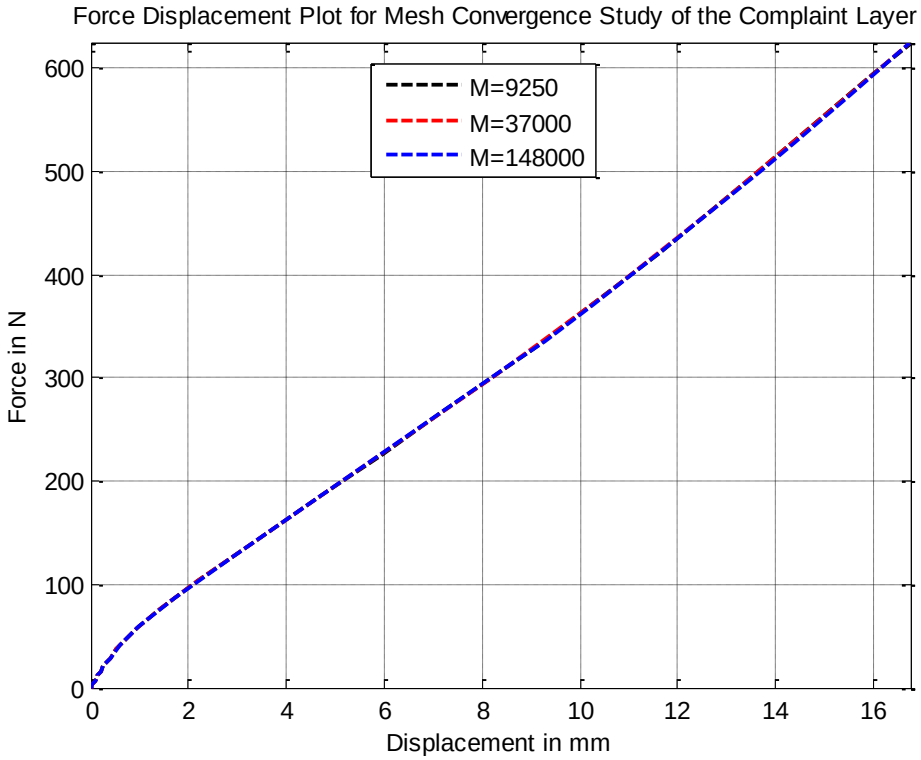

Figure 4-6: Force vs. Displacement plot of the First Generation Michelin Lunar model with a compliant layer

CHAPTER FIVE

DESIGN PARAMETRIC STUDY ON THE FIRST GENERATION MICHELIN LUNAR WHEEL

With a reliable and physically realistic computational model identified for predicting the contact pressure accurately, the Michelin Lunar Wheel model with a 4 mm thick compliant layer will be used as the base model on which sensitivity analysis is preformed to understand how key design variables affect the pressure distribution. The sensitivity/design parameters include:

- Study of the connections between the circular cylinders and the inextensible membranes.
- Effect of thickness of cylinders.
- Effect of volume fraction of the Glass Composite.
- Effect of cylinder orientation.
- Effect of non-uniform ground.

5.1 Study of Connections between the Circular Cylinders and Inextensible Membranes

The shear layer of the first generation Michelin Lunar wheel has cylinders which are bonded to the inner and the outer inextensible membrane by an adhesive. Addition of the adhesive between the cylinders and the membranes increases the stiffness of the connection and has an effect on the development of spikes in the contact pressure. The first generation wheel also has the glass fiber that affects the

stiffenss of this connection. In the case of the third generation wheel, the cylinders are actually bolted to the membranes. In either case, the contact pressure is affected by the manner in which the cylinders are attached to the membranes and a precise modeling of this connection is required for an accurate prediction. In this study, which applies to the first generation wheel, the following two extremes of kinematic constraints are considered at the connection/attachment points:

- Fixed Case: The adhesive creates a fixed support at the attachment point between the cylinders and the membranes allowing no rotation or motion in any direction.
- Pinned Case: The cylinders are allowed to rotate with respect to the membranes at the attachment points. Contact is defined between the cylinders and the adhesive.

In order to make the finite element model more realistic, the epoxy adhesive was modeled using plane strain CPE4R elements and assembled between all the cylinders and inextensible membranes at the attachment points for both the fixed and pinned cases. The cylinder diameter and glass fiber length was reduced from 30 mm to 29.75 mm to provide space for the adhesive. The thickness of the epoxy used on either side is 0.125 mm and the width of the surface on which the epoxy is applied is 8 mm. Isotropic material properties are used for epoxy, which were provided by MICHELIN as given in Table 5-1.

Table 5-1: Epoxy Material Properties

Young Moduli (E) in MPa	Poisson's Ratio (ν)
3500	0.358

A fine quad dominated mesh is used for the epoxy and the total number of elements is 1980. The Michelin Lunar Wheel was meshed with 20,823 beam elements and the compliant layer was meshed with 37,000 plane strain elements. The boundary conditions and the loading remain the same as those of Chapter IV.

5.1.1 Fixed Case:

The outer surfaces of epoxy were tied to the surfaces of the inextensible membranes (inner and outer) by 'surface based tie constraints' at both ends. The curved surfaces of the epoxy were tied to the surface of the cylinders using a similar approach. The tie definitions are shown in Figure 5-1. A portion of the revised model including a thin layer of epoxy filler is presented in Figure 5-2.

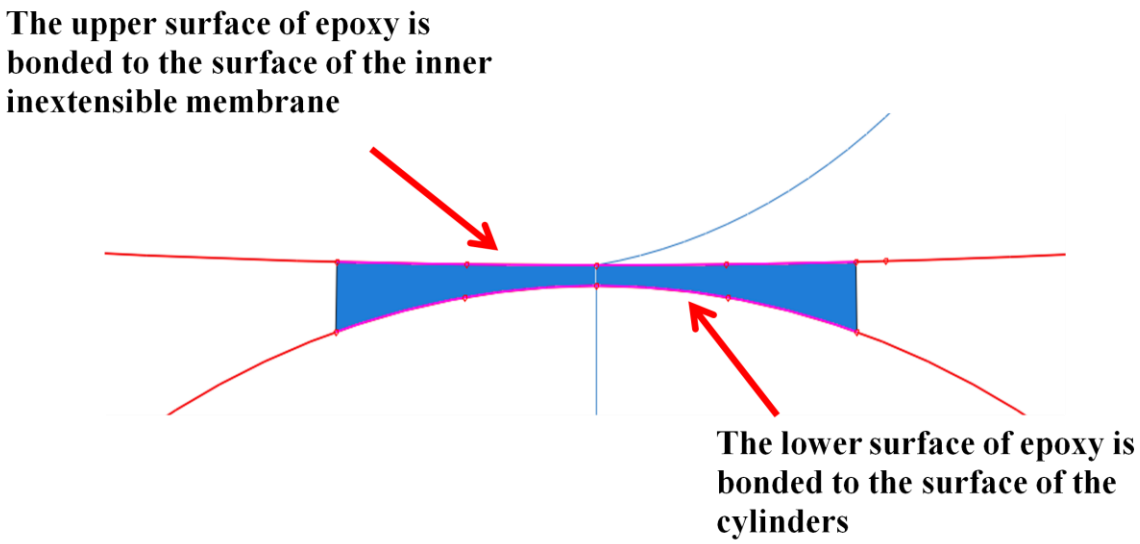

Figure 5-1: Fixed Case definition

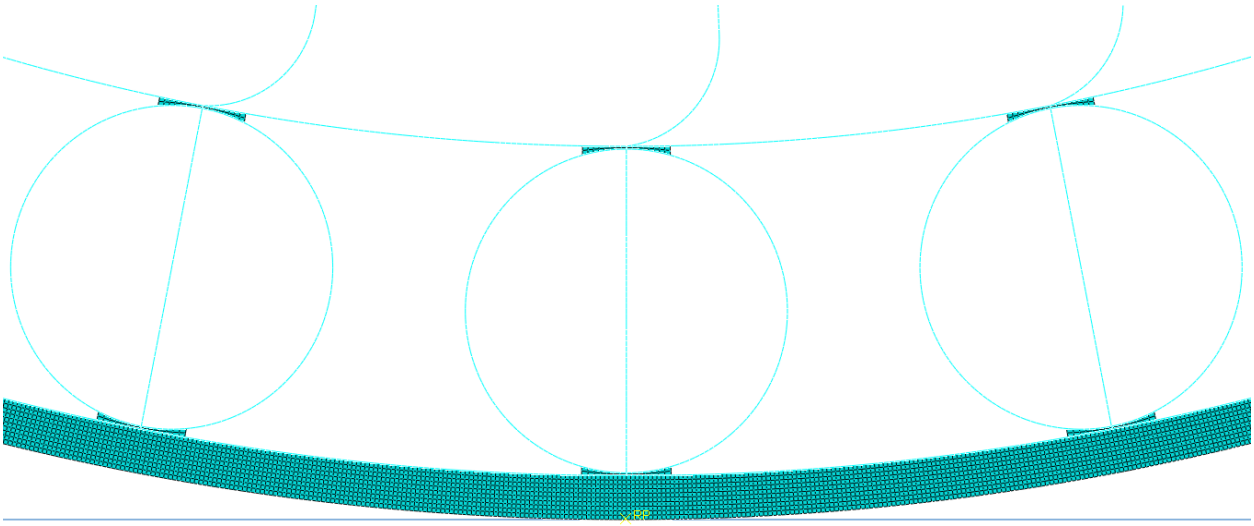

Figure 5-2: Filler material Epoxy added between the cylinders and the inextensible membranes

5.1.1.1 Results for Fixed Case

As seen from the plot in Figure 5-3, the pressure drops down even further and is approaching the type of result to be expected based on the experimental results in Chapter I. Adding the adhesive helps in making the pressure more uniform in the contact patch. A comparison of the force displacement response is shown in Figure 5-4.

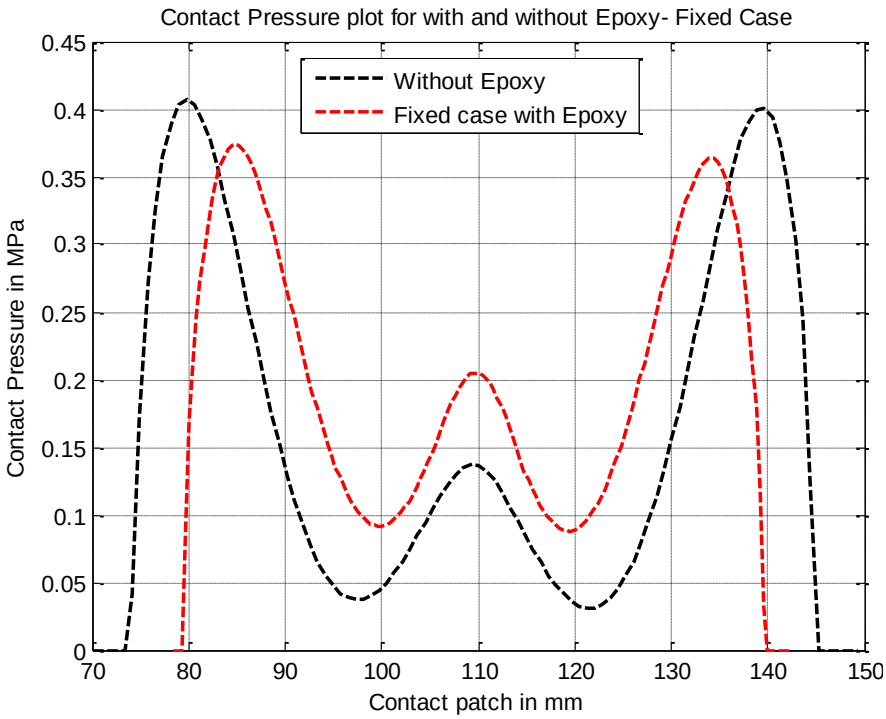

Figure 5-3: Contact Pressure plot for the Lunar Wheel with and without Epoxy (Fixed Case)

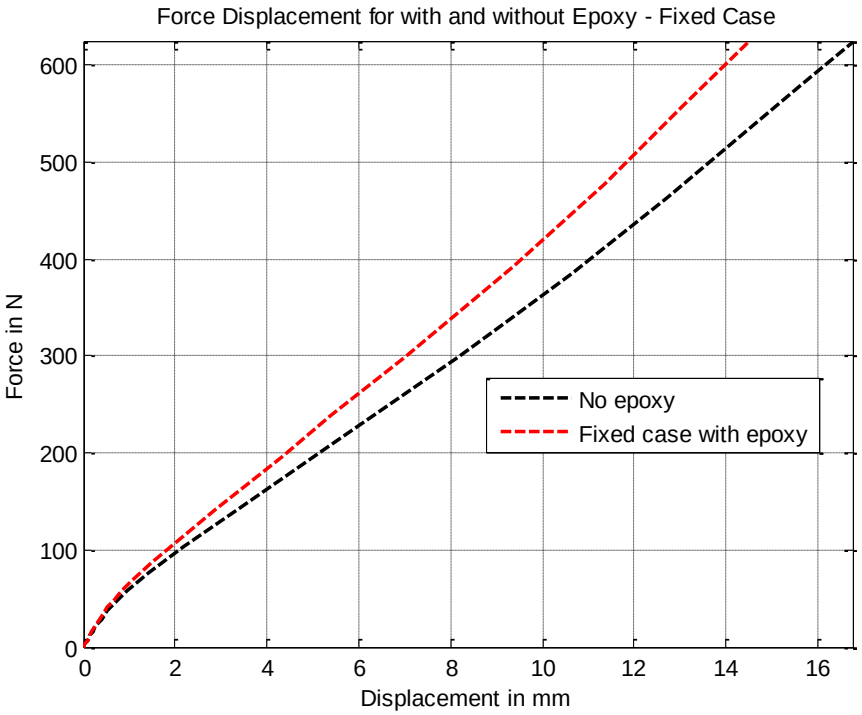

Figure 5-4: Force Displacement plot for the Lunar Wheel with and without Epoxy (Fixed Case)

5.1.2 Pinned Case

The outer surfaces of epoxy were tied to the surfaces of the inextensible membranes (inner and outer) by 'surface based tie constraints' at both ends. The curved surfaces of epoxy were pinned to the surface of the cylinders at the attachment point only using 'surface based coupling constraints.' This is equivalent to assuming that the epoxy has debonded from the cylinder and serves only as filler that will affect contact. A frictionless contact with direct hard over pressure enforcement method defined in Chapter II is used here. The surface of the cylinders is made the master surface and the surface of epoxy is made the slave surface, since the cylinders are stiffer. The pinning conditions are shown in Figure 5-5.

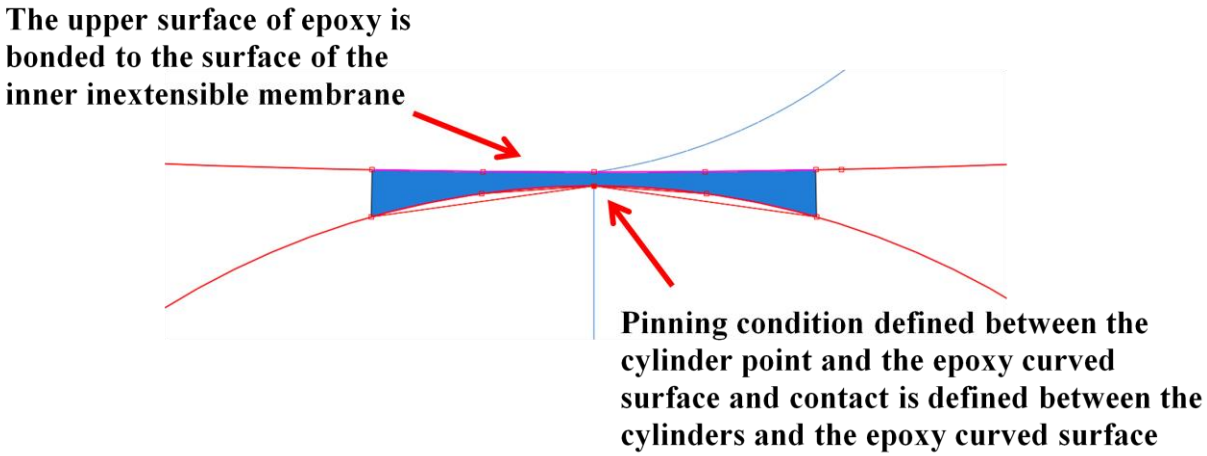

Figure 5-5: Pinning Case definition

5.1.2.1 Results for Pinned Case

Compared to the fixed case, as shown in Figure 5.6, the pressure is shifted from the outer cylinders to the center cylinder. The contact patch length for this case is about 4

mm more than the fixed case. Since the pressure distribution profile has more pronounced upper and lower bounds compared to the fixed case which is more uniform with respect to the experimental results, only the fixed case with epoxy is used as the baseline case in further analysis in this thesis. The force displacement plot for the pinned case is shown in Figure 5-7. The fixed case has a displacement of 14.87 mm and the pinned case has a displacement of 14.91 mm, which shows that for a small degree of change in connections the contact pressure profile is affected drastically.

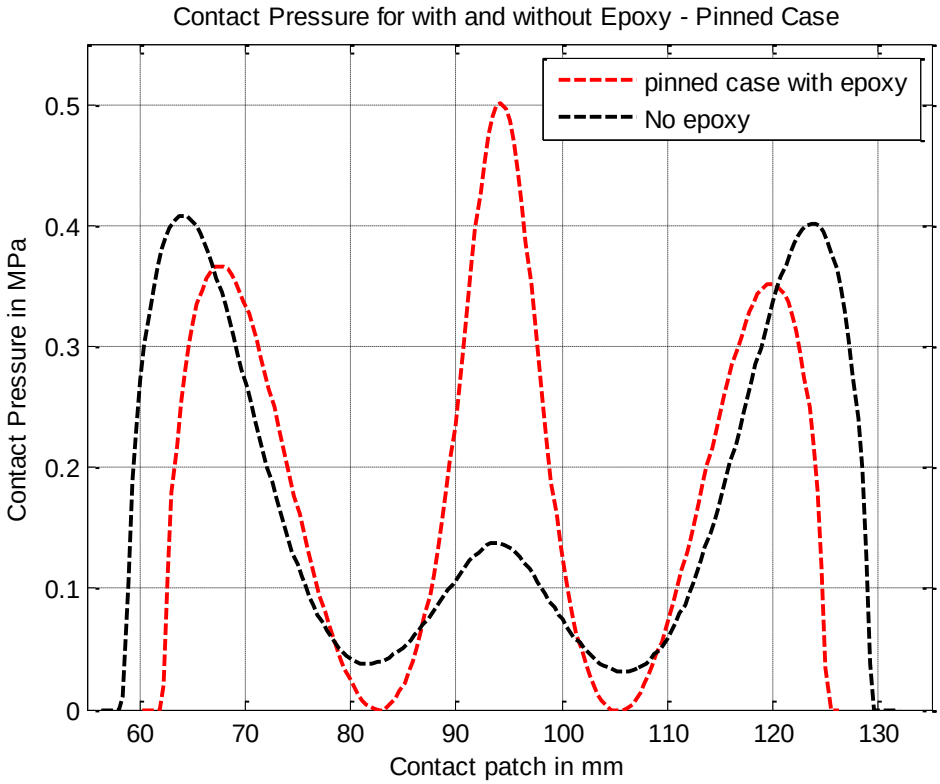

Figure 5-6: Contact Pressure plot for the Lunar Wheel with and without Epoxy (Pinned Case)

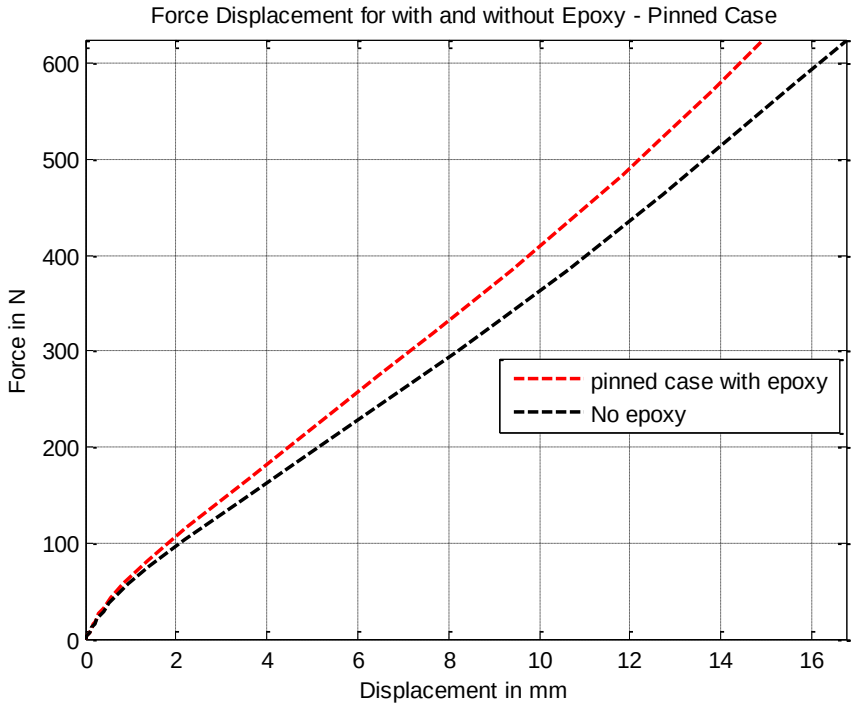

Figure 5-7: Force Displacement plot for the Lunar Wheel with and without Epoxy (Pinned Case)

5.2 Effect of Thickness of Cylinders

For the fixed case with epoxy, the cylinder wall thickness was reduced to understand how the shear stiffness affects the pressure distribution. For a given load, the lateral displacement is expected to be a strong function of the thickness of the cylinders. The thickness was reduced in the four increments shown in Table 5-2.

Table 5-2: Thickness Reduction of Cylinders

Thickness of the Cylinders	Number of cylinders in the Contact Patch	Contact Length (mm)
1	3	60.76
0.75	3	83.47
0.5	5	138.54
0.25	5	162.91

From the contact length results presented in Table 5-2 and the contact pressure distribution shown in Figure 5-8, it is clear that reducing the thickness of the cylinders helps in reducing the shear stiffness, GA, of the cylinders which increases the contact patch length for the same load. As expected the force-displacement curves presented in Figure 5-9 for the four cylinder thicknesses cases show a significant decrease in vertical stiffness as the wall thickness of the cylinders is reduced.

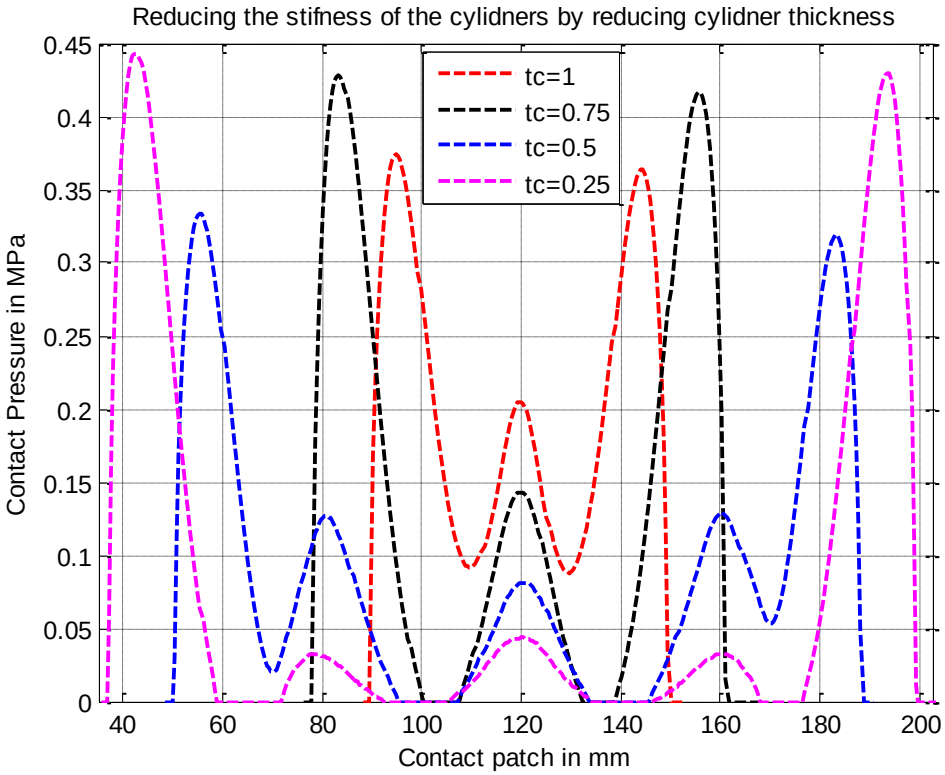

Figure 5-8: Contact Pressure plot for the Michelin Lunar Wheel with epoxy and reducing the thickness of the cylinders

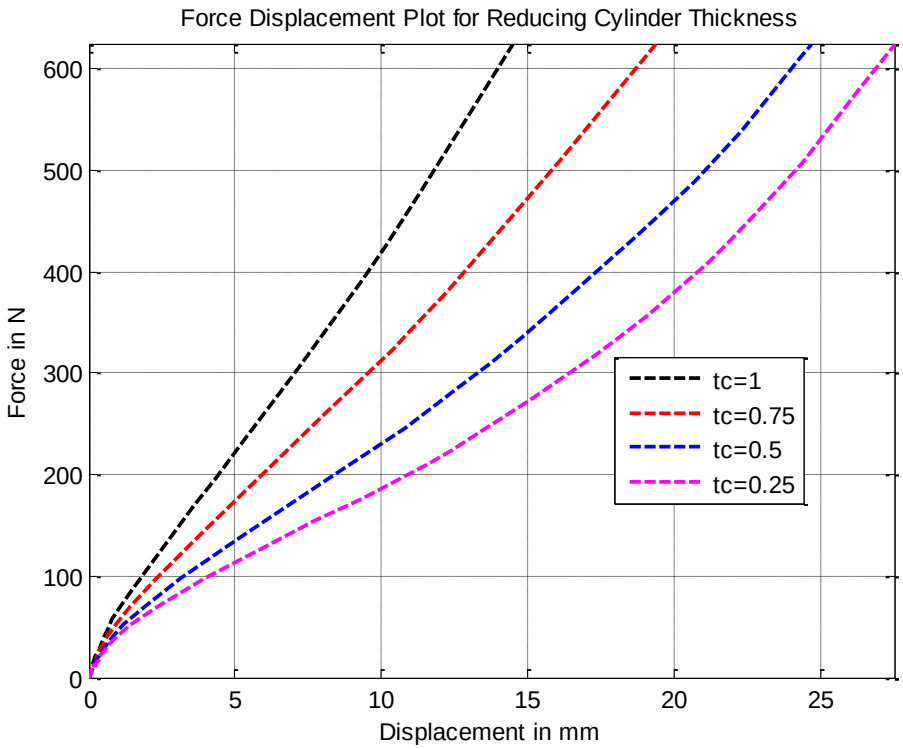

Figure 5-9: Force Displacement plot for the Lunar Wheel with epoxy and reducing the thickness of the cylinders

5.3 Reducing the Volume Fraction of the Glass Composite

The volume fraction of the glass fibers in the composite (M_f) is 0.7 and the remaining 0.3 percent is resin (M_m). From Chapter II it is known that when the shear modulus and Young's modulus are very high in the circumferential direction, bending deformation dominates over shear deformation resulting in an Euler-Bernoulli type pressure solution. Therefore, if the volume fraction of the Glass Composite is reduced, the values of the Young's modulus and shear modulus are lowered which changes the pressure distribution. The data presented in Table 5-3 show the values of the Young's modulus and the shear modulus when the volume fraction is reduced.

Table 5-3: Volume fraction reduction of the Glass Composite

M_f/M_m	E_1	E_2	E_3	ν_{12}	ν_{13}	ν_{23}	G_{12}	G_{13}	G_{23}
0.7	39969	6813	6813	0.29	0.05	0.48	2537	2537	3500
0.6	32166	5655	5655	0.3	0.06	0.48	2108	2108	3500
0.5	25559	4958	4958	0.31	0.07	0.48	1844	1844	3500
0.4	19891	4479	4479	0.32	0.08	0.48	1665	1665	3500
0.3	14997	4132	4132	0.33	0.09	0.48	1536	1536	3500

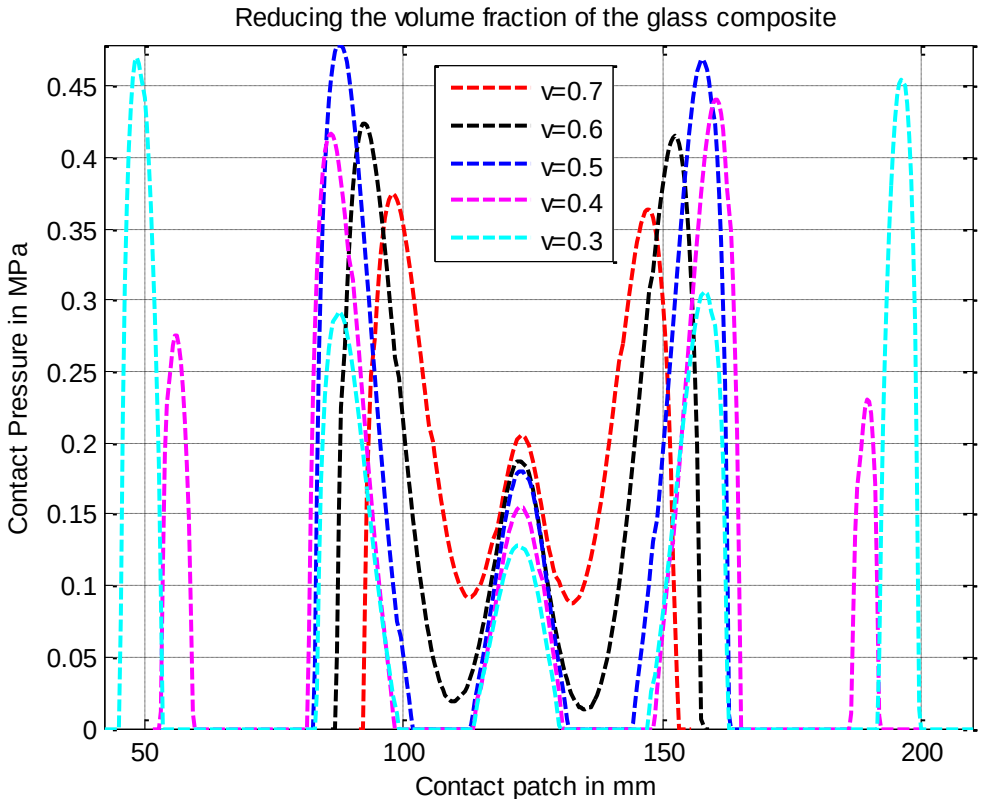

Figure 5-10: Contact Pressure plot for the Michelin Lunar Wheel reducing the volume fraction of Glass Composite

It is seen from Figure 5-10 that reducing the volume fraction of the glass composite redistributes the pressure by increasing the contact patch. But this approach of modifying the pressure profile is not as effective as reducing the wall thickness of the

cylinders, since the contact pressure is more uniform with smaller gaps between peaks in contact pressure than for the former.

5.4 Effect of Cylinder Orientation

The angular distance between two cylinders is 10.91 degrees. So far all results have been obtained for the symmetric orientation where one cylinder is at the bottom of the wheel. In this study, the other case of symmetry is considered where two cylinders are located at the bottom of the wheel as shown in Figure 5-11. This new orientation will affect both the pressure distribution and the vertical stiffness. Since the vertical stiffness is affected, the wheel will experience vibration and possibly fatigue as the wheel rolls.

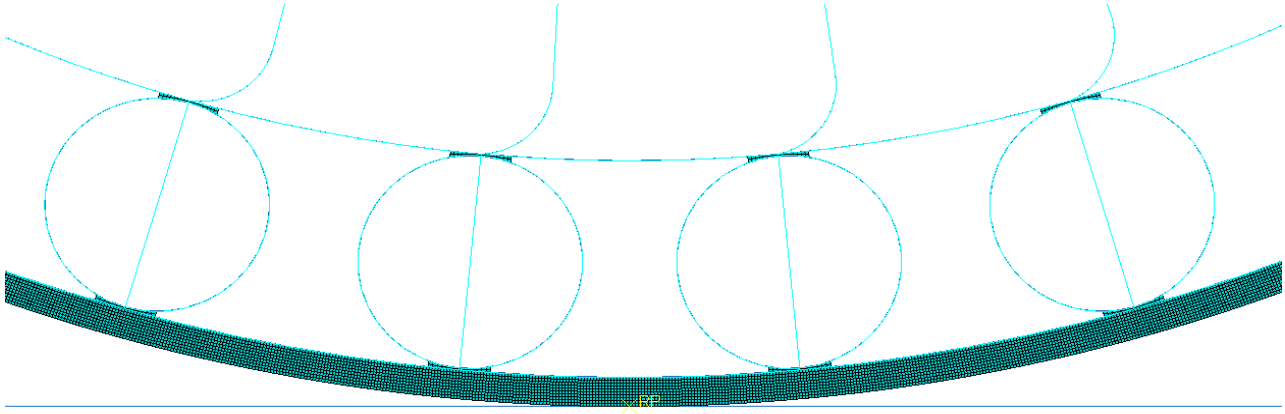

Figure 5-11: Section view of the rotated configuration

Two cases are studied here to observe the vibration/fatigue effect, which are summarized in Table 5-4.

1. 625 N Load, h = 4mm (compliant layer) with epoxy and thickness of cylinders (t_c) = 1 mm

2. 625 N Load, h=4mm (compliant layer) with epoxy and thickness of cylinders (t_c) = 0.5 mm

Table 5-4: Displacement for rotated and unrotated configuration for the two cases of cylinder thickness

Thickness of cylinders in mm	Rotated Configuration Displacement in mm	Unrotated Configuration Displacement in mm
1	14.8692	14.4812
0.5	24.2159	24.6473

From the Figure 5-12 and Figure 5-14 it is seen that when the rotated configuration is loaded, there are two cylinders present in the contact patch for t_c = 1mm and four cylinders in contact for t_c = 0.5mm compared to unrotated case which has three and five cylinders in the contact patch, respectively. The force-displacement response for these cases is presented in Figure 5-13 and Figure 5-15, respectively. Figure 5-13 and Figure 5-15 show the pressure peaks at various intervals of imposed displacement. For the case where the thickness of the cylinders is 1 mm it is seen that the rotated configuration has a higher displacement than the unrotated configuration, and when the thickness of the cylinders is changed to 0.5 mm the later has a higher displacement than the former one clearly signifying that the vertical stiffness of the wheel is not constant and changes as the wheel rolls.

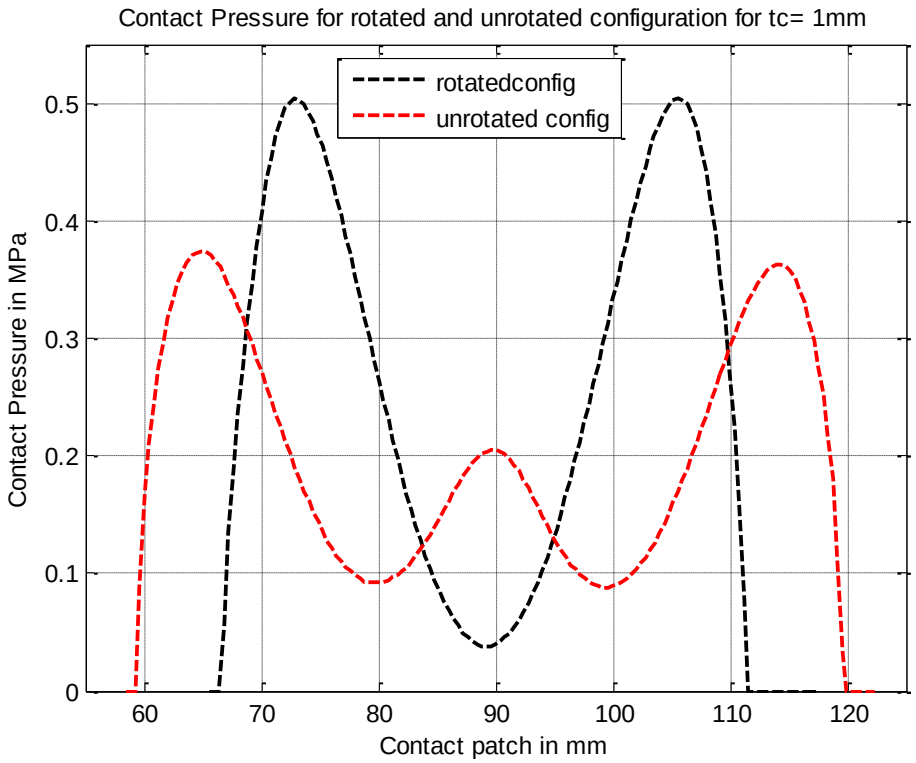

Figure 5-12: Contact Pressure plot for the Lunar Wheel for rotated and unrotated configuration when cylinder thickness t_c=1 mm

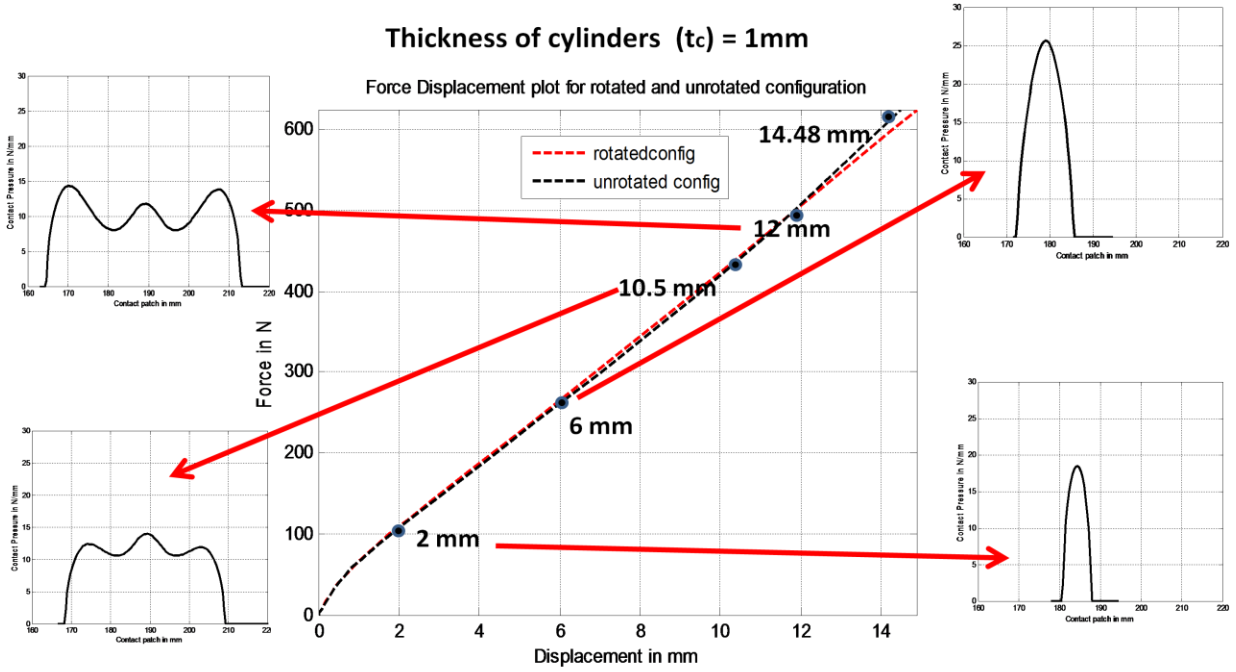

Figure 5-13: Force Displacement plot for the Lunar Wheel for rotated and unrotated configuration when cylinder thickness t_c=1 mm

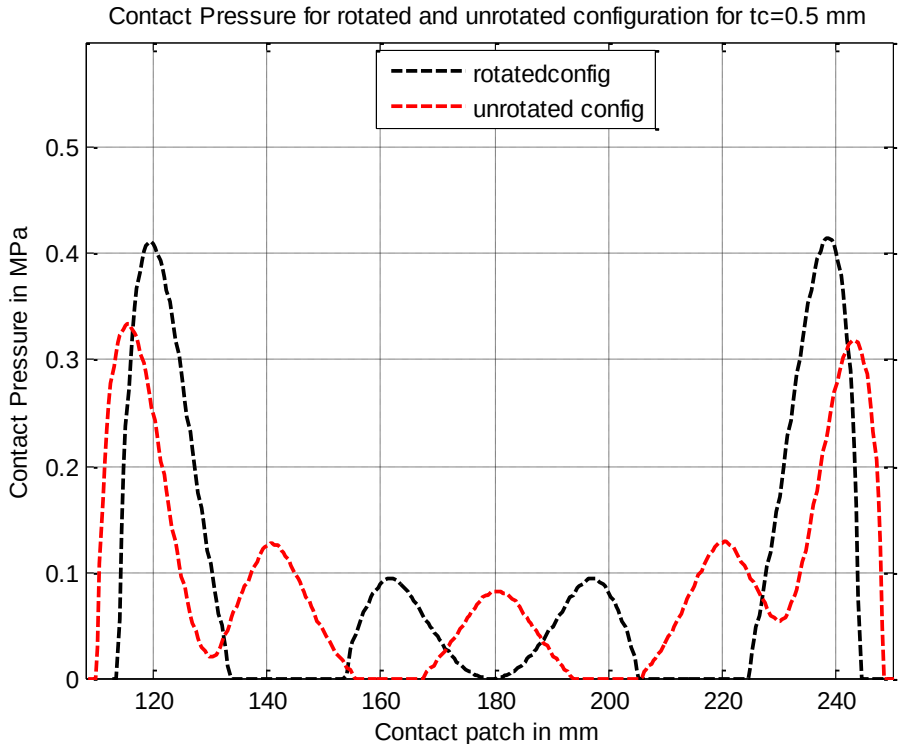

Figure 5-14: Contact Pressure plot for the Lunar Wheel for rotated and unrotated configuration when cylinder thickness t_c= 0.5 mm

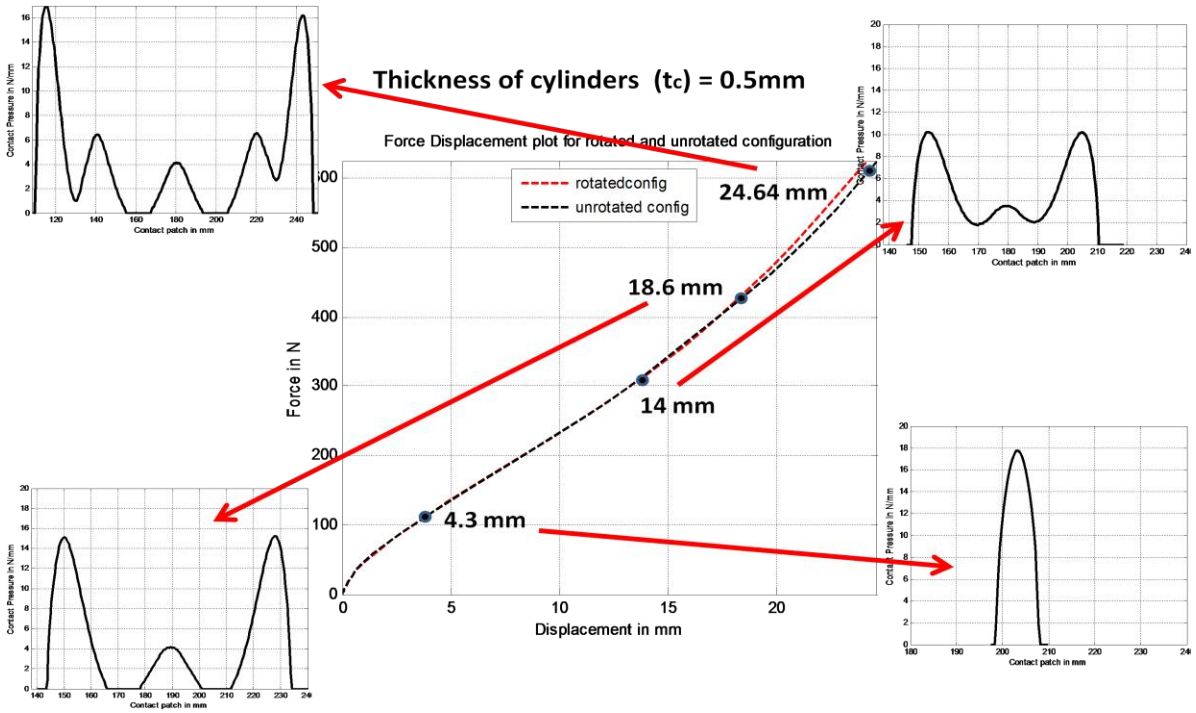

Figure 5-15: Force Displacement plot for the Lunar Wheel for rotated and unrotated configuration when cylinder thickness t_c= 0.5 mm

5.5 Effect of Non Uniform Ground

One way to try to make the contact pressure more uniform is to add a non-uniformly thick layer of material to the outside of the outer inextensible membrane. This can be achieved by adding a non-uniform compliant layer or by adding a "filler" material between the outer inextensible membrane and the uniformly thick compliant layer. The latter case is preferred in this study since it will give an indication of how much thickness is required to convert the non-uniform pressure distributions into uniform pressures. However, this case is complicated by the finite element modeling choices available and the effect this added material has on the bending stiffness of the membrane. Therefore, a preliminary investigation of this idea is achieved by modifying the flat rigid ground surface into a slightly curved surface.

In order to determine the ground shape that will produce a uniform pressure with the existing Michelin Lunar Wheel for baseline case with epoxy presented in Figure 5-3 (red curve) the wheel is loaded with the average pressure over the same contact length as for the baseline case. The displacement in the loaded region is then compared to the contact boundary condition,

$$v(x) = \delta_0 - R + \sqrt{R^2 - x^2} \quad . \tag{5-1}$$

This boundary condition is the required displacement for the outer surface of the tread at radius R, if the flat ground is raised by an amount δ_0. The variable, x, is measured within the contact region with $x = 0$ at the center of the wheel. The difference between this displacement and that from ABAQUS corresponds in displacement terms,

how far "off" the contact pressure is from being uniform. The ABAQUS results for this displacement comparison are presented in Figure 5-16, while the difference which corresponds to the required ground shape is presented in Figure 5-17.

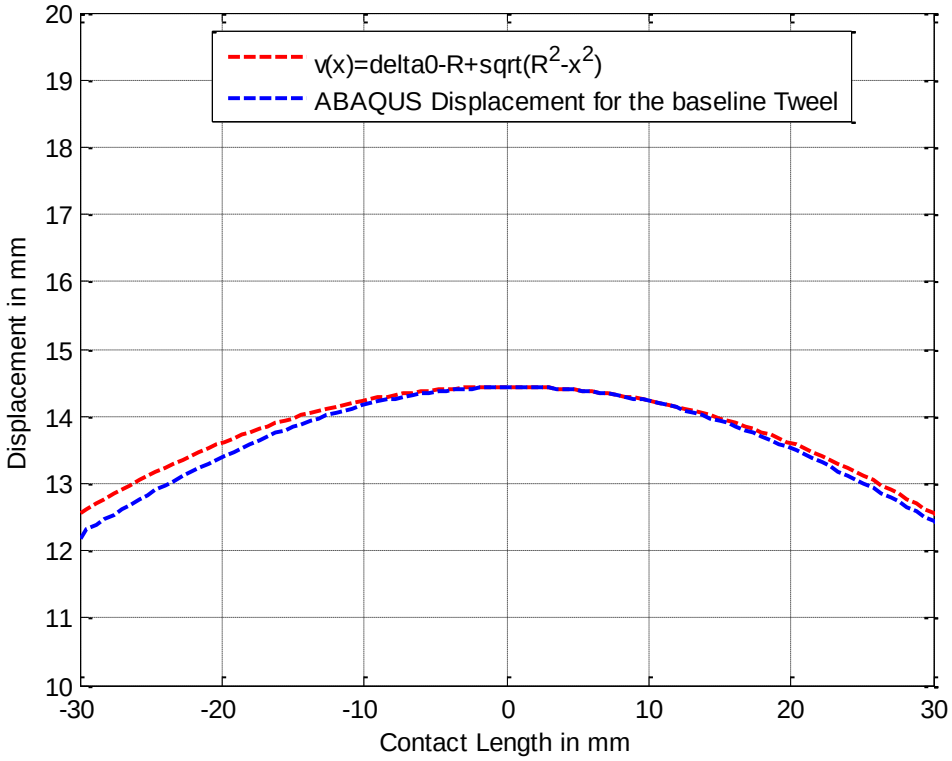

Figure 5-16. Displacement of the baseline wheel within the assumed contact area for a uniform pressure compared to the displacement boundary condition presented in Equation 5-1

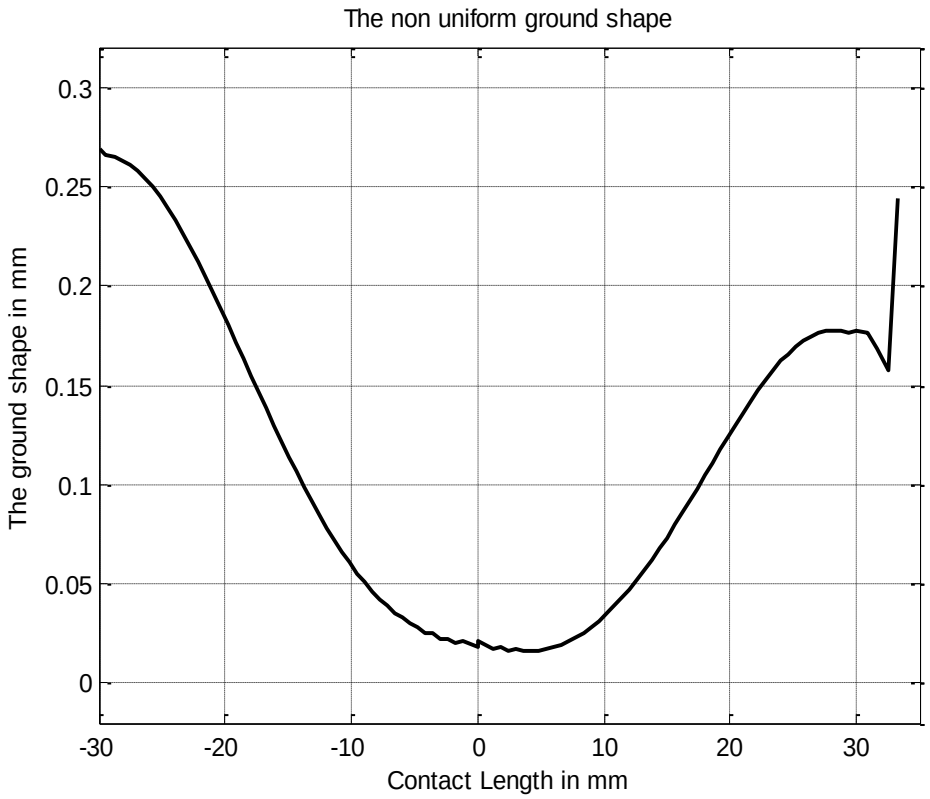

Figure 5-17. Difference in the displacements from Figure 5-16, which indicates the ground shape that should result in a uniform pressure

In Figure 5-18 the pressure that results from loading the baseline Tweel on a ground shape slightly perturbed from flat according to Figure 5-17 is presented. It is observed that this pressure is nearly uniform, as expected.

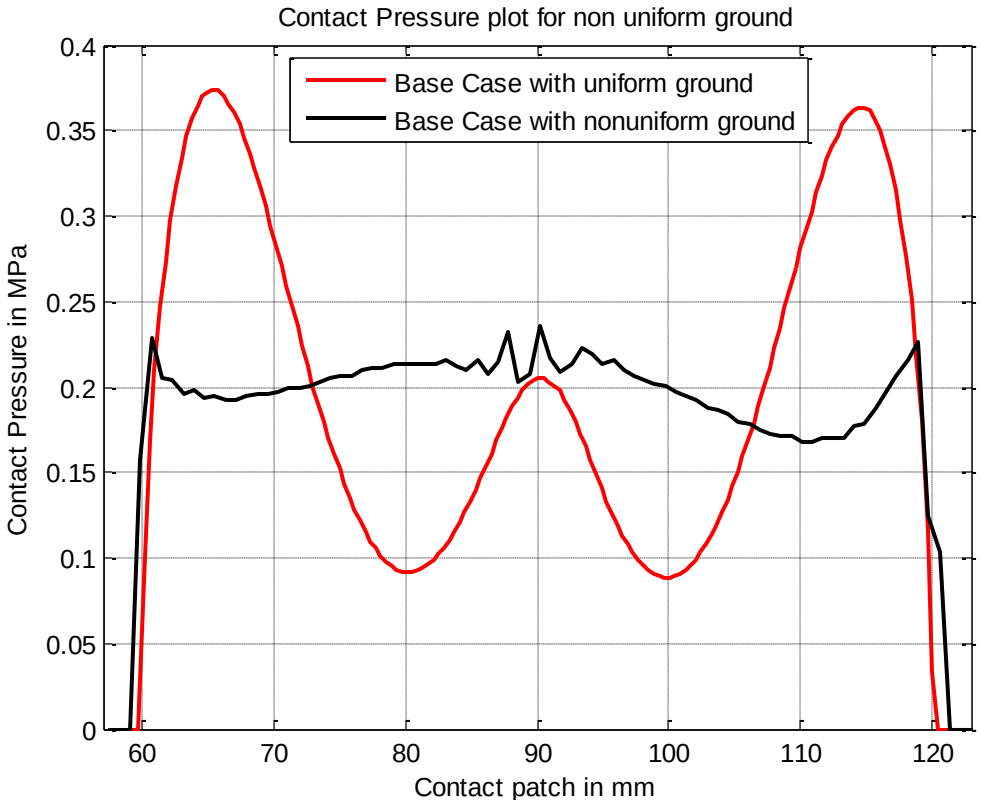

Figure 5-18. Contact pressure for the baseline case on a flat surface and for a surface defined by the profile presented in Figure 5-17

The important point is the slight difference in ground shape that converts the non-uniform pressure into a uniform pressure. The amplitude of this ground profile is approximately 2% of the total displacement. Therefore, in order to have ABAQUS predict (correct) experimental values of pressure, it is necessary to model the structure and connections accurately enough to capture this level of displacement.

CHAPTER SIX

THREE DIMESIONAL FINITE MODEL OF THE THIRD GENERATION MICHELIN LUNAR WHEEL

A three-dimensional finite element model of the third generation Michelin Lunar Wheel is considered to take into account the modeling changes compared to the first generation. The third generation wheel has a larger diameter of approximately 28” and has fifty-six double layered cylinders arranged around the circumference of the shear band. In this case the cylinders are more closely packed in the shear band compared to the first generation wheel. Hence, the contact pressure will be affected by the larger wheel diameter, the cylinder spacing, and the double layered cylinder design compared to the first generation.

In this chapter, the third generation Lunar Wheel model is pressed against a rigid plane to observe if five cylinders are present in the contact patch and to see how the contact pressure profile compares with the experimental result.

6.1 Description of 3D Model Geometry of the Third Generation Michelin Lunar Wheel

A three dimensional third generation Michelin Lunar wheel which was developed by Marisa Orr [20] is being used as the base model to which the 4 mm compliant layer is added and MICHLEIN provided orthotropic material properties are used for the Wheel. The model was created using conventional shell elements (S4R). The wireframe model is extruded to create half of the wheel which consists of two lobes, the width being 106 mm.

The offset distance between the two cylinders within the shear band is 3.5 mm. A section view of the oval shaped concentric cylinders is shown in Figure 6-1. The dimensions of each part of the Lunar Wheel are provided in Table 6-1.

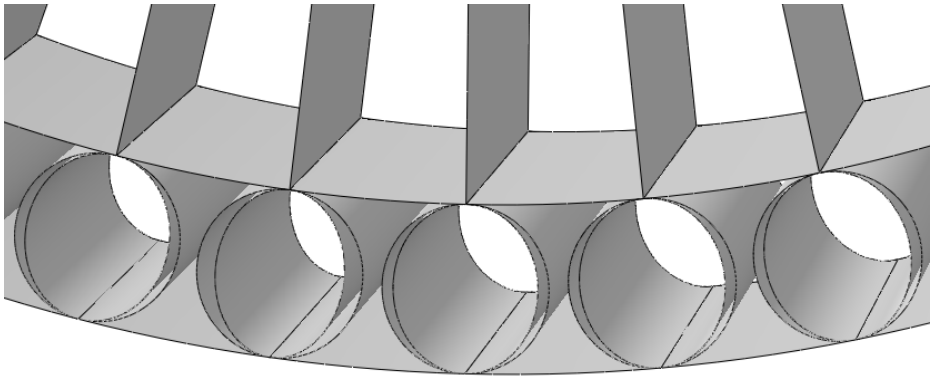

Figure 6-1: Section view of the oval shaped cylinders in the shear band

Table 6-1: Dimensions of the Third Generation Michelin Lunar Wheel

PART	DIMENSION (mm)	THICKNESS (mm)
Outer Inextensible Membrane	$D_{OE} = 703$	1.5
Inner Inextensible Membrane	$D_{IE} = 635.8$	1.5
Inner Glass Cylinder	$D_{IG} = 16.8$	0.7
Outer Glass Cylinder	$D_{OG} = 16.8$	0.7
Spokes - Straight	$L_S = 78.7$	0.1
Springboard (Curved spokes to Hub connector)	$R_{SB} = 12$	1.5
Hub	$D_H = 478.4$	1

A compliant layer of 4 mm is bonded to the outer surface of the outer inextensible membrane using ‘surface based tie constraints’ in ABAQUS. The compliant layer is meshed with 3D stress solid elements (C3D8R). The analytical rigid ground is a

wireframe model and extruded to 106 mm. The other features such as the material properties used for the wheel and compliant layer, interaction surfaces, contact formulation, contact properties and boundary conditions remain the same as those presented in Chapter IV. The hub is a rigid body and constrained to the motion of a center reference node of the wheel using 'kinematic coupling constraints'. The full 3D shell model of the third generation Lunar Wheel with two lobes is shown in Figure 6-2.

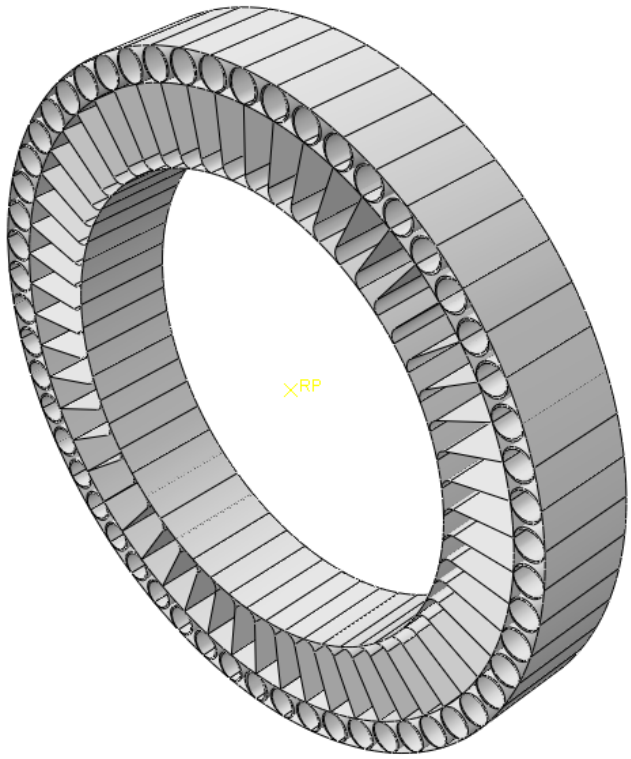

Figure 6-2: 3D shell model of the third generation Michelin Lunar Wheel

The wheel is meshed with 49,896 reduced integration shell elements and the compliant layer was meshed with 86,000 reduced integration solid elements. Since only half of the model is considered here due to symmetry, a load of 1250 N was applied at the

reference point on the ground and pushed to establish contact. A complete 3D model with the compliant layer, boundary and loading conditions is shown in Figure 6-3.

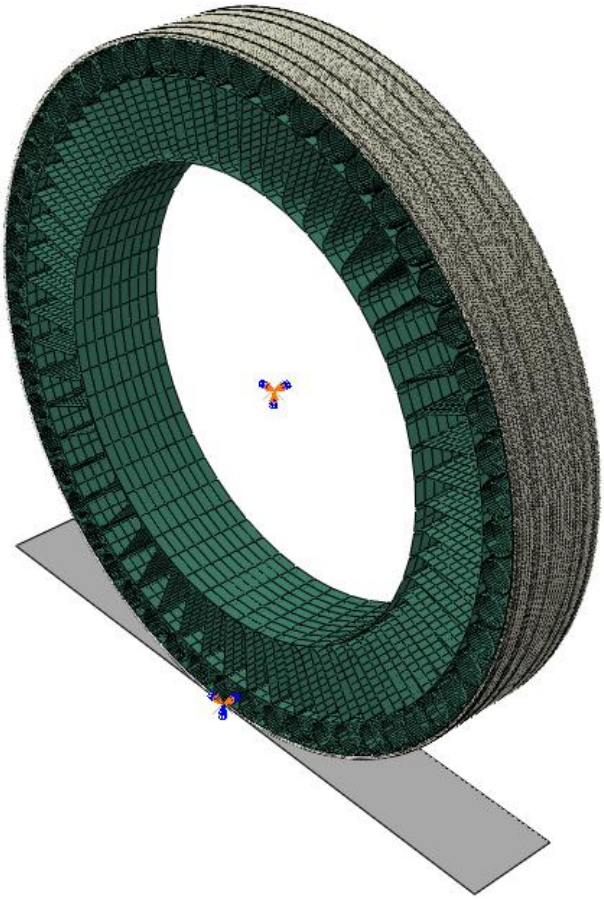

Figure 6-3: The complete 3D model with the load and boundary conditions

6.2 Preliminary Results of the Third Generation

When the wheel is loaded with 1250N, the deformed configuration has three cylinders in the contact region as shown in Figure 6-4. The contact pressure footprint of the wheel is shown in Figure 6-5 and the force displacement plot is shown in Figure 6-6.

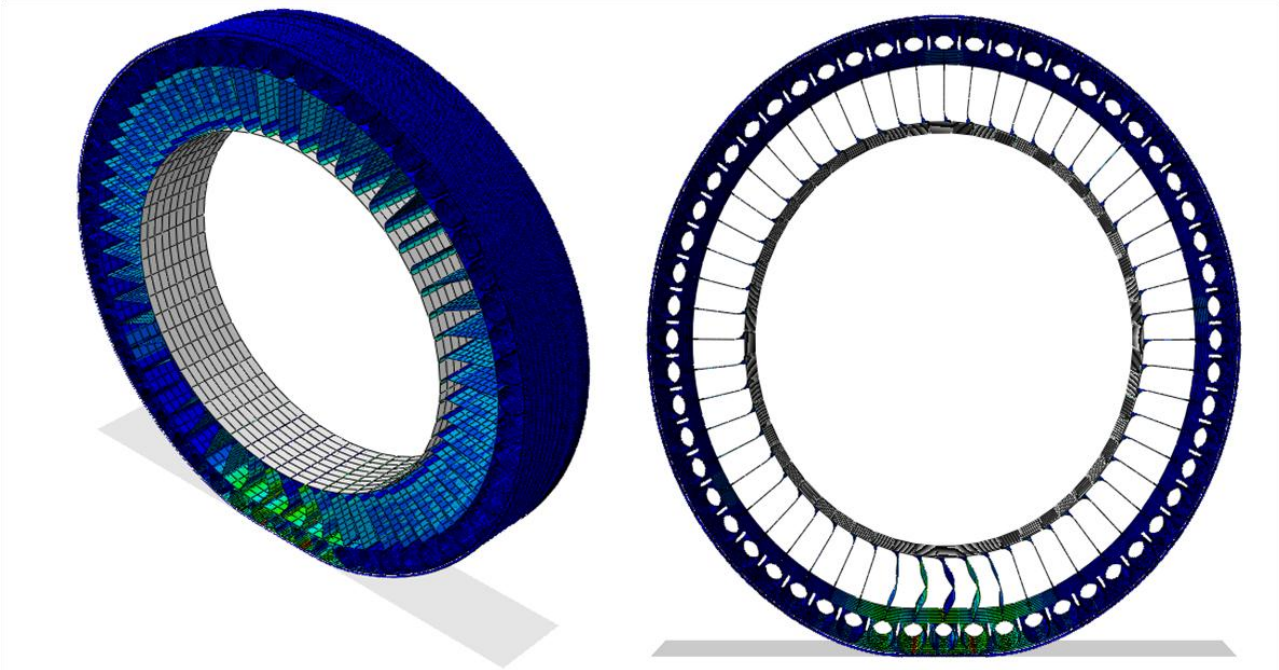

Figure 6-4: Deformed configuration of the Third generation Michelin Lunar Wheel

From the contact pressure profile it is seen that the pressure varies from 0.36 bar to 4.3 bar and three cylinders are present in the contact patch. It is also observed that the end cylinders have a higher pressure than the cylinders at the center.

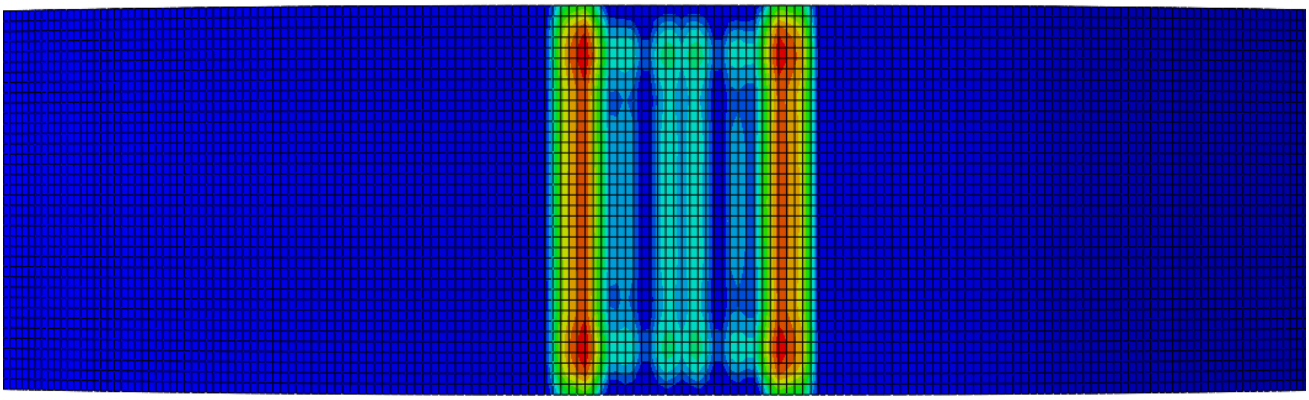

Figure 6-5: Contact pressure showing three cylinders in contact for the third generation Michelin Lunar Wheel

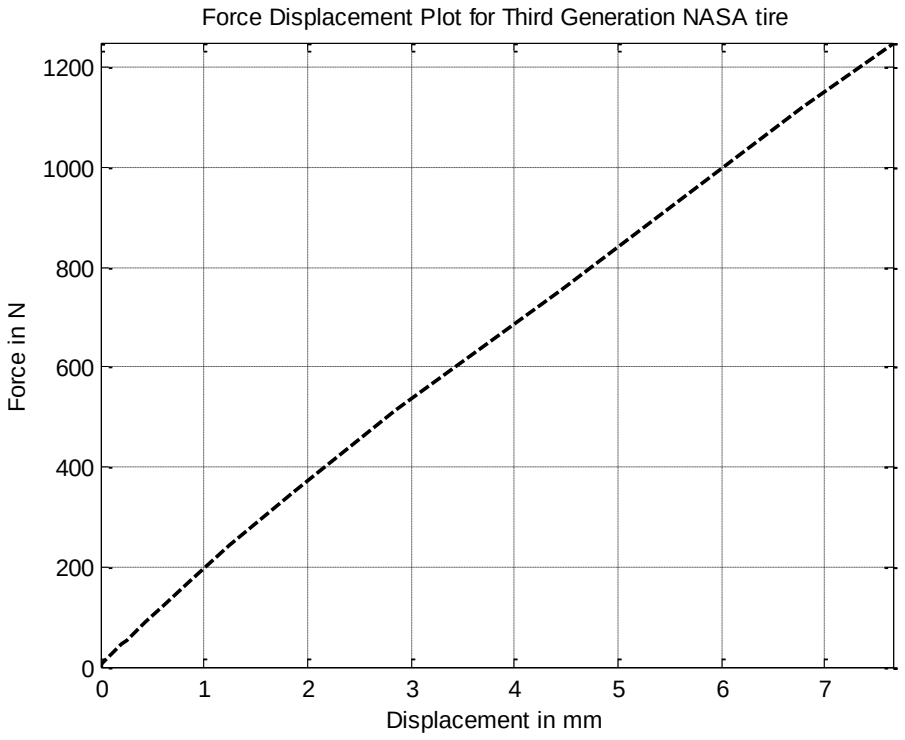

Figure 6-6: Force displacement plot for the Third generation Michelin Lunar Wheel

Comparing these results to those from the first generation analysis in Chapter IV and the experimental results in Chapter I, it is seen that neither the first or the third generation wheel give a uniform pressure distribution. Similar to the first generation results, the third generation wheel has three cylinders in the contact patch, unlike the experimental results which has five cylinders in the contact patch. Also the contact pressure values in both the generations are almost of the same magnitude with the lowest value being about 0.08 bar and the highest around 4 bar. The Table 6-2 summarizes the main differences and results for the first and third generation wheels. The conclusion is that regardless of the generation considered, the modeling issues concerning the pressure are the same for the two designs.

Table 6-2: Summary of the differences and results for the first and third generation wheel

Feature	First Generation Wheel	Third Generation Wheel
Wheel diameter	18.5''	27.56''
No of Cylinders in the shear band	33 circular cylinders with glass fiber rods	56 double layered oval shaped cylinders
Circumferential spacing between the cylinders	10.91 degrees	6.5 degrees
Connection	The cylinders with glass fiber rods glued between the inner and outer inextensible membrane with epoxy	The double layer cylinders are fixed between the two inextensible membranes by nuts and bolts
No of cylinders in the contact patch	3	3
Pressure variation	0.14 MPa to 0.4 MPa	0.036 MPa to 0.43 MPa
Contact Patch length	71.94 mm	72.95 mm
Displacement	16.74 mm	7.66 mm

CHAPTER SEVEN

CONCLUDING REMARKS

7.1 Conclusions

A computational model of a lunar wheel that can predict accurate contact pressure when the wheel is pressed against a rigid plane has been developed. From the literature, it is revealed that for prediction of accurate contact pressure the element should include not only the effect of transverse shear deformation but also the effect of transverse normal strain. To study this, a comprehensive investigation was done in ABAQUS on a simpler ring model to find the appropriate structural element type that could account for transverse normal strain and allow for convergence with respect to the mesh. It was found that ABAQUS has difficulty converging to a unique pressure profile when the mesh was refined, especially when the circular beam or shell becomes thin. The justification given by ABAQUS support team, after a five month period or submitting requests, is summarized as follows

- As the shear stiffness, GA, of the structural member tends to a high or infinite value, ABAQUS does not have the capability to capture a point load as the output. Hence even as the mesh is refined it is unable to show this feature.
- The elements used do not include the effect of transverse normal strain which causes the pressure to be discontinuous at the edge of contact.

This reply is of course correct for a beam with very high shear stiffness, but it was still interesting that ABAQUS did not perform better for finite values of shear stiffness or for 2-D elasticity. Essentially, the contact algorithm was not capable of handling high gradients in pressure, even though these gradients were not excessively high. However, as shown in Figure 3-11, only a slight change from a circular shape enables ABAQUS to converge even for a ring with high shear stiffness.

As a consequence of this limitation, a tread of considerable thickness and a reasonable stiffness was added onto the outer perimeter of the wheel, which resulted in unique and accurate contact pressure profiles even as the mesh was increased.

Further a sensitivity study of the contact pressure was performed for the various design parameters of the Michelin Lunar Wheel. The goal here was two-fold: 1) to find which parameter when varied gave a constant contact pressure distribution and 2) to see how the average pressure could be lowered. The important conclusions made are:

1. The model with the fixed epoxy case at the connections between the membranes and the circular cylinders produced results that matched experimental results better compared to the pinned epoxy case. It is also identified that a small alteration in degree of freedom in the connection between the cylinders and members changes the pressure distribution, and it is possible that a much more uniform pressure may exist for a connection that has stiffness between the fixed and pinned case.
2. From the cylinder orientation study, when the cylinders were rotated by five degrees, it was observed that the vertical stiffness of the wheel was not a

constant and changes the contact pressure distribution. This signifies that the wheel will experience vibration and possibly fatigue as it rolls.

3. A uniform pressure was determined by a slight adjustment of the profile of the ground. Instead of a flat surface, the shape necessary to produce uniform pressure was determined by taking the difference between the displacements caused by uniform pressure applied to the wheel to the required displacement boundary condition. The small perturbation in ground shape that is necessary to make this change shows the precision necessary for accurate modeling of the geometry and connections of the Michelin Lunar Wheel.

Overall, it is found that the contact pressure is highly sensitivity to precise modeling of the components in the Michelin Lunar Wheel and is affected by the material properties, the connection between cylinder and inextensible members, and the exact thickness/geometry of the inextensible membranes and cylinders.

7.2 Lack of Agreement between the Experimental and Simulation Results

The reasons for lack of agreement between the experimental and simulation results are:

1. Although the experimental results were reported to be for the wheel without a compliant layer, the TEKSCAN mapping sensor is about 0.2 mm in thickness so does provide a cushion. It is likely that this sensor is affecting the pressure by making it slightly smoother. However, this does not explain the large deviation between simulation and experimental results. Perhaps the

TEKSCAN sensor results are not able to resolve the high pressure gradients predicted by ABAQUS.

2. The simulation results predict micron sized gaps which in reality can be filled with particles, affected by surfaces that are not perfectly smooth, and/or thicknesses that are not perfectly uniform. All these imperfections would alter the idealized stress state predicted by the model as shown by the non-uniform ground study.

3. It is possible that friction at the connections has a large effect on the pressure distribution, which would be very difficult to model precisely. Stress redistribution around the connections may occur in a very complex way.

7.3 Future Work

In this section, some suggestions for further research work recommended are:

1. Study the contact problem in Chapter 2 using an ellipse instead of a circular ring to see if the primary problem is the shape, not the shear stiffness. This is motivated by the results presented in Figures 3-11 and 3-12.
2. Given that non-linear geometry can be used with ABAQUS, study the effect of loading path to see if convergence can be obtained for a circular ring without a compliant layer. The motivation here is that deformation changes the shape from a circle. Perhaps if high pressure gradients are avoided in the initial stages of deformation, convergence will be possible.

3. To develop a user defined contact element type or a higher order beam/shell element in ABAQUS that includes the effect of the transverse normal strain along with transverse shear deformation.
4. The contact algorithm should be studied for thin structural membranes and improved in order to address the high gradients in stress that occur near the edge of contact.
5. To develop a full three dimensional model can be created with all the lobes to see if the 2% error inherent in displacement in the 2D model can be reduced. For example, there are more modeling choices in 3D such as connections and element types.
6. Perform an optimization study based on the method of determining the ground shape that leads to uniform pressure. Instead of modifying ground shape, however, the non-uniformity can be introduced between the tread and the outer inextensible membrane. This can be done for all wheel orientations to try to find the best shape that minimizes the deviation of pressure from a constant value. One difficulty that arises is spoke offset which destroys symmetry. Hence this optimization study should be made with a symmetric spoke arrangement.

REFERENCES

[1] Rhyne et al., Non-Pneumatic Tire, United States Patent Number 7,201,194 B2.

[2] T. B. Rhyne and S. M. Cron, "Development of a Non-Pneumatic Tire," *Tire Science and Technology*, vol. 34, pp. 150-169, 2006.

[3] "The Vision for Space Exploration," National Aeronautics and Space Administration February, 2004.

[4] B. H. Wilcox, *et al*., "ATHELETE: A Cargo Handling and Manipulating Robot for the Moon," *Journal of Field Robotics*, vol. 24, pp. 421-434, 2007.

[5] B. H. Wilcox, *et al*., "ATHELETE: An Option for Mobile Lunar Landers," in *Aerospace Conference, 2008 IEEE*, pp. 1-8.

[6] D. Stowe, *et al*., "Designing of a Lunar Wheel," presented at 2008 ASME International Design Engineering Technical Conferences (ASME-DETC2008, ATTV-49981), Brooklyn, NY, 2008.

[7] V. Asnani, *et al*., "The development of wheels for the Lunar Wheel Development," *Journal of Terramechanics*, vol. 46, pp. 89-103, 2009.

[8] M. Chinnakonda, "Design and Analysis of CDM Swiss Tweel: Final Report, "January 31, 2008.

[9] S. K. Clark., "Mechanics of Pneumatics Tires," pp. 286-293, US Government Printing Office, Washington, DC, 1981.

[10] L. M. Keer and M. A. G. Silva., "Bending of a Cantilever Brought Gradually into Contact with a Cylindrical Supporting Surface," *International Journal of Mechanical Science*, vol. 12, pp.751-760, 1970.

[11] L. M. Keer., M. ASCE and G. R. Miller., "Smooth Indentation of a Finite Layer," *Journal of Engineering Mechanics*, vol. 109(3), pp.706-717, 1983.

[12] J. M. Block and L. M. Keer., "Partial Plane Contact of an Elastic Curved Beam Pressed by a Flat Surface," *Journal of Tribology*, vol. 129, Issue 1, pp. 60-64, 2007.

[13] F. Essenburg., "On the Significance of the Inclusion of the Effect of Transverse Normal Strain in Problems Involving Beams with Surface Constraints," *Journal of Applied Mechanics*, vol. 42, pp.127-132, 1975.

[14] P. M. Naghdi and M. B. Rubin., "On the Significance of Normal Cross-Sectional Extension in Beam Theory with Application to Contact Problems," *International Journal of Solids and Structures*, vol. 25, pp.249-265, 1989.

[15] C.F. Panek., "Study of contact problems with heat conduction or in connection with beam theories," Ph.D Thesis, Northwestern University, Evanston, IL, 1975.

[16] D. M. Robbins., "The contact of certain elastic shells with rigid flat surfaces," Report 05608-7-T (Office of Research Administration, The University of Michigan, Ann Arbor), 1965.

[17] DASSAULT SYSTEMES, Simulia, "ABAQUS: Analysis Users Manual", ABAQUS Documentation V6.8

[18] G. Strang and G. J. Fix., "An Analysis of the Finite Element Method", Prentice-Hall, Inc., 1973.

[19] G. Strang., "Introduction to Applied Mathematics," Wellesley-Cambridge Press, 1986.

[20] Marisa Orr., "Development of a finite element model to predict the behavior of a prototype wheel on lunar soil," Ph.D Thesis, Clemson University, Clemson, SC, 2010.